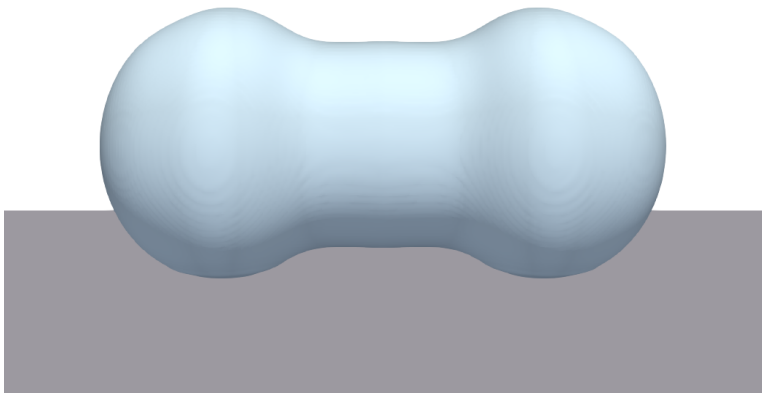

Numerical analysis of coalescence-induced jumping droplets on superhydrophobic surfaces

KONSTANTINOS KONSTANTINIDIS

Department of Mechanics and Maritime Sciences
CHALMERS UNIVERSITY OF TECHNOLOGY
Göteborg, Sweden 2022

THESIS FOR THE DEGREE OF LICENTIATE OF ENGINEERING IN THERMO AND FLUID DYNAMICS

Numerical analysis of coalescence-induced jumping droplets on superhydrophobic surfaces

KONSTANTINOS KONSTANTINIDIS

Department of Mechanics and Maritime Sciences

Division of Fluid Dynamics

CHALMERS UNIVERSITY OF TECHNOLOGY

Göteborg, Sweden 2022

Numerical analysis of coalescence-induced jumping droplets on superhydrophobic surfaces
KONSTANTINOS KONSTANTINIDIS

Thesis for the degree of Licentiate of Engineering with report no 2022:13
ISSN 1652-8565
Department of Mechanics and Maritime Sciences
Division of Fluid Dynamics
Chalmers University of Technology
SE-412 96 Göteborg
Sweden
Telephone: +46 (0)31-772 1000

Cover:
Front page image caption: Two equal droplets coalescing on a superhydrophobic surface.

Chalmers digitaltryck
Göteborg, Sweden 2022

Numerical analysis of coalescence-induced jumping droplets on superhydrophobic surfaces

KONSTANTINOS KONSTANTINIDIS
Department of Mechanics and Maritime Sciences
Division of Fluid Dynamics
Chalmers University of Technology

Abstract

Bio-inspired superhydrophobic surfaces are used in numerous technological applications due to their self-cleaning ability. One of the several mechanisms reported in literature and responsible for self-cleaning is the phenomenon of coalescence-induced jumping of droplets from such surfaces. The phenomenon is observed for scales below the capillary length and when gravity is negligible. Primary applications of this technology are on heat-exchangers or any other that involve surfaces for which anti-icing and water-repellency properties are desired. This thesis comprises two publications that involve high-fidelity numerical investigations on fundamental features of the jumping droplets phenomenon and focuses on two important aspects. The first one is a study on coalescing and jumping of microdroplets ($R < 10$ µm). The differences in the jumping process (for example, reduction of the merged droplet jumping velocity) are pointed out as a function of the initial size of the droplets. Through an analysis of the energy budget, several degrees of dissipation are found, which is attributed to a competition between viscosity and the strong capillarity on the interface. The second publication focuses on the interaction of the merged droplet with a superhydrophobic surface with hysteresis. It is found that such a case has a reduced jumping velocity as compared to a no-hysteresis one. Using a dynamic contact angle model is beneficial to capture the receding contact angle and provide a more accurate estimation of the overall process. In this work, a combined Immersed Boundary – Volume-of-fluid method with different contact angle models and a Navier-slip boundary condition is used. The numerical framework has been extensively validated.

Keywords: jumping droplets, coalescence, superhydrophobic, surfaces, contact angle, wetting, hysteresis, self-cleaning, CFD, VOF, immersed boundary

Acknowledgements

For the co-operation and support in the first part of this project, I feel the obligation and at the same time pleasure to initially thank Srdjan (Professor Srđan Šašić), who as my main supervisor, has offered me among many others his guidance, his knowledge and his honesty. I would also like to thank my co-supervisor Andreas (Andreas Mark, from Fraunhofer-Chalmers Centre) who has contributed in many ways in this project, being the main responsible of the code IBOFlow – that is used throughout this project – and providing his experience in numerics and publishing papers. In addition, Johan (Johan Göhl, from Fraunhofer-Chalmers Centre) as our collaborator has provided important insights in the project and support with the details and improvement of the code.

Colleagues and friends have also kept encouraging and motivating me during these first two and a half years of my PhD studies, at the multiphase flow group and at the Fluid dynamics division, therefore I would like to sincerely express my gratitude to them. Lastly, I have to express my loving feelings towards my brother and my parents, who provide me with their unconditional care and support these last 31 years (30 in case of my brother being one year younger).

Abbreviations

CFL	–	CourantFriedrichsLewy or Courant number
CICSAM	–	Compressive Interface Capturing Scheme for Arbitrary Meshes
CSF	–	Continuum Surface Force
MCL	–	Moving Contact Line
SIMPLEC	–	Semi-Implicit Method for Pressure Linked Equations-Consistent
VOF	–	Volume of Fluid

Nomenclature

$\hat{\mathbf{n}}$	unit interface normal vector	(-)
$\mathbf{f}_{SF}$	surface tension body force	($\mathrm{kg{\cdot}m^{-2}{\cdot}s^{-2}}$)
$\mathbf{n}$	interface normal vector	($\mathrm{m^{-1}}$)
$\mathbf{n}_w$	normal wall direction	(m)
$\mathbf{v}$	velocity	($\mathrm{m{\cdot}s^{-1}}$)
$\mathbf{v}_{wall}$	slip velocity at wall	($\mathrm{m{\cdot}s^{-1}}$)
K_i	normalised kinetic energy in direction i	(-)
K_{total}	normalised total kinetic energy normalised	(-)
S_{lg}	normalised surface energy in the liquid–gas interface	(-)
$\overline{v}^*$	averaged normalized vertical velocity of droplet	(-)
$\overline{v}^*_{jump}$	normalized jumping velocity of droplet	(-)
A_{cont}	Contact area to solid surface	($\mathrm{m^2}$)
c_R	Number of cells per radius	(-)
f_{Hoff}	Hoffman function for Kistler dynamic contact angle model	(-)
$F_{pinning}$	Pinning or adhesion force	(N)
g	gravitational acceleration	($\mathrm{m{\cdot}s^{-2}}$)
p	pressure	($\mathrm{kg{\cdot}m^{-1}{\cdot}s^{-2}}$)
R or R_i	radius of initial droplets	(m)
R_c or R_{end}	radius of merged droplet	(m)
t	time	(s)
U_{CI}	normalized capillary-inertial velocity	(-)
Greek Letters		
α	volume fraction	(-)
$\Delta\tau$	normalized time step	(-)
$\Delta\theta$	contact angle hysteresis	($^\circ$)
ΔS	normalised available surface energy for coalescence of droplets	(-)
Δt	time step	(s)
Δx	cell size	(m)

κ	interface curvature	(m^{-1})
λ	slip length	(m)
τ	normalized time	(-)
τ_{CI}	normalized capillary-inertial time	(-)
μ	dynamic viscosity	$(\mathrm{kg{\cdot}m^{-1}{\cdot}s^{-1}})$
ρ	density	$(\mathrm{kg{\cdot}m^{-3}})$
σ	surface tension	$(\mathrm{kg{\cdot}s^{-2}})$
θ_{adv}	advancing contact angle	$(^\circ)$
θ_{dyn}	dynamic contact angle	$(^\circ)$
θ_{rec}	receding contact angle	$(^\circ)$
Dimensionless numbers		
Ca	capillary number	(-)
Oh	Ohnesorge number	(-)
Re	Reynolds number	(-)
We	Weber number	(-)

List of publications

This thesis consists of an extended summary and the following appended papers:

Paper A K. Konstantinidis, J. Göhl, A. Mark, and S. Sasic. Coalescence-induced jumping of microdroplets on superhydrophobic surfaces — A numerical study. *Canadian Journal of Chemical Engineering* **100**.12 (Dec. 2022), 3517–3530. DOI: 10.1002/cjce.24591

Paper B K. Konstantinidis, J. Göhl, A. Mark, and S. Sasic. Coalescence-induced jumping of droplets from superhydrophobic surfaces — The effect of contact-angle hysteresis. *Physics of Fluids* **34**.11 (Nov. 2022), 113302. DOI: 10.1063/5.0118645

Contents

Part I

Extended Summary

1 Background – self cleaning in nature and technological applications

Self-cleaning is the act of removing contaminants from a surface by water when no external energy is mechanically directed to the purpose of cleaning. These contaminants can be dirt particles of various shapes or colloids. The self-cleaning functionality has been observed in various examples in nature and, because of its benefit, it has been a subject of extensive research for potential use in technological applications. The most known cases of surfaces which possess this ability are characterised by their liquid-repellency and it is their particular surface patterns and textures that cause such a behaviour. For contact angles above 150° these surfaces are termed superhydrophobic. In numerous examples, spherical droplets are found on top of such surfaces. Droplet deposition, condensation or break-up from larger non-spherical liquid formations are only a few of the cases representing interaction of droplets with superhydrophobic surfaces. Furthermore, the surfaces are characterised by low adhesion of liquids and the drops tend either to move rapidly on them or to rebound, when there are external energies present or when there is prior inertia of the droplets.

1.1 Self-cleaning in nature

It has been established that numerous biological surfaces are facilitating their clean state through the phenomenon of self-cleaning[1]. The lotus plant has been the most popular among these cases, with its leaf remaining clean by removing dirt particles with droplets rolling off them, a repeated behaviour termed the lotus effect[2]. It takes advantage of the natural micro-sized structures on the surface that give it a superhydrophobic behaviour. An example of the micro-structures that enhance superhydrophobicity of the lotus leaf and facilitate dirt removal is given in Figure 1.1. Furthermore, insects with large wings, like the cicada, need the wetting properties of a superhydrophobic surface to remove contaminants such as particles or microorganisms[3]. They facilitate a self-propelling behaviour of droplets from their surface (that overcomes gravity), a phenomenon that had not been observed till only recently. In this way their wings retain their wing-functionality. The self-cleaning process has been observed not only in rainy environments, but in humid ones as well, where the droplets are formulated on top of the wings due to condensation. Similar examples of self-cleaning have been observed for mosquito eyes or for legs of the water-striders. After having observed the self-cleaning capabilities of the mentioned examples in nature, the obvious task of research is to identify the mechanisms that facilitate such a functionality. One of those mechanisms is the subject of this thesis, but it is straightforward to first mention a couple of examples of self-cleaning in technological applications.

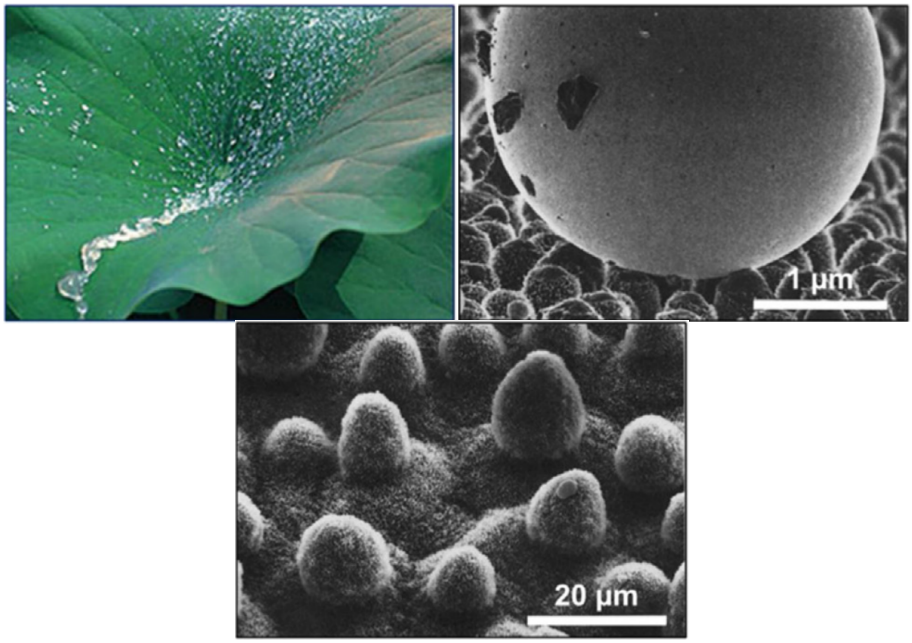

Figure 1.1: *The lotus leaf (top-left) and the structure of its superhydrophobic surface(bottom). The droplet(top-right) captures dirt particles before removing them, Ref.[2].*

1.2 Self-cleaning in technological applications

Inspired by the relation between surface hydrophobicity and the phenomenon of self-cleaning observed in nature, various designs of such surfaces have been proposed and used in numerous technological applications. The technology has been further improved in creating surfaces that possess limited or zero contact angle hysteresis. This suggests that such surfaces do not exhibit pinning or have a zero sliding angle, so that droplets or dirt particles can be immediately removed from an inclined surface. Another interesting phenomenon is that degradation of these properties with time has been reported.

There is a considerable list of applications where superhydrophobic surfaces have been tested and considered beneficial for facilitating self-cleaning. There is, for example, sound experimental evidence of surfaces that promote anti-icing behaviour due to the roughness of the superhydrophobic surfaces[4]. Moreover, building or textile materials[5] and solar panels[6, 7] have been suggested to preserve a clean state through the self-cleaning abilities attributed to superhydrophobicity.

Heat exchangers were one of the first applications involving superhydrophobic surfaces and related to self-cleaning. An often-met feature of such units is drop-wise condensation in condensers, a mechanism that enhances heat transfer[8]. In addition, heat exchangers

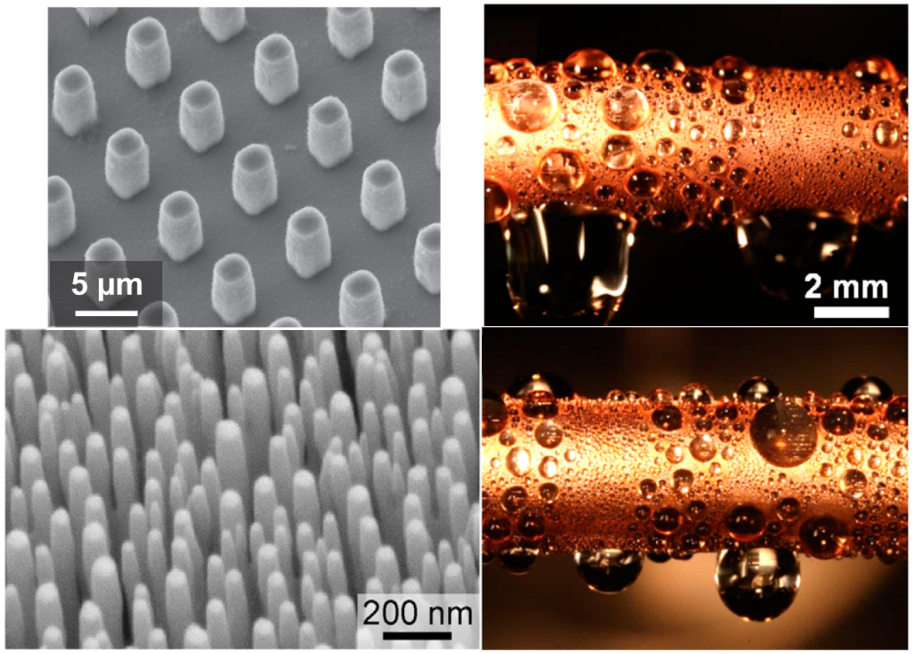

Figure 1.2: *Two examples of manufactured microstructures with pillars that are used for improved drop-wise condensation by Ref.[12](top-right) and Ref.[13](bottom-right). Two instants of drop-wise condensation are shown on a superhydrophobic surface of copper coated with graphene at Ref.[14].*

benefit from the presence of low adhesion on superhydrophobic surfaces, thus enabling anti-fouling opportunities typically on their thin elongated tubes. A variety of studies have been performed regarding the details of textured and heterogeneous surfaces that promote drop-wise condensation, when they are exposed in saturated environments[9]. An example of such superhydrophobic surfaces is presented in Figure 1.2. The phenomenon of coalescence-induced jumping droplets has been noticed for the first time through a similar experiment involving condensation by Boreyko and Chen[10]. In that work the authors looked at two or more droplets residing on a superhydrophobic surface, where they approach, merge (the phenomenon also known as coalescing of droplets), and finally are self-ejected from the surface. This is a mechanism that this thesis will mainly focus upon, with more details to be discussed in Section 1.4. Finally, the anti-fouling abilities of superhydrophobic surfaces have been tested in a limited number of studies, that performed either experiments of removal of dirt particles and colloids or numerical simulations that dealt with removal of contaminated droplets.[3, 11]

1.3 Mechanisms for self-cleaning

Self-cleaning was initially analysed observing lotus-leafs, which inspired technological applications to first understand the importance of superhydrophobic surfaces and then to develop methods that highly improve the hydrophobicity of surfaces. As for the lotus-leaf effect, self-cleaning is initiated by the presence of an external field (gravity) combined with the low-adhesion energy between water and the leaf surface. As a result, the droplet starts to move and rolls on top of the superhydrophobic surface, accumulating other droplets and dirt particles by inertia until the moment the droplet-particles cluster rolls off the side of the lotus leaf.

On the other hand, for the cases that droplets condensate on the cicada wings or on the surfaces of heat exchangers, self-cleaning is facilitated by the removal of the droplets with a different and fascinating removal mechanism. The mechanism is termed the coalescence-induced jumping of droplets. Here, the process is initiated by the coalescence of droplets, while their rapid expelling from the superhydrophobic surface is caused by the release of the surface energy, in combination with some of the fundamental features behind the interaction of droplets with the substrate (to be discussed in what follows). As argued in Wisdom et al.[3], jumping droplets removed particles through the following mechanisms i) floating, where a hydrophilic particle is first entrained by a single droplet before such a conglomerate merges with other droplets (or conglomerates) and then jumps, ii) lifting, in which the particle is captured at the interface of one of the drops or during the oscillations of the coalescence of more droplets before the merged conglomerate jumps, and, lastly, iii) by accumulation of smaller particles into a pack, created by the wetting of particles from condensation and then the creation of liquid bridges with different particle clusters followed by the initiation of jumping. In the next section we will look in more detail into different stages of the coalescence-induced jumping of droplets.

1.4 Coalescence-induced jumping of droplets – identification of different stages

Among the mechanisms that facilitate removal of particles from surfaces, we identify coalescence-induced jumping droplets as a most promising one for various technological applications. Our argument resides in a zero requirement for external energy to be provided to the system in order to facilitate self-cleaning. For example, horizontal substrates would not be able to facilitate gravity for self-cleaning, in contrast to the jumping droplets. The process starts with the coalescence of two or more droplets, while they are on top of a superhydrophobic surface. It has been reported initially by Boreyko and Chen[10] when the authors reported an out-of-plane movement upon coalescence of droplets, which were nucleated from condensation on a cold superhydrophobic surface. Various numerical and experimental investigations followed and uncovered a physical explanation of the process

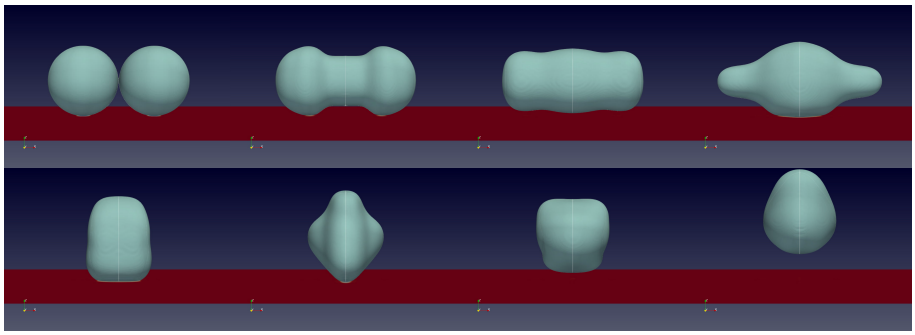

Figure 1.3: *A sequence of stages of two droplets leading to a jumping of the merged droplet. The stages include the liquid bridge expansion, various forms of oscillation of the merged droplet and an eventual jumping. The entire sequence is numerically reproduced by a combined VOF-immersed boundary framework used in this work.*

and identified its different the stages.[15–19]. Coalescence is initiated with a formation of a liquid bridge between the merging droplets. The numerical investigation of Liu et al.[18] and the corresponding experiment with leidenfrost droplets by the same group[19] pointed to the specific stages through which the jumping process of droplets undergoes, as seen in Figure 1.3. The liquid bridge is initiated by the extremely high curvature that appears at the interface near the point of coalescence. As the bridge expands, liquid mass moves to the direction of the liquid bridge expansion, with the flow being mostly governed by the forces of capillarity near the interface and inertia. The liquid bridge impinges on the superhydrophobic surface and causes expansion of the initiated contact area on the surface. The interaction of the liquid and solid in the vicinity of the triple contact line is governed by the wettability of the surface, with the true values of the contact angles and the dynamics of the moving contact line becoming significant factors.The role of wettability be discussed in the next section.

The next stage of the jumping process, as the droplet-surface contact area expands on the solid surface, corresponds to the effect of high contact angles with the inertia of the droplet still interacting with the surface. This breaks the symmetry of the droplets coalescence and causes redirection of the liquid mass outwards from the surface. After the expansion reaches a maximum wetting area, the contact area decreases, with the merged droplet retracting from the surface with a receding moving contact line. During the last two stages of the entire process, the merged droplet oscillates between oblate and prolate shapes in the xz- and yz-planes. There exists another significant observation near the end of this retraction, before the merged droplet gets detached. Here, as the merged droplet moves upwards, a deceleration (i.e. a decrease of the velocity) in the vertical direction is noticed. It is argued that this phenomenon can be due to the effect of the contact angle or a dissipation of the translational energy at the period that the air substitutes the liquid volume between the merged droplet and the solid surface. During the shape oscillation the contact area is minimised rapidly up to the moment of detachment of the merged droplet from the surface. As the process is dominated by the capillary and inertial forces,

it is due to the latter that a detachment occurs. Following the detachment, in the final stage of the process, the merged droplet rises through the gas-phase, continuing its shape oscillations damped by the viscosity. In the same time, there is a drag force acting on the droplet, which leads to the stabilisation of the latter's shape into a spherical one.

1.5 Theory of wetting and a connection to this work

Due to the existence of roughness on superhydrophobic surfaces, two situations have been theoretically established and examined in numerous studies. The first one is a partial wetting type[8], also referred to as the partial Wenzel wetting, where the liquid contact area is fully wetting certain regions of the solid surface, while in the remaining locations air voids are trapped between the liquid and the solid zones. The second situation is a consistent existence of voids between all defects and surface textures, while the majority of the liquid is situated on the tip or highest point of roughness textures. The defects or similar features with a larger height related to the rest of the surface are typically termed pillars. In any realistic superhydrophobic surface, the pillars become a resting area on top of nano- or micro-structures of the surface, while the intermediate regions of the solid and liquid zones are gas voids. For this situation, theoretical calculation of an apparent contact angle has been introduced using the Cassie-Baxter theory[20], which gives the equilibrium contact angle on the pillars. For the Cassie state, the relation that returns the single apparent contact angle reads:

$$\cos\theta_{app,CB} = f\,(1 + \cos\theta_{eq}) - 1\,, \tag{1.1}$$

with $\theta_{app,CB}$ being the global apparent contact angle as would be found for a low hysteresis case and f the Cassie-Baxter parameter which is given as the projected area of pillars divided by the projected contact area in a homogeneous plane.

The partial Wenzel wetting bases its theory on the normal Wenzel state that is observed in wetting occasions where the whole area of a rough solid surface is in contact to the liquid[21]. The apparent contact angle for the Wenzel state is calculated as:

$$\cos\theta_{app,W} = r_W\ \cos\theta_{eq}\,, \tag{1.2}$$

with $\theta_{app,W}$ being the global apparent contact angle as observed for a low hysteresis case, θ_{eq} the equilibrium or Young's contact angle and r_W the Wenzel roughness parameter which is given as the total surface divided by the projected contact area in a homogeneous plane.

The Cassie-Baxter form of interaction of a droplet with a superhydrophobic surface is usually treated with a high slip velocity on the solid surface or with the formation of a gas layer between the liquid and solid zones. Note that here an existence of the contact-angle hysteresis is fully neglected, which has been observed to be the cause for pinning and

other dissipative behaviours of the contact line. Such a statement requires from us in the current study to establish the ability of our modelling the variations of contact angle on the grid-cell level. These variations could be also caused by the dynamic behaviour of the contact angle, subjected to the contact line velocity or the presence of the imbalance of the stresses (Young's equation) in the contact line, when the contact angle differs from the theoretical equilibrium angle of the system. However, the equilibrium contact angle is defined as a feature of the surfaces when they are fully flat and homogeneous, otherwise such a contact angle occurs in purely nanometre scales. At such length scales we consider that the continuum approach breaks down and intermolecular dynamics are important to account for.

2 Objectives and Contributions of the thesis

The primary objective of this work is to formulate, validate and use a trustworthy framework to investigate numerically and in great resolution the process of coalescence-induced jumping of droplets from superhydrophobic surfaces. This a considered a necessary step before introducing the removal of particles into the overall numerical framework that looks at fundamentals of the self-cleaning process.

2.1 Why are numerical investigations of self-cleaning necessary?

It is essential to understand the mechanisms that support the process of self-cleaning on different surfaces if we are to explore its potential use in various industrial applications. Such surfaces are sometimes located in environments where their quality can be negatively affected by, for example, fouling, icing or frosting. Such locations and components may be difficult to reach and substitute, making it very cumbersome or even impossible to test their performance experimentally.

In addition, we need to identify which geometrical parameter or substrate characterization of a superhydrophobic surface could promote the self-cleaning process. In the same manner, there is a need to recognise limitations in the design of specific surfaces and to suggest possible improvements. It may become impractical to study experimentally a wide range of geometrical parameters or features of the surfaces to identify the ones that could lead to improvements in the self-cleaning. A sound point here is that, in contrast to numerical simulations, experiments are often limited with regards to how many different superhydrophobic surfaces can be tested. Moreover, controlling and recording the jumping process with the different levels of resolution reduces the possibilities of a research outcome that identifies fundamental processes between the droplets and particles during their interaction, or, similarly, the interaction of the both of them with the superhydrophobic surface, either in a molecular or a modelled form.

On the other hand, numerical investigations can be used to identify details that experiments are restricted on informing. Therefore, for our research to uncover the fundamentals behind how coalescing droplets can remove solid particles from surfaces, a series of steps are required. These numerical investigations, as are presented in the current thesis for the jumping droplets only, assure that the physics of such systems are fully understood and recovered. Therefore, a thoroughly validated numerical framework is established in this thesis that will be used in the second part of this project to perform simulations of self-cleaning involving a number of particles and with multiple droplets. Additionally,

the framework makes it possible for us to account for the interaction of droplets and particles (either modelled or resolved) with the microstructures of a superhydrophobic surface.

2.2 Jumping of equally-sized jumping droplets and the existence of a cut-off radius

We start from the argument that it is highly improbable to attain any reliable information on the process of self-cleaning involving particles and droplets that coalesce and jump, without paying meticulous attention to fine details of the involved phenomena. In the same manner, it is fair to say that it is problematic to even consider introducing particles into the framework before the latter is thoroughly validated and trustworthy for jumping droplets only. More specifically, a part of the physics that is vital in this case is the interface transport and sharpness, for which we need a robust model that can maintain a sharp interface and an accurate computation of the curvature between every time-step. In addition, the high pressure jump at the interface for relatively small droplets requires minimisation of the spurious velocities, that occur in the velocity field after applying the conservation laws of mass and momentum. The smaller the size of the droplet, the greater are the surface tension forces at the interface of the droplet, increasing the mentioned numerical errors. These problems should be removed altogether or at least drastically minimised in a framework capable of handling simulations of jumping droplets with sizes of as low as 0.5 µm in radius. We note here that we work with droplets of 0.5-700 µm in radius, a size for which gravity can be neglected and the length scale of the problem remains smaller than the capillary length.

From the initial experimental observations of the jumping-droplets phenomenon, difficulties have been outlined in capturing (both experimentally and numerically) the governing time-scale of jumping at small scales. The time scale is given by the competing interaction between the surface tension and the inertial forces. The process of coalescence and the liquid bridge dynamics, at length scales that are below the capillary length, are governed by a capillary-inertial time scale t_{CI}. Using the initial radius of the droplets as the length scale of the flow, a capillary-inertial velocity is defined. The jumping velocity of the droplets is often given for the different length scales normalised by the capillary-inertial velocity. In fact the normalized jumping velocity happens to have the same value with the square root of the Weber number, when velocity is set as the average jumping velocity in the Weber number formula. This is pointed out because the Weber number gives a relation between the inertial and the capillary forces in a system. The time scales are decreasing with a power of 3/2 with the droplet radius decrease. As a result, for droplet sizes approaching a few microns the process accelerates so much that it cannot be captured by the frame capabilities of cameras in current experimental environments. It was Boreyko[10] who first suggested that the jumping velocities of the merged droplet, in relation to variations in the initial radius of the droplets, follow a capillary-inertial

scaling and adhere to the velocity scales of the phenomenon. The capillary-inertial velocity is related with a power of $-1/2$ to the initial radius of the droplets. However, while this scaling law suggests that the normalised velocity will be constant when reducing the droplets size, a deviation was observed from this theory for droplets below 25 µm in radius. The term microdroplets is sometimes used in the relevant literature for such droplets. We thus identify henceforth in this thesis that the droplets of sizes $R \leq 10$ µm will be referred to as microdroplets. A limited number of studies focused on the causes of the existence of the observed cut-off radius, with the dominating opinion suggesting the interaction with sides of micro-structures as the main cause of energy dissipation and a consequent reduction of the jumping velocity in comparison to the one theoretically expected by the capillary-inertial scaling.

From a theoretical analysis, we see that for the decreasing droplet sizes the Ohnesorge number increases (the number that relates the viscous forces to inertial and surface tension ones), as the latter is inversely proportional to the droplet size. However the fact that, for the investigated water droplets in this work, the Reynolds number Re will be above 1, shows that inertia is still able to compete with and possibly overcome the viscous forces. Moreover, the capillary number Ca (that relates the viscous forces to the surface tension ones) is well below 1 for droplet sizes of as low as $R = 0.2$ µm, hence the capillary forces are markedly exceeding the viscous dissipation. The two non-dimensional numbers are proportional to the droplets velocity. Considering the velocity scaling behaviour, the non-dimensional jumping velocity in the microdroplets range is required to be at least a half of the mean jumping velocity that has been observed in the previous experimental and numerical studies. These studies report a non-dimensional jumping velocity $v^*_{jump} \sim 0.2 - 0.24$ for droplets with $R > 25$ µm. Otherwise, for a half of that velocity or lower, the drop in the Reynolds number will suggest that viscosity has increased its influence in the process.

Following the initial studies exploring the jumping droplets, other experimental studies that investigated surfaces with improved wetting properties suggested that droplets as small as $R = 0.5$ µm seem to have been successfully ejected from the surface[22, 23]. With this we identify the theoretical capability of the jumping process to adhere to the capillary-inertial scaling of the velocity in microdroplets. We therefore identify the need to investigate the stages of the jumping in a numerical investigation, as well as the energy variations in the domain for the kinetic, surface and viscous dissipation energies.

There are numerical studies which observed the continuation of validity of the mentioned scaling law to droplets radii as small as 0.5 µm for surfaces that are modelled as flat[24]. On the other hand, Attarzadeh and Dolatabadi[25] is an example of a study that performed simulations with pillars and observed different modes of interaction with the structures for different initialising positions of two equally-sized droplets. However, the exact interaction at the micro-scale is still not fully understood and, more importantly, it cannot be generalised for different sizes of micro-structures or droplets. We remind that the goal of this project is to eventually introduce particles (e.g. dirt) in our numerical framework, and that is why we support that giving a more fundamental explanation behind this interaction will help us to estimate the maximum size of particles that can

be expected to be removed by jumping droplets.

2.3 Jumping of microdroplets as a first focus in this thesis

With this work it is identified the smallest scale for the phenomena of the capillary-inertial regime to be still relevant for the jumping process. This is achieved by the level of resolution which is used in this numerical investigation. The simulations of jumping droplets on flat surfaces, even though they inherit a degree of simplification of the problem and include an assumption that modifies the main idea of the influence of roughness present on superhydrophobic surfaces, can still provide valuable information for the phenomena. More specifically, it helps uncover the details of the behaviour of droplets spanning all radius ranges of the capillary-inertial scaling. Using a basic formulation for the boundary condition of the wall velocity and contact angles, our investigation gives the smallest droplets size for which the numerical framework is still able to capture all the stages of the jumping process and help with estimating the available energy that would facilitate self-cleaning. The details of this study are given in Paper 1 of this thesis.

As a general comment here, it can be stated that the interaction of the contact line with the surface and the special features of the superhydrophobic surface cause the prediction of the moving contact line dynamics and of the true values of the contact angle to be a great challenge. In order to not lose information, the interaction needs to be modelled with respect to the geometrical features of a superhydrophobic surface and the physical phenomena, captured theoretically and experimentally, that govern the movement and stresses of a contact line. Only the behaviour of the contact line for the cells adjacent to the wall will require a specific treatment, which is implicitly imposed in our framework that accounts for the continuum physics of the fluids. More on this subject will be given in the Methodology section.

2.4 Jumping droplets from superhydrophobic surfaces with hysteresis as a second focus of the thesis

Superhydrophobic surfaces attribute their behaviour to the structures that control their interaction with the fluids. These structures can be both manufactured in a textured and precise manner or they could be coated in manners that would create random directions of the normal surface to the wall, multiple and asymmetrical points of contacts and different heights between the structures. In the case of biological surfaces, superhydrophobic surfaces are mostly observed with such random patterns. The manufactured hierarchical surfaces, on the other hand, are obtained by precise deposition of micro-structures, which then undergo treatments that add an additional layer of random nanostructures on the

solid surface. It is these nanostructures that are responsible for a certain degree of hydrophobicity, with the larger micro-structures (from 0.5 μm and greater) that cause the very high (superhydrophobic) contact angles. As a result, the surface demonstrates superhydrophobicity only when the droplets reach a size comparable to the size of the microstructures or larger[22, 23, 26].

The interaction of droplets with such structures has been mostly simulated using rectangular pillars in 3D or in 2D simulations using randomised surfaces. The required level of resolution would necessitate using computational cells much smaller than a micrometer, something that would cause excessive computational cost, which, in turn, would make unfeasible any systematic study involving variation of the governing parameters. Hence, a connection of a superhydrophobic surface to the continuum domain is preferably achieved by defining and obtaining the two angles responsible for hysteresis, the advancing contact angle and the receding contact angle. These angle become available for any actual surface by performing an experiment with a static droplet and measuring the contact angles through enlarging and decreasing of the droplet volume. Moreover, it is straightforward to find situations where hysteresis exists on the surface. The reasons for the existence of the pinning effect, that is experimentally observed and which is caused by hysteresis, could be a non-optimal superhydrophobic coating or pattern, problematic manufacturing of the surface or even degradation of the surface that causes a superhydrophobic surface to gradually lose its ability of a contact angle near 170° and the contact angle hysteresis of nearly 0°. Various dynamic contact angle models have been suggested and implemented in numerous applications, and giving a full account about them is outside of the scope of this thesis. We do find them important in order to control the sensitivity of the jumping droplets process to the actual contact angles that the merged droplet experiences. The values of such angles can be close to the advancing or receding contact angles observed for a certain surface in a static experiment. However, due to the presence of high velocities and acceleration in flow systems where inertia is strong, it is straightforward to recognise that these values can be exceeded. For such a case, the numerical results do not highlight the possible sensitivity of the jumping efficiency, a study which we have decided to undertake in the scope of this project. A detailed analysis can be found in Paper B of the thesis.

After adding the effect of superhydrophobic structures to the boundaries with a scheme for imposing contact angles, we used a slip velocity for the interaction with the idealised flat solid surface. The contact angle in various numerical cases in our work was implemented through either a static formulation or a dynamic contact angle model, that can be dependent on the flow parameters. Since we have in mind the interaction to general solid structures (e.g. particles) as the next step, we have recognised a need to have a reliable and flexible model that could handle both particles and superhydrophobic surface. Flows around moving bodies can be modelled using a dynamic moving mesh around the body or an immersed boundary method. The latter can be implemented in a structured mesh with the existence of a solid body implicitly calculated. Therefore, the immersed boundary method was chosen in order to account for correct calculations of forces on the solid bodies or boundaries. The method uses a triangular surface mesh for the immersed body,

but it does not require any refinement of the fluid cells as a function of the geometrical characteristics of the body. The forces are evaluated from the average normal vector of the unstructured faces on the body surface by using fictitious ("ghost") cells in the solid phase. For our framework the grid is given by a hexahedral type octree mesh with Adaptive Mesh Refinement (AMR), which allows for higher accuracy in the calculation and transport of the surface tension forces in the vicinity of the interface. Therefore, we use in this work a combined VOF-Immersed boundary that has a benefit of limiting the computational time and following a single-mesh approach both for interfaces and for the existence of movable or static solid surfaces.

2.4.1 Motivation for the organisation of research in this work

We emphasise here that the order of steps that should be taken to formulate a validated and trustworthy numerical framework is of great importance to reach the goals of this project. Wettability effects, capillarity and strong inertial forces are the driving forces behind the studied type of the self-cleaning process. All our actions are designed in such a way as to focus on the details of one of the mentioned physical phenomena, and afterwards to create the entire framework in a building block approach. The capillary-inertial effects are discussed in Paper A, whereas the behaviour of the interface-solid interaction is addressed in Paper B with the detailed approach of modeling for superhydrophobic surfaces with defects or other pinning phenomena that cause hysteresis and/or dynamic behaviour of the contact line. With the conclusions of the analysis of the two papers presented in the thesis, we set up the possibility of carrying out simulations with jumping droplets trapping and removing contaminants from a superhydrophobic surface.

3 Methodology

3.1 Methods used in the thesis

The Volume-Of-Fluid method (VOF) together with the continuum surface force (CSF) approach for introducing the surface tension force (Brackbill et al.[27]) is one of the Eulerian techniques used to model a sharp interface in a continuum framework. It adds to mass and momentum conservation laws a transport equation of a colour function that locates the two phases, with the volume fraction being most often selected as that function. The method is popular both in academia and industry, as it typically requires less computational time and user intervention as compared to methods which use Lagrangian markers to represent the interface (e.g. the front-tracking method, Tryggvason et al.[28]). Another Eulerian method is the level-set method that uses a smoothed Heaviside function across the interface to solve for its movement and to compute the curvature[29], thus artificially diffusing the interface. The diffusive approach may lead to problem in mass conservation. Similarly, the phase-field approach is a diffuse-interface method which uses the chemical potential and solves the Cahn-Hilliard equation to introduce the inter-facial forces[30].

The advantages of using VOF in our framework, that is part of the code IPS IBOFlow®, we fully demonstrate in our publications. It is due to the ability to retain a sharp interface throughout the whole process of coalescing, that enables the framework to introduce and handle maximum refinement cells near the interface. With that resolution the framework becomes able to capture the three-dimensional effects of the high curvature locations and the transport of shape oscillations that are caused by its presence. This requires a highly accurate estimation of the curvature. To this regard, smoothening of the gradient of the volume fraction in the calculations for the curvature is used, as suggested by Brackbill et al. in their original publication. Alternative methods that permit an acceptably accurate estimation of curvature are the implementation of height functions and the geometric reconstruction of the interface. Testing the functionality of such methods in the research questions addressed in this work is certainly of potential interest. However, we are confident with the validation procedures we have undertaken and consider our current framework capable of reproducing the complex physics of jumping droplets in the entire range of spatial and temporal scales we have been interested in.

Moreover, the developing of the framework has involved the implementation of the balanced-force method to calculate the velocity at the faces of cells that are neighbouring to the interface location[31]. This implementation and its combination with the SIMPLEC segregated solver[32], as well as the CICSAM scheme[33] for the estimation of the advective velocity in the colour function equation, introduced a greatly improved estimation of the transport of interfaces at length-scales that often witness high spurious velocities in other VOF implementations.

The boundaries are modelled with an immersed boundary method. The mirrored IBM (MIBM) (Mark et al.[34]) takes into account the ghost cells velocity in order to set the exact required velocity at the wall. We have chosen a slip boundary condition at the superhydrophobic surface, following the Navier slip boundary that connects the velocity at the wall with the gradient of the velocity and the slip length. The slip length was chosen to be as high as the size of the adjacent cell on the wall, in order to obtain the best possible agreement with with the experimentally observed jumping velocity. We have also verified that the chosen slip length gave grid-independent results. Furthermore, the contact angle was imposed by setting the normal of the interface in the adjacent cell of a solid body. Within the CSF method, the normal vector of the interface is computed by the gradient of the volume fraction. For the cells which are adjacent to the wall, multiple cells in the vicinity of the contact line were used to impose the contact angle. This assumption is a fair one because the interface is not located in these cells and the transport equation for the volume fraction is not highly affected by the imposed direction of the gradient of the volume fraction in these cells. When the equation is solved for the mentioned cells, it does not influence the volume fraction computed for that cell, which should be a constant 0 or 1. The value of the contact angle was chosen with either a static formulation or using two contact-angle models, the so-called quasi-static that returns the advancing or receding value as taken from experimental data, or a fully dynamic contact angle model. In this study the latter one is the Kistler model, with an introduced modification in the correlated Hoffman equation[35] to account for the high contact angles on a superhydrophobic surface. For the last two schemes, the contact line velocity is required, which is computed by the tangential to the boundary part of the velocity at the adjacent cells to the solid boundary. The details of the contact angle implementation are described by Göhl et al.[36]. The method is also provided in Paper B.

3.2 Validation of the numerical framework

The validation of the framework has been independently performed for both publications in the thesis, in order to avoid any ambiguities related to its performance for each of the research questions treated. The time- and grid-independence investigations presented in the two papers eventually affirm a minimal influence to the results from slight variations of the time-step or the cell size, with regards to the benchmark setup that had been selected. We note here the connection between the slip length used in the Navier slip boundary condition and the grid convergence. When performing a grid study, the slip length was investigated according to the resulting jumping velocity. In other words, we have opted for that length to be a function of the droplet radius targeting that the jumping velocity remained constant. Alternative trials of grid convergence that were performed with a slip length varying according to the smallest cell size, and in effect keeping it equally proportional to the cell size, showed less consistency in the jumping velocity.

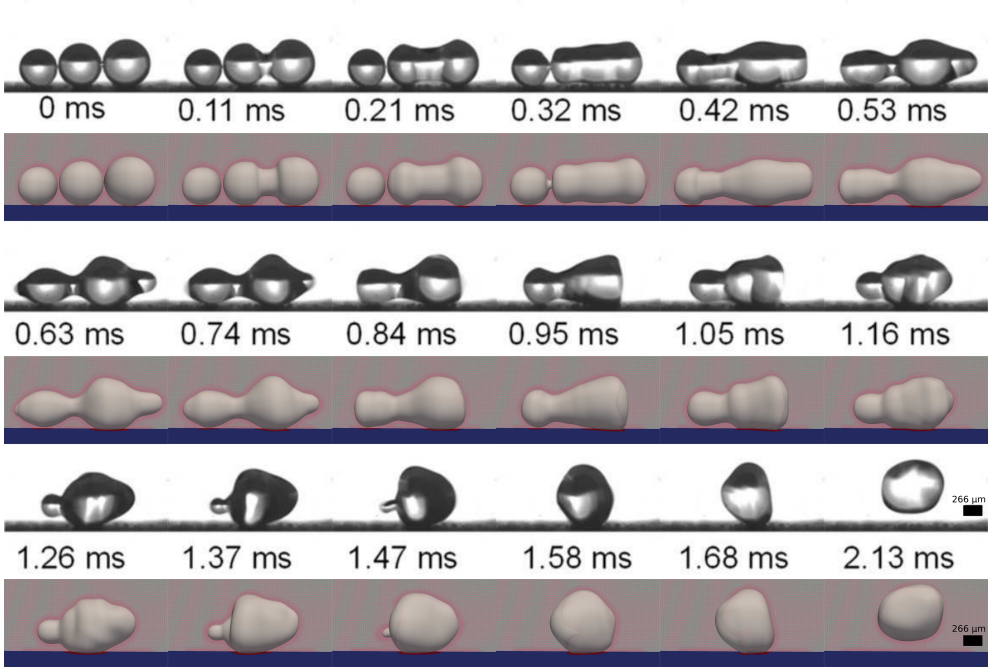

Figure 3.1: *A validation case with three unequal droplets coalescing and jumping. Note that a very good qualitative matching is obtained with experimental images by Yan et al[37] (with permission). We demonstrate a strong ability of the framework to capture the capillary effects for the interface and the merged droplet's shape oscillations.*

Among different validation studies presented in papers A and B, we have focused on the correspondence of the phenomenological behaviour of the simulated merged droplets to equivalent experimental cases. We have thus compared our simulation results with recorded videos from experimental studies of other authors that focus on elucidating different stages of the jumping droplets process. One such example is the case of coalescing of three unequal droplets and eventual jumping of a large merged one, see Fig. 3.1. The figures on the top represent experimental recordings, whereas the bottom ones are snapshots from our simulations. The goal for the simulations is to capture shape oscillations and the different stages of the process. We see that first the two larger droplets merge, but also that during their coalescing a liquid bridge with a third droplet is formed. We argue that the different shape deformations during the merging are well captured by our simulations, with the latter also adhering to the non-dimensional time-scales of the system. Moreover, the detachment of the final merged droplet appeared to take place similarly for both cases, with a limitation that only a single frame was publicly available from the experiment of Yan et al.[37]. This specific case demonstrates the abilities of our simulation tool regarding the interface capturing and advection. This also shows that we accurately represent the surface force near the interface, in an example where multiple locations of strong capillary forces exist in the domain at the regions of high curvature.

4 Selected results

This section will offer only some salient findings presented in the two papers of the thesis. In Paper A a thorough investigation is presented for microdroplets (with $R < 10$ µm) of the jumping velocity evolution, the energy budget and the final energy conversion of the available surface energy to translational upwards motion. A connection to the Ohnesorge non-dimensional number Oh is also presented with an intention to analyse up to what extent are the viscous forces the sole contributor of the dissipation in the non-linearly decreasing time-scales of the problem, as the radius of droplets decreases. A claim is made that the capillary forces do not showcase the same linear decrease with the decrease of the length scale of the problem, whereas the inertial forces do. This effect is noticed by a more rapid decrease in the surface energy for the case of microdroplets in comparison to larger droplets ($R = 100$ µm). It is suggested that the stronger influence of capillarity near the high curvature locations (or points with apparent dimples) is considered a key-factor for the more smoothed interface shape of the merged droplet for the microdroplet ($R = 1$ µm) case, while the inertial effects on the interface seem to be minimised. The analysis of the capillary number Ca and the Reynolds number Re introduces that inertia should still counter-act the viscous forces, while capillary forces are expected to dominate the physics of the problem.

The analysis of the energy budget from Figures 6 and 7 of the paper A brings into our knowledge that the coalescence of microdroplets experiences less oscillations in the transport of the kinetic energy than is the case for larger droplets. The re-distribution of the energy in the different directions, when the merged droplet oscillates between different oblate and prolate shapes, is documented with less noise but with a higher dissipation of the kinetic energy, in regards to the total available energy that was released from the surface energy of the initial droplets. These results are presented in Figure 4.1, where it is pointed out that the normalized jumping velocity is decreased by nearly 25% between the two droplet-size cases and that the energy conversion is down by 40%.

The second paper deals with the influence on the jumping process outcome of the modelled modes of interaction between a droplet and a wall, when this interaction is implemented through boundary conditions. We note an important effect of the type of contact-angle formulation and implementation, as well as the ability of the framework to dynamically adjust the contact-angle values. Therefore, several variations of the contact-angle formulations are presented in paper B, with an intention of pointing out how such formulations change the overall jumping droplets process and the jumping velocity when hysteresis is effectively introduced in the simulation. To account for the hysteresis effect, contact angles are implemented with the quasi-static method or with the Kistler model. Figure 4.2, found also in paper B, shows the changes of the jumping velocity with different contact-angle representations and for droplets of different initial sizes ($R = 200$ µm to 12.5 µm). The hysteresis introduced is for a superhydrophobic surface from Mulroe et al.[23], with a contact-angle hysteresis of $\Delta\theta = 15°$.

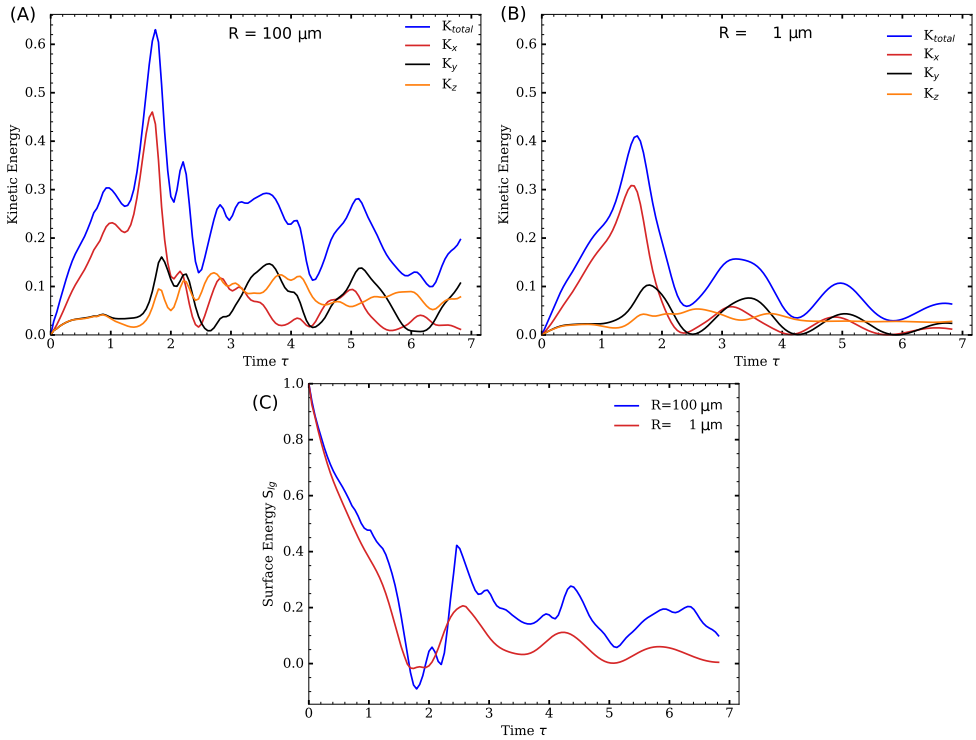

Figure 4.1: *The kinetic energy for a droplet of A) $R = 100$ μm and B) for $R = 1$ μm. The total kinetic energy of the merged droplet, shown together with the kinetic energy stored separately in each direction to observe the oscillations. C) The release of the available surface energy in the simulations of two droplet sizes. Observe considerably smoother oscillations in the microdroplet case with a more rapid release of the surface energy.*

The same figure shows that a relatively small decrease in the jumping velocity is present for a no-hysteresis case for $R \leq 25$ μm droplets, while a significantly increased reduction is introduced for all droplet sizes when hysteresis is present. Between the two ways to account for hysteresis, the Kistler model is showing a more pronounced decrease in the jumping velocity, something that led us to carry out a detailed analysis in Paper B of the advancing and receding movements of the contact line. We have observed that the nature of the Kistler model permits a much lower contact angle to be imposed in a receding case. As a result, during the detachment, where a rapid receding movement takes place, a strong deceleration for the merged droplet was identified, causing the eventual decrease in the jumping contact angle (compared to the case with the quasi-static method used).

Another significant observation in our results was that the merged droplet showed ability to re-attach to the surface after initial detachment. This sequence of detachment–re-attachment occurrences has been observed multiple times in certain cases during the coalescing process. We have also established a connection between the jumping velocity

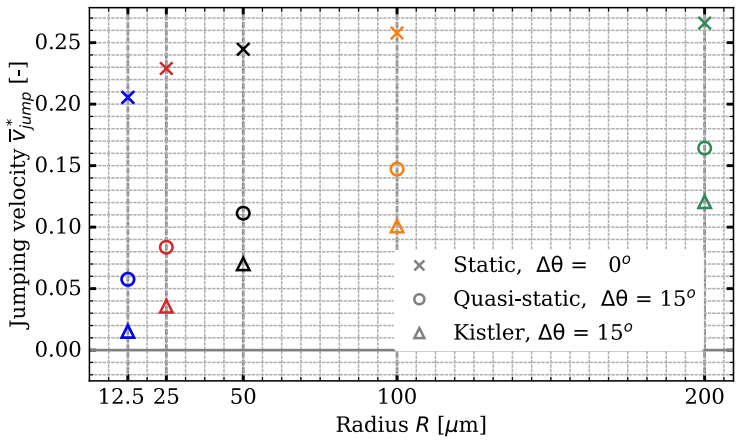

Figure 4.2: *The normalized jumping velocity for ve initial droplet radii (R between 12.5 and 200 µm). Note that the increasing degree of hysteresis leads to a signicant reduction in the jumping velocity.*

and the moments that the droplet detaches from the surface. The longer a merged droplet would stay attached to the surface, while a retracting oscillation from the surface takes place, the more reduction in the eventual jumping velocity is seen. An example of this behaviour would be for the cases with smaller droplets (R = 25 µm) and with higher hysteresis, where the jumping velocity was decreased up to the level that the velocity was neutralised after the last detachment.

5 Future prospects

The second part of the project will be focused on the interaction between the droplet interface and a solid particle, with an intended outcome to remove the particle from a superhydrophobic state. The plan for the first study case is to look at a droplet spreading over a hydrophilic particle, while it sits on a superhydrophobic surface. Recent developments in the field suggest that even for this case a bridge between the particle and the droplet will be formed at the capillary-inertial scales and an out-of-plane movement of the particle with the droplet can be observed.

Finally, a combination of the simultaneous coalescence of droplets and the interface capturing a particle before the droplets jump will be the final goal for this project. Then, a parametrization of surface properties will be investigated with numerous possible research strategies, for example to model pillars or to test different dynamic contact angle models and observe what cases would promise the best removal efficiency for particles of random shapes and different sizes.

6 Summary

In this thesis we have numerically studied a promising mechanism for self-cleaning that can be used in numerous technological applications. The mechanism involves superhydrophobic surfaces and droplets that are coalescing and jumping. The goal was to create a numerical framework that resolves in high resolution the important features of the droplet jumping phenomenon, something we deemed necessary before introducing solid particles (contaminants) in the framework. A first study, presented in Paper A, investigated jumping of microdroplets and provided important insights into the physical mechanisms that influence their jumping ability, with the focus on the energy budget.

We have shown that the framework is able to capture the surface tension force in the all the studied configurations and with an accuracy that is parallel or superior to the most highly reputed sharp interface codes. We have found that the transport and shape of the interface agree very well with experimental findings related to coalescing and jumping of droplets, showing a minimal loss of information. An investigation was also performed of the influence of substantial hysteresis present on a superhydrophobic surface and the contact-angle implementations on the dynamics of the jumping process. Among other things, we have proven that the overall process efficiency and the final jumping velocity of a merged droplet are as sensitive to the changes in the actual (i.e.true) contact-angle values as some experimental investigations were suggesting. It is concluded that the influence of the receding contact angle is substantial to the overall process performance, which justifies that great attention should be paid in any high-fidelity simulations to capturing its dynamic variations.

References

[1] C. Yu, S. Sasic, K. Liu, S. Salameh, R. H. Ras, and J. R. van Ommen. NatureInspired selfcleaning surfaces: Mechanisms, modelling, and manufacturing. *Chemical Engineering Research and Design* **155** (Mar. 2020), 48–65. DOI: 10.1016/j.cherd.2019.11.038.

[2] W. Barthlott and C. Neinhuis. Purity of the sacred lotus, or escape from contamination in biological surfaces. *Planta 1997 202:1* **202**.1 (1997), 1–8. DOI: 10.1007/s004250050096.

[3] K. M. Wisdom, J. A. Watson, X. Qu, F. Liu, G. S. Watson, and C.-H. Chen. Self-cleaning of superhydrophobic surfaces by self-propelled jumping condensate. *Proceedings of the National Academy of Sciences* **110**.20 (May 2013), 7992–7997. DOI: 10.1073/pnas.1210770110.

[4] S. Farhadi, M. Farzaneh, and S. A. Kulinich. Anti-icing performance of superhydrophobic surfaces. *Applied Surface Science* **257**.14 (May 2011), 6264–6269. DOI: 10.1016/j.apsusc.2011.02.057.

[5] P. Roach, N. J. Shirtcliffe, and M. I. Newton. Progess in superhydrophobic surface development. *Soft Matter* **4**.2 (Jan. 2008), 224. DOI: 10.1039/b712575p.

[6] S. Nishimoto and B. Bhushan. Bioinspired self-cleaning surfaces with superhydrophobicity, superoleophobicity, and superhydrophilicity. *RSC Advances* **3**.3 (2013), 671–690. DOI: 10.1039/c2ra21260a.

[7] S. P. Dalawai, M. A. Saad Aly, S. S. Latthe, R. Xing, R. S. Sutar, S. Nagappan, C. S. Ha, K. Kumar Sadasivuni, and S. Liu. Recent Advances in durability of superhydrophobic self-cleaning technology: A critical review. *Progress in Organic Coatings* **138** (Jan. 2020), 105381. DOI: 10.1016/j.porgcoat.2019.105381.

[8] N. Miljkovic, R. Enright, and E. N. Wang. Effect of droplet morphology on growth dynamics and heat transfer during condensation on superhydrophobic nanostructured surfaces. *ACS Nano* **6**.2 (2012), 1776–1785. DOI: 10.1021/nn205052a.

[9] H. Cha, S. Sett, P. Birbarah, T. Gebrael, J. Oh, and N. Miljkovic. Recent advances in structured surface enhanced condensation heat transfer. *Nanoscale Energy Transport* (Mar. 2020), 13–1–13–32. DOI: 10.1088/978-0-7503-1738-2ch13.

[10] J. B. Boreyko and C. H. Chen. Self-propelled dropwise condensate on superhydrophobic surfaces. *Physical Review Letters* **103**.18 (2009), 2–5. DOI: 10.1103/PhysRevLett.103.184501.

[11] S. Farokhirad and T. Lee. Computational study of microparticle effect on self-propelled jumping of droplets from superhydrophobic substrates. *International Journal of Multiphase Flow* **95** (2017), 220–234. DOI: 10.1016/j.ijmultiphaseflow.2017.05.008.

[12] C. Lv, P. Hao, X. Zhang, and F. He. Dewetting Transitions of Dropwise Condensation on Nanotexture-Enhanced Superhydrophobic Surfaces. *ACS Nano* **9**.12 (2015), 12311–12319. DOI: 10.1021/acsnano.5b05607.

[13] R. Mukherjee, A. S. Berrier, K. R. Murphy, J. R. Vieitez, and J. B. Boreyko. How Surface Orientation Affects Jumping-Droplet Condensation. *Joule* **3**.5 (2019), 1360–1376. DOI: 10.1016/j.joule.2019.03.004.

[14] D. J. Preston, D. L. Mafra, N. Miljkovic, J. Kong, and E. N. Wang. Scalable graphene coatings for enhanced condensation heat transfer. *Nano Letters* **15**.5 (May 2015), 2902–2909. DOI: 10.1021/nl504628s.

[15] N. Miljkovic, R. Enright, Y. Nam, K. Lopez, N. Dou, J. Sack, and E. N. Wang. Jumping-droplet-enhanced condensation on scalable superhydrophobic nanostructured surfaces. *Nano Letters* **13**.1 (Jan. 2013), 179–187. DOI: 10.1021/nl303835d.

[16] K. Rykaczewski, A. T. Paxson, S. Anand, X. Chen, Z. Wang, and K. K. Varanasi. Multimode multidrop serial coalescence effects during condensation on hierarchical superhydrophobic surfaces. *Langmuir* **29**.3 (2013), 881–891. DOI: 10.1021/la304264g.

[17] Y. Nam, H. Kim, and S. Shin. Energy and hydrodynamic analyses of coalescence-induced jumping droplets. *Applied Physics Letters* **103**.16 (Oct. 2013), 161601. DOI: 10.1063/1.4825273.

[18] F. Liu, G. Ghigliotti, J. J. Feng, and C.-H. Chen. Numerical simulations of self-propelled jumping upon drop coalescence on non-wetting surfaces. *Journal of Fluid Mechanics* **752** (Aug. 2014), 39–65. DOI: 10.1017/jfm.2014.320.

[19] F. Liu, G. Ghigliotti, J. J. Feng, and C. H. Chen. Self-propelled jumping upon drop coalescence on leidenfrost surfaces. *Journal of Fluid Mechanics* **752** (2014), 22–38. DOI: 10.1017/jfm.2014.319.

[20] A. B. D. Cassie and S. Baxter. Wettability of porous surfaces. *Transactions of the Faraday society* **40** (1944), 546–551.

[21] R. N. Wenzel. Resistance of solid surfaces to wetting by water. *Industrial & Engineering Chemistry* **28**.8 (1936), 988–994.

[22] H. Cha, C. Xu, J. Sotelo, J. M. Chun, Y. Yokoyama, R. Enright, and N. Miljkovic. Coalescence-induced nanodroplet jumping. *Physical Review Fluids* **1**.6 (Oct. 2016), 064102. DOI: 10.1103/PhysRevFluids.1.064102.

[23] M. D. Mulroe, B. R. Srijanto, S. F. Ahmadi, C. P. Collier, and J. B. Boreyko. Tuning Superhydrophobic Nanostructures To Enhance Jumping-Droplet Condensation. *ACS Nano* **11**.8 (Aug. 2017), 8499–8510. DOI: 10.1021/acsnano.7b04481.

[24] J. Wasserfall, P. Figueiredo, R. Kneer, W. Rohlfs, and P. Pischke. Coalescence-induced droplet jumping on superhydrophobic surfaces: Effects of droplet mismatch. *Physical Review Fluids* **2**.12 (2017), 1–17. DOI: 10.1103/PhysRevFluids.2.123601.

[25] R. Attarzadeh and A. Dolatabadi. Coalescence-induced jumping of micro-droplets on heterogeneous superhydrophobic surfaces. *Physics of Fluids* **29**.1 (Jan. 2017), 012104. DOI: 10.1063/1.4973823.

[26] C. Lv, P. Hao, Z. Yao, Y. Song, X. Zhang, and F. He. Condensation and jumping relay of droplets on lotus leaf. *Applied Physics Letters* **103**.2 (2013), 1–5. DOI: 10.1063/1.4812976.

[27] J. U. Brackbill, D. B. Kothe, and C. Zemach. A continuum method for modeling surface tension. *Journal of Computational Physics* **100**.2 (1992), 335–354. ISSN: 10902716. DOI: 10.1016/0021-9991(92)90240-Y.

[28] G. Tryggvason, B. Bunner, A. Esmaeeli, D. Juric, N. Al-Rawahi, W. Tauber, J. Han, S. Nas, and Y.-J. Jan. A Front-Tracking Method for the Computations of Multiphase Flow. *Journal of Computational Physics* **169**.2 (May 2001), 708–759. DOI: 10.1006/jcph.2001.6726.

[29] M. Sussman, P. Smereka, and S. Osher. A Level Set Approach for Computing Solutions to Incompressible Two-Phase Flow. *Journal of Computational Physics* **114**.1 (Sept. 1994), 146–159. DOI: 10.1006/jcph.1994.1155.

[30] D. M. Anderson, G. B. McFadden, and A. A. Wheeler. Diffuse-interface methods in fluid mechanics. *Annual Review of Fluid Mechanics* **30** (Nov. 1998), 139–165. DOI: 10.1146/annurev.fluid.30.1.139.

[31] M. M. Francois, S. J. Cummins, E. D. Dendy, D. B. Kothe, J. M. Sicilian, and M. W. Williams. A balanced-force algorithm for continuous and sharp interfacial surface tension models within a volume tracking framework. *Journal of Computational Physics* **213**.1 (Mar. 2006), 141–173. DOI: 10.1016/j.jcp.2005.08.004.

[32] S. V. Patankar. *Numerical Heat Transfer and Fluid Flow*. CRC Press, Taylor & Francis Group, Oct. 1980. DOI: 10.1201/9781482234213.

[33] O. Ubbink. "Numerical prediction of two fluid systems with sharp interfaces." PhD thesis. Imperial College London, 1997.

[34] A. Mark, R. Rundqvist, and F. Edelvik. Comparison between different immersed boundary conditions for simulation of complex fluid flows. *Fluid Dynamics and Materials Processing* **7**.3 (2011), 241–258. DOI: 10.3970/fdmp.2011.007.241.

[35] M. Jiang and B. Zhou. Improvement and further investigation on Hoffman-function-based dynamic contact angle model. *International Journal of Hydrogen Energy* **44**.31 (2019), 16898–16908. DOI: 10.1016/j.ijhydene.2019.04.256.

[36] J. Göhl, A. Mark, S. Sasic, and F. Edelvik. An immersed boundary based dynamic contact angle framework for handling complex surfaces of mixed wettabilities. *International Journal of Multiphase Flow* **109** (2018), 164–177. DOI: 10.1016/j.ijmultiphaseflow.2018.08.001.

[37] X. Yan, L. Zhang, S. Sett, L. Feng, C. Zhao, Z. Huang, H. Vahabi, A. K. Kota, F. Chen, and N. Miljkovic. Droplet Jumping: Effects of Droplet Size, Surface Structure, Pinning, and Liquid Properties. *ACS Nano* **13**.2 (Feb. 2019), 1309–1323. DOI: 10.1021/acsnano.8B06677.

[38] K. Konstantinidis, J. Göhl, A. Mark, and S. Sasic. Coalescence-induced jumping of microdroplets on superhydrophobic surfaces — A numerical study. *Canadian Journal of Chemical Engineering* **100**.12 (Dec. 2022), 3517–3530. DOI: 10.1002/cjce.24591.

[39] K. Konstantinidis, J. Göhl, A. Mark, and S. Sasic. Coalescence-induced jumping of droplets from superhydrophobic surfaces — The effect of contact-angle hysteresis. *Physics of Fluids* **34**.11 (Nov. 2022), 113302. DOI: 10.1063/5.0118645.

Part II

Appended Papers A–B

Paper A

Coalescence-induced jumping of microdroplets on superhydrophobic surfaces — A numerical study

K. Konstantinidis, J. Göhl, A. Mark, and S. Sasic. Coalescence-induced jumping of microdroplets on superhydrophobic surfaces — A numerical study. ***Canadian Journal of Chemical Engineering*** **100.12 (Dec. 2022), 3517–3530. DOI:** 10.1002/cjce.24591

Received: 28 February 2022 | Revised: 7 April 2022 | Accepted: 11 April 2022

DOI: 10.1002/cjce.24591

SPECIAL ISSUE ARTICLE

THE CANADIAN JOURNAL OF CHEMICAL ENGINEERING

Coalescence-induced jumping of microdroplets on superhydrophobic surfaces—A numerical study

Konstantinos Konstantinidis[1] | **Johan Göhl**[2] | **Andreas Mark**[2] | **Srdjan Sasic**[1]

[1]Department of Mechanics and Maritime Sciences, Division of Fluid Dynamics, Chalmers University of Technology, Gothenburg, Sweden

[2]Fraunhofer-Chalmers Centre, Chalmers Science Park, Gothenburg, Sweden

Correspondence
Konstantinos Konstantinidis, Department of Mechanics and Maritime Sciences, Division of Fluid Dynamics, Chalmers University of Technology, Gothenburg, 41296, Sweden.
Email: konkonst@chalmers.se

Funding information
Swedish National Infrastructure for Computing (SNIC); Swedish Research Council, Grant/Award Numbers: 2018-05973, 2019-04969

Abstract

We develop a numerical framework for simulating the coalescence and jumping of microdroplets on superhydrophobic surfaces. The framework combines the volume of fluid (VOF) method with models for advancing and receding contact angles on a number of superhydrophobic surfaces. We demonstrate the temporal and spatial convergence of the framework and show agreement between our numerical results and other experimental studies. The capillary-inertial scaling is investigated together with the existence of a cut-off behaviour frequently observed in the lower size-range of that regime. We investigate findings in some of the previous studies that the cut-off behaviour can be attributed to viscosity effects and dissipation due to interaction with surface microstructures. We exemplify specific features related to the jumping process and the corresponding energy budget analysis when microdroplets coalesce and jump. We have tested droplets of a radius as small as 0.5 μm that are still jumping but recorded a decrease in the jumping velocity and the degree of energy conversion compared to the jumping of larger droplets. We argue and prove that strong capillary forces originating from the high curvature oscillations dissipate the energy of the system significantly faster in the case of microdroplets.

KEYWORDS

contact angle, microdroplets, VOF–immersed boundary, wetting

1 | INTRODUCTION

The phenomenon of droplets jumping upon coalescence on superhydrophobic surfaces has been relatively recently observed.[1] It immediately attracted considerable research focus, as no external energy is required in order for the droplets to jump. The driving force behind the process is the combination of strong capillary forces, which are present during coalescence, and low adhesion to the surface, which is observed in the case of superhydrophobic surfaces.[2] The research activity related to jumping droplets has been steadily increasing for the last decade, with applications being found in, among others, anti-icing and defrosting technologies,[3–6] heat transfer from drop-wise condensation,[7,8] and various self-cleaning mechanisms.[9–12] Those technological applications are often inspired by mechanisms that have been observed in nature and that aim at providing benefits for animals and plants, such as water-repellency or self-cleaning.[13] Suitable examples in that manner are the lotus leaf[14,15] and the cicada wings.[16]

Coalescence and jumping of droplets on superhydrophobic surfaces have been investigated both experimentally and numerically. Studies agree that the properties of surface microstructures[17,18] or the number of coalescing droplets[19,20] are important factors in determining both the likelihood and the overall efficiency of the entire process. The jumping velocity follows the so-called capillary-inertial scaling law for droplet sizes where gravity can be deemed negligible.[1,2] Furthermore, while experimental studies have often demonstrated the necessity of having high droplet–surface contact angles for the jumping to take place, less attention has been paid to the influence of the hysteresis between the advancing and receding angles. In most cases, such hysteresis has been minimal.[17] A decrease in the value of the contact angle or an increase in the hysteresis causes the contact behaviour to change from a Cassie–Baxter to a partial Wenzel wetting one and a consequent impediment of jumping.[18] The Young's equation determines the ideal equilibrium state in which the triple contact line settles between gas, liquid, and solid phases.[21] This equation expresses the force acting at the liquid–solid interface, from which the adhesion energy is often calculated. When a droplet moves, a three-phase contact line is formed, and, as a consequence, there is a well-known problem for a chosen numerical framework to overcome the inability of the no-slip boundary condition to correctly represent the contact line movement and the induced stress singularity.[22–24] Various measures have been suggested to overcome this problem, including the so-called slip models and the Navier-slip boundary condition, the most popular among them.[22,25]

Moreover, there have been an increasing number of numerical studies looking at fundamental phenomena and characteristic features of the droplets jumping process.[26,27] Liu et al.[28] identified four stages that the merged droplet experiences during coalescence and jumping: (i) a liquid bridge expansion, (ii) acceleration upon impingement of the liquid bridge on a superhydrophobic surface, (iii) retraction of the merged droplet from the surface until the moment of departure, and (iv) deceleration of the merged droplet in air. Previous numerical studies have also shown that the jumping velocity follows the capillary-inertial scaling law.[28,29] These studies predicted jumping of droplets for even higher Ohnesorge numbers than did the early experimental works.[1] Here, it is worth noting that various multiphase flow frameworks have been used to study the jumping of droplets. A number of them have used continuum-based methods that focus on tracking or capturing the interface movement,[29–32] volume of fluid (VOF) probably being the most frequently used among them.[33–36] Surface tension is treated as a body force at the location of the interface, which categorizes VOF as a sharp-interface method. Using VOF, Wasserfal et al.[37] calculated 6% as the degree of energy conversion, the latter being defined as the amount of the released surface energy related to the kinetic energy, and also mentioned a reduction of that value when unequal droplets coalesce. Attarzadeh and Dolatabadi[38] looked at the jumping of droplets when the microstructures on a superhydrophobic surface were of sizes comparable to water droplets of around 20 μm. In addition to continuum-based frameworks, the meso-scale Lattice-Boltzmann approach has also been frequently used[26,39,40] to capture the jumping droplets process, with similar phenomena and stages of the process identified as in continuum-based simulations. Lastly, there have been studies using molecular dynamics (MD) simulations, focusing on molecular interactions of the droplets, the surrounding air, and the superhydrophobic surface.[41–43] The mentioned works dealt with nanodroplets of the radius of up to 50 nm. The observed behaviour of even small droplets was generally in line with that obtained using the continuum-based approaches with larger droplets.

The focus in most studies dealing with jumping droplets has so far been on those with a radius greater than 10 μm, see, for example, works of Boreyko and Chen, Nam et al. and Wen et al.[1,30,44] However, recent numerical and experimental studies have shown that jumping can occur for much smaller droplets of radii as small as 5, 1, or even 0.5 μm.[2,45–47] We term such droplets microdroplets, and they represent the main focus of this work. Microdroplets are of interest in numerous applications, such as those dealing with heat transfer rates through drop-wise condensation[48] and surfaces with antifogging abilities.[49] In the experimental works of Cha et al.[45] and Mulroe et al.,[46] the authors argued that the biggest obstacle for microdroplets to jump is due to the size of microstructures on superhydrophobic surfaces and their arrangement pattern on the top of such surfaces. On the other hand, there are both experimental[46] and numerical works[28,29,37] that confirm the jumping of droplets of sizes less than 1 μm, and, as it will be seen in what follows, the present work also corroborates such observations. Note that one of the difficulties in the experimental studies involving microdroplets can be a technical limitation in the frame rate when capturing the moment of jumping. In addition, the observed deviations for microdroplets in the velocity scaling from the capillary-inertial regime are usually attributed to an increase in the viscous dissipation.[1,50] As a result, the mentioned behaviour is explained by introducing a viscous cut-off region, above which the capillary-inertial law holds. This argument has been challenged as mentioned previously, with adhesion forces due to surface microstructures being considered of greater importance.[51,52]

Although the concept of a critical (minimum) size for a droplet to jump has been discussed before, there is still a lack of a systematic presentation of how the process of jumping takes place for microdroplets (those ranging from 500 nm to 10 μm will be the main focus of this work). The present paper thus aims at filling this gap, by formulating a comprehensive and trustworthy numerical framework that is thoroughly validated and has full control of the numerical aspects of the simulation process. We use a combined immersed boundary–VOF framework, accompanied by a dynamic contact-angle model, to investigate in detail and with sufficient resolution all the stages of the microdroplets jumping process. Such an approach is justified since experimental observations of these phenomena can be hindered by the small time scales of the process and whose capturing may become a significant challenge. Consequently, the goals of the present numerical simulations are (i) to find out whether microdroplets are able to jump at all upon coalescence on a number of tested superhydrophobic surfaces, (ii) to look into the details of the liquid–solid interaction and how the latter affects the jumping process, and finally, (iii) to investigate whether the observed capillary-inertial scaling law for larger droplets still holds for microdroplets, in comparison to experimental data (and the reasons for possible deviations). We do this by controlling both numerical and physical aspects that may cause variations in the jumping itself, the jumping velocity, and the energy conversion process that makes the upwards movement possible.

2 | METHODS

We make use of a combined immersed boundary–VOF method, implemented in our in-house code IPS IBOFlow®.[53] VOF is a single-fluid method that solves the incompressible Navier–Stokes equations

$$\nabla \cdot \mathbf{v} = 0,$$
$$\frac{\partial(\rho \mathbf{v})}{\partial t} + \mathbf{v} \cdot \nabla(\rho \mathbf{v}) = -\nabla p + \nabla \cdot (\mu \nabla \mathbf{v}) + \rho \mathbf{g} + \mathbf{f}_{SF}, \quad (1)$$

where $\mathbf{v}$ represents the velocity field, P is the pressure, $\mathbf{g}$ is the gravitational acceleration, $\mathbf{f}_{SF}$ is the surface tension force at the interface, ρ is the density, and μ is the dynamic viscosity. In order to track the interface location, a transport equation for the volume fraction is solved additionally, which reads as follows

$$\frac{\partial \alpha}{\partial t} + \mathbf{v} \cdot \nabla \alpha = 0, \quad (2)$$

where α is the volume fraction. The density and dynamic viscosity are volume averaged at the interface location, wherever a cell is partly occupied by the two fluids.

To model the surface tension, the continuum surface force (CSF) method[54] is used. A body force $\mathbf{f}_{SF}$ that is calculated for a computational cell at the interface is given as

$$\mathbf{f}_{SF} = \sigma \kappa \mathbf{n}, \quad (3)$$

where σ is the surface tension, $\mathbf{n}$ is the interface normal vector, and κ is the interface curvature.

The curvature is obtained by taking the divergence of the interface unit normal vector $\hat{\mathbf{n}}$ as

$$\kappa = -\nabla \cdot \hat{\mathbf{n}} = -\nabla \cdot \left(\frac{\mathbf{n}}{\| \mathbf{n} \|} \right), \quad (4)$$

where the interface normal vector $\mathbf{n}$ in the centre of a cell is calculated from the gradient of the volume fraction field as $\mathbf{n} = \nabla \alpha$.

Adaptive mesh refinement is utilized in the neighbouring regions of the interface and the solid surface. For the latter, the refinement is limited to the region of the surface around which the droplets are placed, in order to reduce the computational cost. Adaptive mesh refinement is implemented with a dynamically refined octree mesh, which has been used in our previous works.[53,55] The velocity and pressure fields are coupled with the help of the segregated semi-implicit method for pressure linked equations-consistent (SIMPLEC) algorithm.[56]

Additionally, we have implemented a balanced-force method,[57,58] which modifies the Rhie–Chow interpolation for face velocities[59] in co-located grid arrangements. The method accounts for the presence of surface tension when interpolating the velocities at the faces in order to reduce spurious currents and prevent pressure oscillations. It achieves that by improving the balance between surface tension and pressure gradient forces.

The solid surface is modelled by triangulated objects and the mirroring immersed boundary method.[53,60] The method is second-order accurate and is used to impose the local boundary conditions. It also enhances the surface force calculations by including the local boundary normal in the contact angle calculations.[55] A Navier-slip boundary condition is used to remove the stress singularity. The velocity of the liquid at the wall is given by

$$\mathbf{v}_{\text{wall}} = \lambda \left. \frac{\partial \mathbf{v}}{\partial n_{\text{w}}} \right|_{\text{wall}}, \quad (5)$$

where $\mathbf{v}_{wall}$ is the slip velocity at the wall, n_w is the normal direction to the wall, and λ is the slip length, understood as the distance from the boundary location to the hypothetical no-slip point. We calculate the slip velocity in the tangential direction and set it by the immersed boundary condition at the solid boundary.

Finally, the contact angle is implemented according to Göhl et al.[55] where a dynamic contact angle is imposed depending on whether the contact line is advancing or receding.

3 | VALIDATION OF OUR NUMERICAL FRAMEWORK

In this section, we wish to demonstrate and confirm the ability of our numerical framework to reproduce all fundamental features of the actual jumping process. Special attention is paid to identifying the exact movement of the interface and the corresponding forces. Moreover, we want to outline the difficulties and limitations encountered by all numerical frameworks when capturing the actual movement of the three-phase contact line and the corresponding dynamics of the contact angle. There is an additional challenge in correctly capturing the adhesion of droplets to the superhydrophobic surface and the changes in the behaviour of the contact line when the real geometry of the surface is considered.

The contact angle hysteresis is important in this process, and we focus more on that problem in what follows. In a previous study, Göhl et al.[55] successfully implemented and validated in IPS IBOFlow®, a dynamic contact angle framework able to make use of a number of different models for both advancing and receding contact angles. In this work, we use this framework to look specifically at the jumping of microdroplets on surfaces of different wettabilities and demonstrate its ability to recover fundamental features of jumping of larger droplets as well. In all the cases, we report that the framework recreated the conditions of the jumping process with a high accuracy, as the mass of water droplets in the simulations was conserved successfully. In addition, all fluid properties in the simulations were given actual values for a water–air system at 20°C, which corresponds to a density ratio of $\rho_l/\rho_g = 830$, a viscosity ratio of $\mu_l/\mu_g = 55$, and a surface tension of $\sigma = 0.0729$ N/m.

We now demonstrate the temporal and spatial convergence of our simulations. First, we present our motivation for the chosen time step. Two levels of adaptive interface refinements are used on the base grid, giving a minimum cell size of 2.5 μm. The minimum cell size is

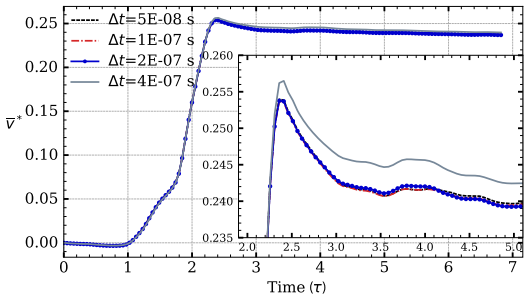

FIGURE 1 Demonstration of time convergence of our simulations. We note that the time convergence is achieved for a time step of $\Delta t = 2 \cdot 10^{-7}$ s or shorter. The initial radius of merging droplets is 100 μm and CFL < 0.7 for the simulation. CFL, Courant number

kept constant for the simulations presented in Figure 1. The time step Δt remained constant throughout each simulation, while the highest Courant number (CFL) number related to each time step varies depending on the maximum velocity. The time step Δt was varied from $2 \cdot 10^{-7}$ s down to $0.5 \cdot 10^{-7}$s. In this test case, the initial droplets have a radius (R) of 100 μm, and the minimum cell size corresponds to 40 cells per radius of the initial droplets, which is the resolution suggested by our grid convergence study. The vertical velocity of the jumping droplet was chosen as the parameter to observe when changing the simulation time step. In Figure 1, this velocity is normalized by the capillary-inertial velocity scale U_{CI}, whereas time is normalized by the capillary-inertial time scale τ_{CI}.

The largest time step reveals the same evolution of the average velocity as in the initial stage of the simulation. The maximum velocity occurs at $\tau = 2.4$, but the merged droplet detaches itself at an earlier time and it elevates at a higher velocity. The remaining simulations presented in Figure 1 show converged behaviour with respect to the time step. For the simulations with microdroplets, we will use a time step that follows the same principle as the simulation with $\Delta t = 1 \cdot 10^{-7}$ s, where CFL was limited to values below 0.35. However, some adjusting for the different sizes of the droplets in the domain is needed. We want here to accommodate the dependence of the compressive interface capturing scheme for arbitrary meshes (CICSAM) scheme on the CFL value, as this convective scheme relaxes the region of the convective boundness criterion. The scheme is able to accept CFL values of up to unity but switches to a different diffusive scheme for higher CFL values. It needs to be taken into consideration that the velocity is constant when it is normalized for the capillary-inertial regime.

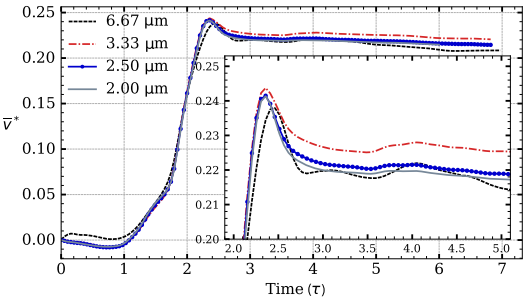

FIGURE 2 Demonstration of spatial convergence of our simulations. Adaptive mesh refinement is utilized, and the minimum cell size is defined. Grid convergence is achieved for a grid of 2.5 μm that corresponds to 40 cells per initial droplet radius. The radius of initial droplets is 100 μm and CFL < 0.35 for that simulation. CFL, Courant number

This results in having the same normalized time step $\Delta\tau$ for all such simulations that is given by:

$$\Delta\tau = \Delta t/\tau = \frac{1\cdot 10^{-7}\,\mathrm{s}}{\sqrt{\frac{\rho_l}{\sigma}}R^{\frac{3}{2}}} \simeq 0.051,$$

where $R = 100\,\mu\mathrm{m}$, or similarly

$$\Delta t = 1\cdot 10^{-7}(\mathrm{s})\left(\frac{R}{100\,(\mu\mathrm{m})}\right)^{\frac{3}{2}}.$$

To obtain the optimum grid size, we have again looked at the test case of 100 μm droplets. The time step is obtained from the previous time convergence study but adjusted depending on the minimum cell size to keep the same CFL number. The mesh is an octree-mesh, and the size of the cells is adjusted by choosing the base cell size and the number of refinement levels close to the interface. The coarsest grid has a minimum cell size, Δx, of 6.67 μm, which corresponds to a resolution of 15 cells across the initial droplet radius. To look at the required spatial resolution, we have subsequently tested 30 ($\Delta x = 3.33\,\mu\mathrm{m}$), 40 ($\Delta x = 2.5\,\mu\mathrm{m}$), and, finally, 50 ($\Delta x = 2.0\,\mu\mathrm{m}$) cells per R. Figure 2 shows the evolution of the vertical velocity of the system for the different simulations. The inset zooms the events close to the jumping moment and the first oscillations of the merged droplet while being elevated in the air. The Navier-slip boundary condition was used with a given constant slip length l_{sl} of half the length of the cell size, which is $l_{sl} = 1.0\mu\mathrm{m}$. The slip length of half a cell size is often chosen in similar studies.[61]

In Figure 2, it is revealed that the coarsest grid (shown with the black dashed line) has missed the initial behaviour of the liquid bridge expansion, while it overshoots the moment of the highest velocity, as well as the peak. The remaining grid resolutions have the same evolution of the coalescing stage. In the zoomed-in plot, it is understood that the case of $\Delta x = 3.33$ μm has predicted an earlier release from the superhydrophobic surface. Therefore, a greater upwards velocity was preserved during the stage of deceleration, and the droplet jumped with a higher velocity. The two cases of finer refinements showcase the same behaviour throughout the simulation, and the jumping velocity is calculated to be within 0.8% of each other. For these reasons, the spatial resolution of the simulations in the remainder of the article will follow the rule of 40 cells per radius of the initial droplets.

Finally, we continue the validation of our framework by comparing the simulation results with experimental results obtained by another research group. In Figure 3, we present a series of experimentally obtained camera images taken at different instants by Yan et al.,[17] together with the corresponding snapshots from our simulations. The figure depicts the evolution of the process of coalescing and jumping of two equal droplets with a radius of 288 μm, which are placed on a superhydrophobic, nanostructured surface (Yan et al.[17] Figure 1B). The advancing and receding contact angles are $\theta_{adv} = 170.3^\circ$ and $\theta_{rec} = 167.7^\circ$, respectively. The resemblance of the behaviour of the jumping droplets in all the phases of the process is apparent in Figure 3. In the second comparison from the top ($t = 0.29$ ms), we show the liquid bridge expansion. The qualitative analysis shows a good agreement between the simulation and the experiment. A slight variation in the times presented can be attributed to possible errors in the image-capturing process. The following two snapshots present the impingement of the liquid bridge on the surface and the formation of an oblate droplet until the point when the contact line starts retracting. We note that we accurately capture the oscillations of the shape of the merged droplet, which have been captured by the experiment. Next, the snapshots at approximately $t \simeq 1.4$ and 1.6 ms show moments just before and right after the detachment of the merged droplet from the surface. The oscillations are portraying rapid shape changes during the detachment. As a result, the captured image could incorporate a slight distortion, which can be an effect of the limitation imposed by the shutter speed. Nonetheless, we see that the shapes of the merged droplets coincide, with the moment of detachment predicted by our simulation with high precision. Finally, the last two frames present the resulting droplets elevating in the air, depicting similar shape oscillations in the qualitative comparison of the two systems. In

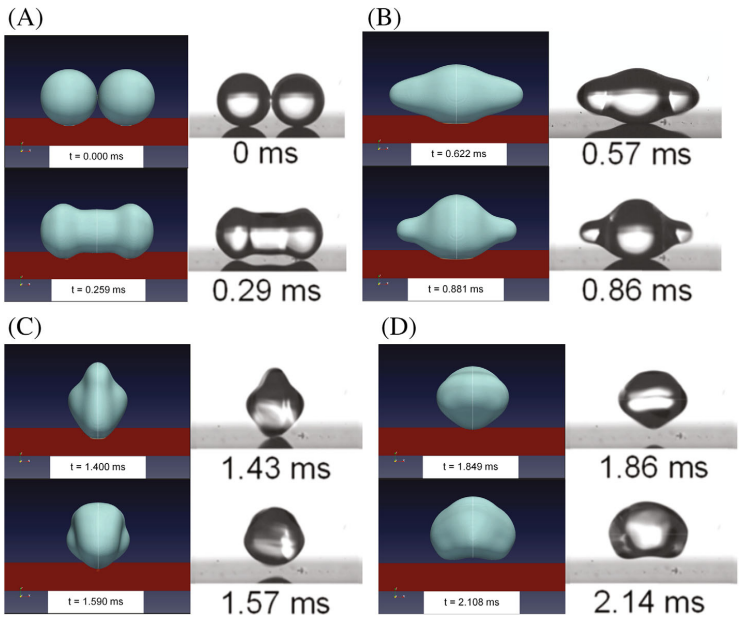

FIGURE 3 Validation by comparing our simulation results with an experiment from Yan et al.[17] Equally sized droplets of an initial radius $R = 288$ μm are presented at different instants throughout the jumping process. The timestamps of the simulation follow the values provided in the experimental study. We observe a high qualitative agreement of the jumping behaviour between our simulation and the experiment.

summary, we argue that the shapes of the droplets and the overall analysis of the jumping process obtained by our simulation highly agree with the published information from the experimental study. This makes it possible for us to now turn our attention to the main topic of our paper, which is the coalescence and jumping of microdroplets on superhydrophobic surfaces.

4 | RESULTS AND DISCUSSION

We first simulate the jumping of 1 μm microdroplets and present the snapshots of this simulation in Figure 4, together with the equivalent ones for the case of $R = 100$ μm droplets and given for the same non-dimensional time τ. The liquid bridge expands during the first stage of coalescence for both cases ($\tau = 0.51$). The merged droplet obtains an oblate shape along the axis of droplets initial centres ($\tau = 0.62$). We observe the higher relative curvature of the merged droplet for the 100 μm case. Such a droplet exhibits a higher degree of expansion per radius compared to the case of microdroplets. In both cases, the liquid bridge hits upon the superhydrophobic surface and the merged droplet expands its contact area up to a certain point ($\tau = 1.28$). During this stage, the shape of the microdroplet does not experience some of the features that appear in the larger droplet case, such as oscillations of the interface and formations of dimple shapes. The latter can be explained by the existence of strong inertial forces that counteract the capillary forces at the interface. The effect of capillarity is enhanced at areas of the interface where the droplet is experiencing local maxima of the curvature. In contrast, inertia does not produce the same effect on the microdroplet, in which case the curvature is retained lower. At $\tau = 1.75$, the mass of the droplet moves from the x-direction towards the y- and z-directions (see Figure 4), with that movement being impeded by the existence of the solid surface. Furthermore, the droplet begins retracting from the surface. The interaction of momentum in the z-direction with the surface will create an upwards motion that will reach a maximum vertical velocity around $\tau = 2.3$ as it is shown in Figure 5. It is interesting to point out that the peak velocity is attained slightly earlier for the microdroplet case. Subsequently, the merged droplet experiences deceleration, while the contact area with the surface continues to reduce until the moment the droplet jumps. We note that the detachment is experienced earlier by the larger droplet at $\tau = 2.5$, while for the microdroplet, it takes place at $\tau = 2.7$. Specifically, a deceleration of 15% is observed for the latter while the jumping velocity of the larger droplet is only decreased by 4%. The deceleration phase spans until moments after jumping, because of the existence of a low-pressure area beneath the merged droplet and due to oscillations. Following that phase, the jumping droplet has obtained its travelling velocity through air. This velocity differs for the two cases, as in the case of larger droplets, the gravity and inertia will dictate the

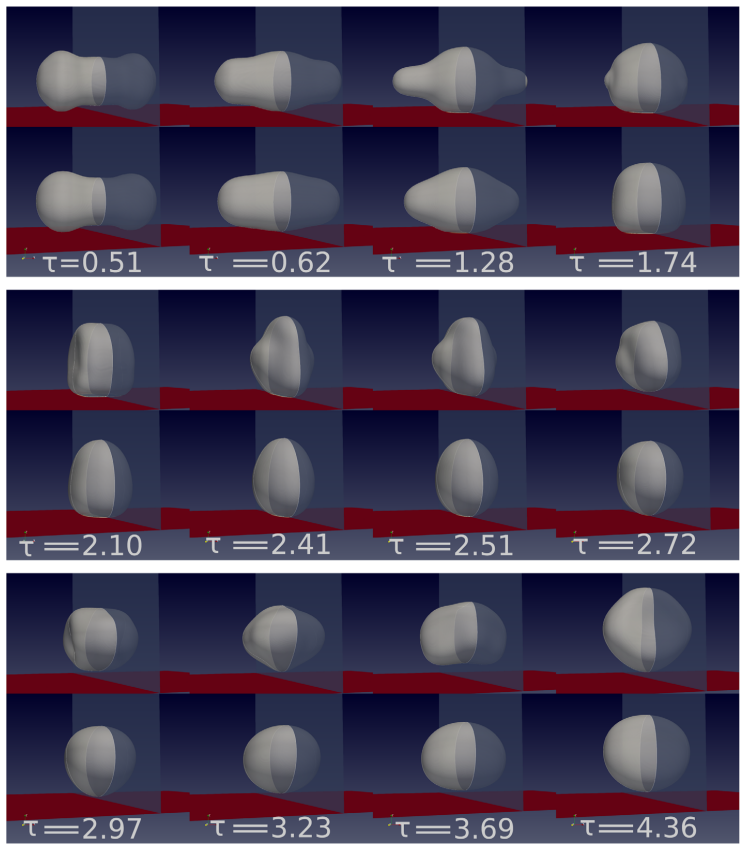

FIGURE 4 Comparison between different stages of jumping of droplets with an initial radius of $R = 100\,\mu m$ (top row in subfigures) and $R = 1\,\mu m$ (bottom row in subfigures). The snapshots are made at instants that correspond to equivalent non-dimensional capillary-inertial time-scales. Oscillations are less apparent in the microdroplet case. We also note the absence of high-curvature locations in comparison to the $R = 100\,\mu m$ case.

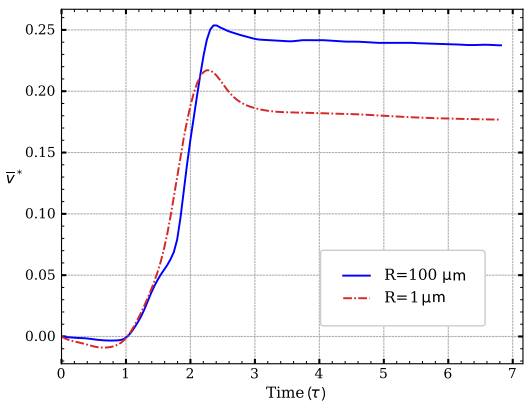

FIGURE 5 Evolution of the vertical velocity for the droplets with $R = 100\,\mu m$ and $R = 1\,\mu m$. Time and velocity are normalized with the capillary-inertial scales. There is a decrease in the jumping velocity for the microdroplet, while the latter is launched at a later moment than the larger one.

movement, while for the microdroplets, the viscous forces are most dominant. Note that the effect of viscous forces is not equally dominant in the jumping of the two types of droplets, since the time scales are dependent on $R^{3/2}$. In such cases, the accuracy of the numerical framework becomes particularly important because it is what makes it possible for us to gain an understanding of the dissipative behaviour during and following the jumping process.

It is also useful to look at the energy budget of the process. Figure 6A,B depict the total kinetic energies during the jumping of microdroplets and larger droplets, respectively. For each case, the kinetic energies of the velocity components are also presented in order to understand in which direction the greater amount of the released surface energy has been absorbed. In addition, the reduction in the surface energy, which is given to the merged droplet due to the surface tension of the water–air interface, is shown in Figure 7. At the beginning of the merging process, the majority of the

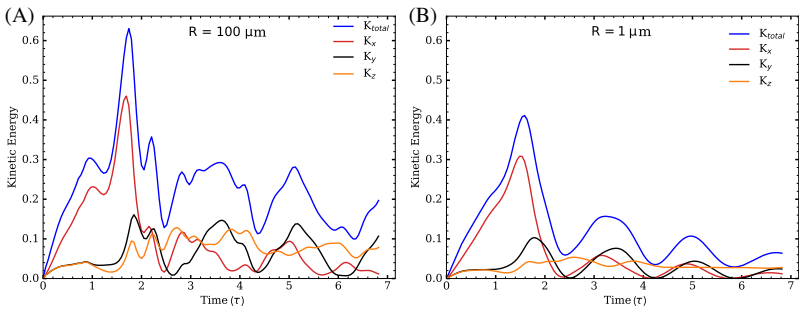

FIGURE 6 Total kinetic energies (K_{total}) in the system normalized by the available released surface energy. The kinetic energies computed by the direction components of the velocity (K_i) are superimposed. Figure (A) corresponds to the $R = 100$ μm droplets case and figure (B) to droplets of $R = 1$ μm. The maximum percentage of the available energy that was given as the kinetic energy in the system for the microdroplets is significantly reduced compared to that in the larger droplet case.

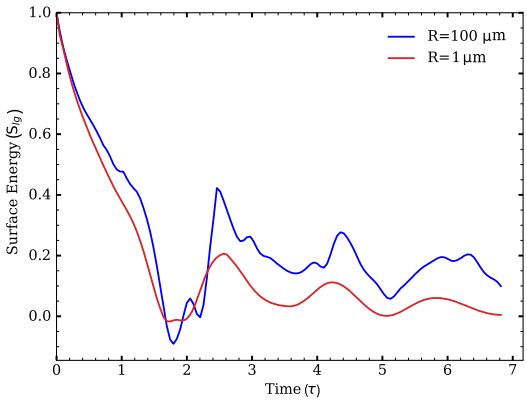

FIGURE 7 Surface energies (S_{lg}) for the $R = 100$ μm and $R = 1$ μm cases. The energies are computed from the interface area of the water–air interaction and are normalized by the available released surface energy for each case. A higher percentage of the available energy has been released during the early jumping stage for $R = 1$ μm droplets.

released surface energy is transformed to kinetic energy in the *x*-direction. A microdroplet is somewhat less efficient in this process than a larger one, as a smaller percentage of its available energy transforms to the kinetic energy. After the droplet goes through the initial stage of expansion in the x-direction until $\tau = 1.3$ and then rapidly retracts up to $\tau = 2.0$, the kinetic energy in the system is experiencing a steep decrease. Such an observation implies that the energy in the system is stored as the surface energy at either the interface or at the contact area with the solid surface. It is noted that the merged microdroplet during this process has experienced a higher surface energy release in the initial stage of its expansion on the superhydrophobic surface. This suggests that either the energy could not be stored at the surface due to extreme capillary forces at high curvature areas or that it has already dissipated due to viscosity after the initial phase, during which the released surface energy is given as momentum in the system. Therefore, viscosity is one of the assisting reasons that causes the velocity of the capillary wave to decrease, before the latter could reach the low curvature area of the interface.

Even though the process as a whole is adhering to the capillary-inertial regime by following the corresponding velocity and time scales, the higher dissipated energy in the microdroplet case could be attributed to either viscous forces or the effect of the surface tension that limits inertia at high curvature areas of the interface. An explanation for the latter would be that the peak capillary forces do not scale with *R* as the radius of the droplets decreases, but with a power of n^{-1}, where $n > 1$.

For the final energy that will be converted to upwards motion, the efficiency is given by the percentage of the available energy that is transformed to the translational kinetic energy of the merged droplet in the vertical direction. The available energy in the system is the difference between the energy of the initial interface area of the coalescing droplets and the reduced surface energy of the jumping merged droplet when the latter finally obtains a spherical shape. For the case of the initial droplets of 100 μm, the energy conversion to the jumping motion was calculated as 4.8%, while for the $R = 1$ μm case, it was obtained to be 2.8%. For even smaller initial droplets of 0.5 μm, the conversion was 2.8%. The results signify that the efficiency is markedly decreased for the jumping of microdroplets, even though they still manage to be expelled from the surface. Comparing the behaviour of

the kinetic and surface energies in Figures 6 and 7, it is suggested that during the initial stage of merging, when the liquid bridge expands and after its impingement on the surface, the merged droplet extends its contact area with the superhydrophobic surface. As a result, and comparing the two cases, the larger droplets receive a higher percentage of the released surface energy in the form of the total kinetic energy.

So far, we have established that microdroplets coalesce and can effectively jump, although they do it with a reduced jumping velocity and energy conversion rate. Observations from these simulations may appear contradicting to some of the previous experimental and numerical results, which emphasize that a viscous cut-off is causing the merged droplet to adhere to the surface.[1,51,52] The Ohnesorge number (Oh), given by Equation (6), compares the viscous forces with the geometric mean of inertial and capillary forces.

$$\text{Ohnesorge Oh} = \frac{\mu}{\rho\sigma R} \sim \frac{\text{Viscous forces}}{\sqrt{\text{Inertia} \cdot \text{Capillary}}} \tag{6}$$

This nondimensional number shows that, for the viscosity to completely dampen any effects arising from high capillary forces during coalescence, it has to be comparable to both surface tension and inertia. The Weber number (We), given in Equation (7), informs us of the relative importance of inertial forces to capillary ones.

$$\text{Weber We} = \frac{\rho V^2 R}{\sigma} \sim \frac{\text{Inertia}}{\text{Capillary}} \tag{7}$$

As it is seen in both our work and in previous studies, in the capillary-inertial regime, the process follows a certain scaling with regards to the velocity and time. With a constant normalized jumping velocity $\overline{v}^*_{\text{jump}}$, we have $\text{We} = \overline{v}^{*\,2}_{\text{jump}}$, which is also a constant value. If $\overline{v}^*_{\text{jump}}$ is approximately 0.24, as it has been observed for droplets larger than 20 μm, then the Weber number becomes We = 0.058. Such a low value shows the dominance of capillary forces in this regime and that the two forces scale the same way with regards to the governing length scale of the system. The observation further suggests that when the length scale is reduced and a decrease in the non-dimensional velocity is observed, the Weber number will decrease even further.

To complete this analysis, a thorough understanding is required of the role of Reynolds (Re) and capillary (Ca) non-dimensional numbers, which are defined as in Equations (8) and (9), respectively.

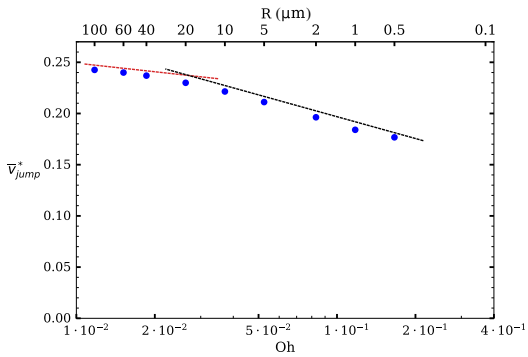

FIGURE 8 Normalized jumping velocities for the simulations involving droplets of varying initial radius as a function of the Ohnesorge number (log-scale). The red and black dashed lines represent the trends (i.e., different slopes) on a logarithmic scale for the jumping velocity of the larger- and microdroplets, respectively. We note that the jumping speed declines faster for droplets with radii corresponding to the Ohnesorge number of 0.03 and greater (initial droplets of 20 μm as the onset of this behaviour) in comparison to the larger droplets.

$$\text{Reynolds Re} = \frac{\rho V R}{\mu} \sim \frac{\text{Inertia}}{\text{Viscous forces}} \tag{8}$$

$$\text{Capillary Ca} = \frac{\mu V}{\sigma} \sim \frac{\text{Viscous forces}}{\text{Capillary}} \tag{9}$$

In the case of the jumping microdroplet with an initial radius of 1 μm, the jumping velocity was $\overline{v}^*_{\text{jump}} = 0.185$. This translates to Re = 1.4 and Ca = 0.024,which for the average velocity of the system indicates that the inertial forces may still be of higher importance than the viscous ones. It also indicates that at these length scales, the two types of forces are of comparable magnitude. On the other hand, the capillary forces are still some 40 times greater than the viscous ones and dictate the behaviour during coalescence. Since the Ohnesorge number can be expressed as $\text{Oh} = \sqrt{\frac{\text{Ca}}{\text{Re}}}$, we argue that even though a cut-off radius has been observed in previous studies, and as long as the viscous forces are not dominant, the capillary forces will overcome any effects from the viscosity. The analysis suggests that a significant part of the surface energy will be given as the kinetic energy to the system, and the coalesced droplets will eventually jump. For these reasons, as it will be shown later in the article, we interpret the notion of a cut-off radius to be caused by the interaction of a droplet with a superhydrophobic surface and the relative size of the microdroplets to the microstructures or nanostructures that exist on these surfaces.

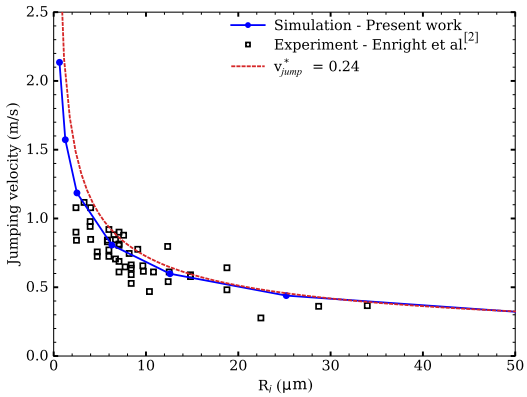

FIGURE 9 Jumping velocities for merged droplets of different radius. The simulation results are compared to the experimental data for jumping droplets by Enright et al.[2] The dashed curve represents a constant jumping velocity of 0.24 U_{CI}.

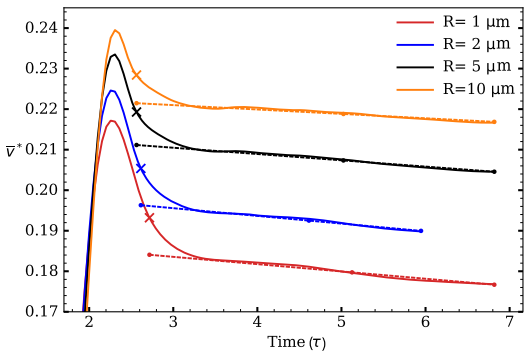

FIGURE 10 Normalized jumping velocities for four different microdroplets obtained by the simulations. The solid lines represent the average vertical velocity, and the crosses indicate the jumping moments. The dashed lines show the linear decrease in the velocity after detachment. The velocity is extrapolated backwards to the point of detachment, giving the jumping velocity.

Connecting our previous discussion on what happens at such small scales to the corresponding Ohnesorge numbers, simulations have been performed for droplets of an initial radius ranging from 0.5 to 60 μm. The obtained results for the jumping velocity are presented in Figure 8, with respect to the Ohnesorge number and with the sizes of the initial droplets indicated on the top of the figure. We note that the calculated velocities decrease as the radius decreases but observe a steeper decrease for droplets smaller than 20 μm (corresponding to the Ohnesorge number of 0.03). Additionally, we compare our results to experimental results for equivalent droplet sizes

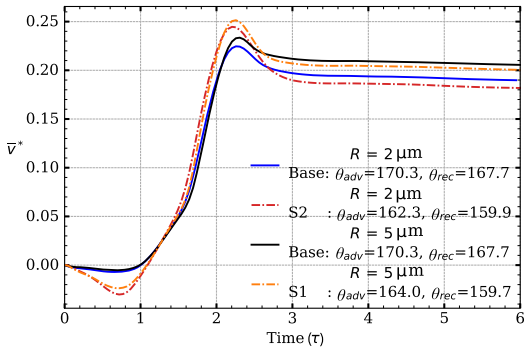

FIGURE 11 Simulations of jumping of 2 and 5 μm droplets on surfaces with different wettabilities (smaller contact angles and a more pronounced hysteresis). The contact angle values correspond to the surfaces S1 and S2 in Mulroe et al.[46] The simulations were performed using the minimum radius for which jumping was observed in the experiments. The obtained results are then compared to those with the base case contact angle values.

by Enright et al.[2] In Figure 9, the jumping velocity of the droplets is depicted, alongside the data from the mentioned experimental study and a curve that corresponds to a constant normalized jumping velocity of $\bar{v}^*_{\text{jump}} = 0.24$. The figure demonstrates the ability of our framework to capture the behaviour of the jumping velocity that has been observed in the experiment. The experimental results were obtained for similar advancing and receding contact angles ($\theta_{\text{adv}} \simeq 170.2^\circ$ and $\theta_{\text{rec}} \simeq 166^\circ$) with nanostructures of up to 0.82 μm on the superhydrophobic surface. The simulation results are provided with respect to the merged droplets radius as the experimental study suggested.

It is also of interest to explain how the jumping velocity is obtained from the simulations. The droplet is considered detached from the surface when all computational cells adjacent to the surface are filled with air. The evolution of the average velocity in the vertical direction is given in Figure 10, and the point of detachment is noted with an ×-symbol. The velocity is plotted for the cases of 1, 2, 5, and 10 μm of the coalescing droplets. The linear decrease in the velocity is extrapolated backwards to the moment of detachment in order to yield the considered jumping velocity, $\bar{v}^*_{\text{jump}}$, for the merged droplet. The jumping velocities presented previously in Figures 8 and 9 are extracted in the same way.

All our simulation cases of the jumping of microdroplets up to now have involved superhydrophobic surfaces with a slight hysteresis and with very high contact angles. The final part of our analysis is thus obtained by changing the surface wetting properties. We first simulate a

case with a similar hysteresis but with lower advancing and receding contact angles. We then proceed by looking at the influence of a more pronounced hysteresis. For that purpose, the previously shown results (that we here term the base case) are compared with the simulations that take the contact angle values from the experimental study of Mulroe et al.[46] Two different surfaces from that work are used, termed S1 and S2, and their wetting properties differ because of changes in surface microstructure. For the surface S1, $\theta_{adv} = 164.0^{\circ}$ and $\theta_{rec} = 159.7^{\circ}$, we look at the jumping of 5 μm microdroplets, whereas for S2, $\theta_{adv} = 162.3^{\circ}$ and $\theta_{rec} = 159.9^{\circ}$, the jumping of 2 μm microdroplets is investigated. In the cited experimental work, the reported 2 and 5 μm droplets were the minimal observed sizes of droplets that indeed jumped on S1 and S2. In Figure 11, we compare the simulation results using the mentioned droplet sizes from the two surfaces with the results acquired using the surface properties of our base case simulations. During the initial stage of the process, the microdroplets on the S1 and S2 surfaces show a more pronounced adhesive behaviour when the liquid bridge expands, directing their mass towards the surface. The relaxation of the effective contact angle in the system from its initialization value, which was set as a mean of the advancing and receding angles, to the receding value for the start of coalescence, is the most probable cause of this behaviour. In addition, the centre mass of the droplets, in comparison with the base case, is located closer to the surface due to the smaller contact angle. This results in a stronger interaction of the liquid bridge with the trapped air between the bridge and the surface. When the liquid bridge impinges on the surface and the merged droplet mass is accelerated upwards, a steeper increase in the velocity is identified for the cases involving surfaces S1 and S2. This behaviour continues until it results in a higher maximum velocity. We notice this response for both the 5 μm droplets on surface S1 and for the 2 μm droplet case on S2. Such an observation is also in accordance with the previously documented behaviour, both experimentally[44,62,63] and numerically,[35,39,64] that earlier the liquid bridge hits upon a surface during its expansion phase, the higher is the reaction energy that the merged droplet will obtain. That happens either when there is a geometrical obstacle beneath the main direction of the liquid bridge expansion, or when the centre of mass of the initial droplets is brought closer to the surface (which in this case occurs because the initial contact angle value of approximately 162◦ is lower than 169◦ for the base case surface). After the peak of the upwards velocity is reached, the droplet goes through another adhesion phase with the receding behaviour, while it takes longer to detach compared to the surface of the base case simulations. When the merged droplet has eventually detached, we observe a lower average jumping velocity, but the same deceleration rate while airborne for the simulations with different surfaces. It is important to point out that for both 2 and 5 μm cases, the droplets jumped with a smaller velocity, something that can most likely be attributed to the smaller receding angle that causes dissipation of energy before the merged droplets are released.

In summary, we have shown that a carefully formulated (with respect to the governing physics) and thoroughly validated numerical framework is able to predict the jumping of droplets of a radius as small as 0.5 μm. We have compared the behaviour of such microdroplets with the jumping of larger droplets in the capillary-inertial scaling regime that follows the constant normalized jumping velocity. Finally, it has been shown that capillary forces and viscous dissipation, to a lesser extent, are indeed factors behind the lost likelihood of the jumping of microdroplets, but in the present analysis, we point out that the main reason behind the experimentally observed existence of a cut-off radius is the surface-droplet interaction with microstructures.

5 | CONCLUSIONS

In this work, we formulated and validated a numerical framework for coalescence and jumping of microdroplets (smaller than 10 μm) on superhydrophobic surfaces. The combined VOF–immersed boundary framework involves models for advancing and receding contact angles on a number of superhydrophobic surfaces with different wetting properties. We performed a series of simulations to explain variations in the behaviour of the droplets whose size is in the lower length-scale region of the capillary-inertial scaling regime. We showed that microdroplets can jump successfully, but, as compared to the jumping of larger droplets ($\sim$100μm), they do this with a decreased normalized jumping velocity and a smaller degree of the released surface energy converted to the kinetic energy of an upwards movement.

Our temporal and spatial convergence studies motivate using 40 cells per initial droplet radius and a constant time step that assures that we always work with a CFL smaller than 0.5. In all our simulation cases, we used adaptive mesh refinement to improve accuracy near the interface and the moving contact line. The framework was further validated by presenting a good qualitative agreement with the experimental evidence for all the stages of the jumping process for $R = 288$ μm droplets.[17]

Our results showed that for 1 μm microdroplets, a smaller degree of the total energy is given as kinetic energy in the initial stage of the process, as compared to

the jumping of larger droplets. During a droplet jumping process, in general, it is known that a part of the kinetic energy is returned to the surface energy and vice versa during the oscillation of a coalesced droplet. We observed that this exchange happens less efficiently in the case of microdroplets. It is possible that viscosity is an important mechanism behind dissipation, but we argue that another important reason is that the peak capillary forces at high curvature locations may not follow the capillary-inertial scaling with a droplet radius. Instead, they show an increased strength in comparison to those during the jumping of larger droplets. For the jumping of $R = 100\,\mu m$ droplets, we calculated the degree of energy conversion to an upwards movement to be approximately 5%. We showed that this number is generally reduced to a half for microdroplets.

Through an analysis of the Ohnesorge number and a comparison of the inertial and capillary forces as a function of viscosity, we concluded not only that the capillary forces are the main driving mechanism behind the microdroplets jumping process but also that inertia is still an important factor. In that sense, we note that the Reynolds number is greater than unity, calculated with the average jumping velocity at $R = 100\,\mu m$. Our findings are in contrast with some previous studies, which suggest that viscous forces are behind the existence of a cut-off region (a set of values for which droplets of certain sizes can jump). We argue instead that the dissipation that has been observed at such scales in previous experimental studies is due to interactions with microstructures on the surface.

We also presented the simulations of jumping of microdroplets with an initial radius of as small as $R = 0.5\,\mu m$ and compared their jumping velocities with the experimental findings of another research group.[2] The simulations accurately reproduced the experimental observations even in the case of such small droplets.

Finally, we looked at the fundamentals of the microdroplet jumping process when a more pronounced hysteresis of contact angles is present not only on superhydrophobic surfaces but also on surfaces with a smaller degree of superhydrophobicity. For that purpose, we ran the simulations of 2 and 5 μm droplets and proved that, by considering the superhydrophobic surface as flat and correctly assigning the corresponding contact angles, the droplets will manage to jump with a reduction in their velocity and small variations in the jumping process (mostly in the form of a more pronounced adhesive behaviour during the expansion of a liquid bridge).

NOMENCLATURE

$\hat{\mathbf{n}}$	unit interface normal vector (−)
$\mathbf{f}_{SF}$	surface tension body force ($kg \cdot m^{-2} \cdot s^{-2}$)
$\mathbf{n}$	interface normal vector (m^{-1})
$\mathbf{v}$	velocity ($m \cdot s^{-1}$)
$\mathbf{v}_{wall}$	slip velocity at wall ($m \cdot s^{-1}$)
K_i	normalized kinetic energy in direction i (−)
K_{total}	normalized total kinetic energy normalized (−)
S_{lg}	normalized surface energy in the liquid–gas interface (−)
$\bar{v}^*$	averaged normalized vertical velocity of droplet (−)
$\bar{v}^*_{jump}$	normalized jumping velocity of droplet (−)
Ca	capillary number (−)
g	gravitational acceleration ($m \cdot s^{-2}$)
n_w	normal wall direction (m)
Oh	Ohnesorge number (−)
p	pressure ($kg \cdot m^{-1} \cdot s^{-2}$)
R	radius of initial droplets (m)
R_c	radius of merged droplet (m)
Re	Reynolds number (−)
t	time (s)
U_{CI}	normalized capillary-inertial velocity (−)
We	Weber number (−)

Greek letters

α	volume fraction (−)
$\Delta\tau$	normalized time step (−)
Δt	time step (s)
Δx	cell size (m)
κ	interface curvature (m^{-1})
λ	slip length (m)
τ	normalized time (−)
τ_{CI}	normalized capillary-inertial time (−)
μ	dynamic viscosity ($kg \cdot m^{-1} \cdot s^{-1}$)
ρ	density ($kg \cdot m^{-3}$)
σ	surface tension ($kg \cdot s^{-2}$)
θ_{adv}	advancing contact angle (°)
θ_{rec}	receding contact angle (°)

Abbreviations

CFL	Courant number
CICSAM	compressive interface capturing scheme for arbitrary meshes
CSF	continuum surface force
SIMPLEC	semi-implicit method for pressure linked equations-consistent
VOF	volume of fluid

AUTHOR CONTRIBUTIONS

Konstantinos Konstantinidis: Conceptualization; data curation; formal analysis; investigation; methodology; software; validation; writing – original draft; writing – review and editing. **Johan Göhl:** Formal analysis; methodology; software; supervision; writing – review and editing. **Andreas Mark:** Formal analysis; methodology;

software; supervision; writing – review and editing. **Srdjan Sasic:** Conceptualization; formal analysis; funding acquisition; investigation; methodology; project administration; supervision; validation; writing – review and editing.

ACKNOWLEDGEMENTS

This work has been financed by the Swedish Research Council (Vetenskapsrådet, Dnr 2019-04969). The authors would like to acknowledge that the computations and handling of data were enabled by resources provided by the Swedish National Infrastructure for Computing (SNIC), partially funded by the Swedish Research Council through grant agreement no. 2018-05973.

CONFLICT OF INTEREST

The authors declare that there is no conflict of interests from this work.

DATA AVAILABILITY STATEMENT

The data of this study are available upon request from the corresponding author.

ORCID

Konstantinos Konstantinidis https://orcid.org/0000-0002-4214-6337

REFERENCES

[1] J. B. Boreyko, C. H. Chen, *Phys. Rev. Lett.* **2009**, *103*, 2.
[2] R. Enright, N. Miljkovic, J. Sprittles, K. Nolan, R. Mitchell, E. N. Wang, *ACS Nano* **2014**, *8*, 10352.
[3] S. A. Kulinich, M. Farzaneh, *Langmuir* **2009**, *25*, 8854.
[4] H. Wang, L. Tang, X. Wu, W. Dai, Y. Qiu, *Appl. Surf. Sci.* **2007**, *253*, 8818.
[5] L. B. Boinovich, A. M. Emelyanenko, *Mendeleev Commun.* **2013**, *23*, 3.
[6] S. Farhadi, M. Farzaneh, S. A. Kulinich, *Appl. Surf. Sci.* **2011**, *257*, 6264.
[7] N. Miljkovic, R. Enright, E. N. Wang, *J. Heat Transfer* **2013**, *135*, 111004.
[8] N. Miljkovic, R. Enright, Y. Nam, K. Lopez, N. Dou, J. Sack, E. N. Wang, *Nano Lett.* **2013**, *13*, 179.
[9] K. M. Wisdom, J. A. Watson, X. Qu, F. Liu, G. S. Watson, C.-H. Chen, *Proc. Natl. Acad. Sci. U. S. A.* **2013**, *110*, 7992.
[10] D. Maggiolo, M. Seemann, H. Thunman, O. Santos, A. Larsson, S. Sasic, H. Ström, *AIChE J.* **2019**, *65*, 317.
[11] S. P. Dalawai, M. A. Saad Aly, S. S. Latthe, R. Xing, R. S. Sutar, S. Nagappan, C. S. Ha, K. Kumar Sadasivuni, S. Liu, *Prog. Org. Coat.* **2020**, *138*, 105381.
[12] C. Yu, S. Sasic, K. Liu, S. Salameh, R. H. Ras, J. R. van Ommen, *Chem. Eng. Res. Des.* **2020**, *155*, 48.
[13] Q. Wang, X. Yao, H. Liu, D. Quéré, L. Jiang, *Proc. Natl. Acad. Sci. U. S. A.* **2015**, *112*, 9247.
[14] C. Lv, P. Hao, Z. Yao, Y. Song, X. Zhang, F. He, *Appl. Phys. Lett.* **2013**, *103*, 1.
[15] G. S. Watson, M. Gellender, J. A. Watson, *Biofouling* **2014**, *30*, 427.
[16] S. Nishimoto, B. Bhushan, *RSC Adv.* **2013**, *3*, 671.
[17] X. Yan, L. Zhang, S. Sett, L. Feng, C. Zhao, Z. Huang, H. Vahabi, A. K. Kota, F. Chen, N. Miljkovic, *ACS Nano* **2019**, *13*, 1309.
[18] C. Lv, P. Hao, X. Zhang, F. He, *ACS Nano* **2015**, *9*, 12311.
[19] C. Lv, P. Hao, Z. Yao, F. Niu, *Langmuir* **2015**, *31*, 2414.
[20] X. Chen, R. S. Patel, J. A. Weibel, S. V. Garimella, *Sci. Rep.* **2016**, *6*, 18649.
[21] D. Quéré, *Annu. Rev. Mater. Res.* **2008**, *38*, 71.
[22] E. B. Dussan, *Annu. Rev. Fluid Mech.* **1979**, *11*, 371.
[23] P. G. de Gennes, *Rev. Mod. Phys.* **1985**, *57*, 827.
[24] D. Legendre, M. Maglio, *Comput. Fluids* **2015**, *113*, 2.
[25] J. H. Snoeijer, B. Andreotti, *Annu. Rev. Fluid Mech.* **2013**, *45*, 269.
[26] K. Wang, Q. Liang, R. Jiang, Y. Zheng, Z. Lan, X. Ma, *Langmuir* **2017**, *33*, 6258.
[27] Y. Wang, P. Ming, *Phys. Fluids* **2019**, *31*, 122108.
[28] F. Liu, G. Ghigliotti, J. J. Feng, C. H. Chen, *J. Fluid Mech.* **2014**, *752*, 39.
[29] Y. Cheng, J. Xu, Y. Sui, *Int. J. Heat Mass Transfer* **2016**, *95*, 506.
[30] Y. Nam, H. Kim, S. Shin, *Appl. Phys. Lett.* **2013**, *103*, 161601.
[31] Y. Chen, Y. Lian, *Phys. Fluids* **2018**, *30*, 112102.
[32] X. Chen, J. Lu, G. Tryggvason, *Phys. Fluids* **2019**, *31*, 052107.
[33] F. Chu, X. Wu, B. Zhu, X. Zhang, *Appl. Phys. Lett.* **2016**, *108*, 194103.
[34] F. Chu, Z. Yuan, X. Zhang, X. Wu, *Int. J. Heat Mass Transfer* **2018**, *121*, 315.
[35] H. Vahabi, W. Wang, J. M. Mabry, A. K. Kota, *Sci. Adv.* **2018**, *4*, eaau3488.
[36] Z. Yuan, R. Wu, X. Wu, *Int. J. Heat Mass Transfer* **2019**, *135*, 345.
[37] J. Wasserfall, P. Figueiredo, R. Kneer, W. Rohlfs, P. Pischke, *Physical Review Fluids* **2017**, *2*, 1.
[38] R. Attarzadeh, A. Dolatabadi, *Phys. Fluids* **2017**, *29*, 012104.
[39] Y. Shi, G. H. Tang, H. H. Xia, *Int. J. Heat Mass Transfer* **2015**, *88*, 445.
[40] X. Liu, P. Cheng, *Int. Commun. Heat Mass Transfer* **2015**, *64*, 7.
[41] Z. Liang, P. Keblinski, *Appl. Phys. Lett.* **2015**, *107*, 143105.
[42] S. Gao, Q. Liao, W. Liu, Z. Liu, *J. Phys. Chem. C* **2018**, *122*, 20521.
[43] F. F. Xie, G. Lu, X. D. Wang, D. Q. Wang, *Langmuir* **2018**, *34*, 11195.
[44] R. Wen, S. Xu, D. Zhao, Y. C. Lee, X. Ma, R. Yang, *ACS Appl. Mater. Interfaces* **2017**, *9*, 44911.
[45] H. Cha, C. Xu, J. Sotelo, J. M. Chun, Y. Yokoyama, R. Enright, N. Miljkovic, *Physical Review Fluids* **2016**, *1*, 064102.
[46] M. D. Mulroe, B. R. Srijanto, S. F. Ahmadi, C. P. Collier, J. B. Boreyko, *ACS Nano* **2017**, *11*, 8499.
[47] T. Mouterde, T. V. Nguyen, H. Takahashi, C. Clanet, I. Shimoyama, D. Quéré, *Physical Review Fluids* **2017**, *2*, 1.
[48] R. Enright, N. Miljkovic, N. Dou, Y. Nam, E. N. Wang, *J. Heat Transfer* **2013**, *135*, 091304.
[49] T. Mouterde, G. Lehoucq, S. Xavier, A. Checco, C. T. Black, A. Rahman, T. Midavaine, C. Clanet, D. Quéré, *Nat. Mater.* **2017**, *16*, 658.

[50] P. Lecointre, T. Mouterde, A. Checco, C. T. Black, A. Rahman, C. Clanet, D. Quéré, *Physical Review Fluids* **2019**, *4*, 24.
[51] X. Liu, P. Cheng, X. Quan, *Int. J. Heat Mass Transfer* **2014**, *73*, 195.
[52] S. Farokhirad, J. F. Morris, T. Lee, *Phys. Fluids* **2015**, *27*, 102102.
[53] A. Mark, R. Rundqvist, F. Edelvik, *Fluid Dynamics and Materials Processing* **2011**, *7*, 241.
[54] J. U. Brackbill, D. B. Kothe, C. Zemach, *J. Comput. Phys.* **1992**, *100*, 335.
[55] J. Göhl, A. Mark, S. Sasic, F. Edelvik, *Int. J. Multiphase Flow* **2018**, *109*, 164.
[56] J. P. Van Doormaal, G. D. Raithby, *Numerical heat transfer* **1984**, *7*, 147.
[57] M. M. Francois, S. J. Cummins, E. D. Dendy, D. B. Kothe, J. M. Sicilian, M. W. Williams, *J. Comput. Phys.* **2006**, *213*, 141.
[58] P. Bartholomew, F. Denner, M. H. Abdol-Azis, A. Marquis, B. G. van Wachem, *J. Comput. Phys.* **2018**, *375*, 177.
[59] C. M. Rhie, W. L. Chow, *AIAA J.* **1983**, *21*, 1525.
[60] A. Mark, B. G. van Wachem, *J. Comput. Phys.* **2008**, *227*, 6660.
[61] S. Afkhami, S. Zaleski, M. Bussmann, *J. Comput. Phys.* **2009**, *228*, 5370.
[62] K. Wang, Q. Liang, R. Jiang, Y. Zheng, Z. Lan, X. Ma, *RSC Adv.* **2016**, *6*, 99314.
[63] Q. Peng, X. Yan, J. Li, L. Li, H. Cha, Y. Ding, C. Dang, L. Jia, N. Miljkovic, *Langmuir* **2020**, *36*, 9510.
[64] D. Lu, M. Zhao, H. Zhang, Y. Yang, Y. Zheng, *Langmuir* **2020**, *36*, 5444.

How to cite this article: K. Konstantinidis, J. Göhl, A. Mark, S. Sasic, *Can. J. Chem. Eng.* **2022**, *100*(12), 3517. https://doi.org/10.1002/cjce.24591

Paper B

Coalescence-induced jumping of droplets from superhydrophobic surfaces — The effect of contact-angle hysteresis

K. Konstantinidis, J. Göhl, A. Mark, and S. Sasic. Coalescence-induced jumping of droplets from superhydrophobic surfaces — The effect of contact-angle hysteresis. ***Physics of Fluids*** **34.11 (Nov. 2022), 113302. DOI:** 10.1063/5.0118645

Coalescence-induced jumping of droplets from superhydrophobic surfaces — the effect of contact-angle hysteresis

K. Konstantinidis*,[1] J. Göhl,[2] A. Mark,[2] and S. Sasic[1]
[1)] *Division of Fluid Dynamics, Department of Mechanics and Maritime Sciences, Gothenburg, SE-412 96, Sweden*
[2)] *Fraunhofer–Chalmers Center, Chalmers Science Park, Gothenburg, SE-412 88, Sweden*

(*Electronic mail: konkonst@chalmers.se)

(Dated: 5 October 2022)

Droplets coalesce and jump from superhydrophobic surfaces, a result that stems from the dominance of capillary and inertial forces and the presence of high contact angles. This phenomenon has been a subject of intensive numerical research mostly for cases when the degree of hydrophobicity is described by a single contact-angle value (a static contact angle). The introduction of various degrees of contact-angle hysteresis complicates the numerical modeling of the jumping process due to the sensitivity of the results to the effective value of the contact angle. We have developed and validated a comprehensive volume-of-fluid(VOF)–immersed boundary numerical framework that accounts for the effect of hysteresis by focusing on the representation of actual (i.e. effective) values of contact angles. By comparing the behavior of jumping droplets on superhydrophobic surfaces with several degrees of hysteresis (up to 15°), we quantified the influence of hysteresis on the jumping process and identified various stages of the merged droplet's detachment and re-attachment to the surface. The latter phenomena were observed in all our simulations with droplets of different initial radii. In all the cases with hysteresis, the merged droplet eventually jumps, but we point out the decrease in the jumping velocity as compared to cases with only a static contact angle imposed. Finally, by using the Kistler dynamic contact-angle model, we demonstrate and quantify the importance of accurately capturing the dynamic receding contact angle when droplets jump from superhydrophobic surfaces with various degrees of hysteresis.

I. INTRODUCTION

The main feature of hydrophobic surfaces is that they inherently resist the contact between a liquid and a solid surface, resulting in a liquid-repellent behavior. The contact angle created at the junction of the three phases, liquid, gas and solid, is required to be above 150° in order for a surface to be classified as superhydrophobic[1]. Minimization of a liquid–solid contact area has been considered beneficial for numerous applications involving heat-transfer with drop-wise condensation[2,3], anti-icing or defrosting coatings[4–7], water-repellent technology[8], and self-cleaning surfaces[9–13]. Studies also suggest that avoiding hysteresis, defined as the difference between advancing, θ_{adv}, and receding, θ_{rec}, contact angles, further promotes the use of superhydrophobic surfaces[14,15] in the mentioned applications. However, in practice, the presence of various types of heterogeneities, due to surface roughness and/or wettability discontinuities, can cause deviation from low hysteresis[16–18]. Superhydrophobic surfaces are known for the existence of roughness patterns and heterogeneities caused by hierarchical microstructures (pillars) or anisotropic textures[1,19]. In technological applications, such surfaces are often inspired by natural water-repellent and self-cleaning superhydrophobic surfaces[13].

Hysteresis is caused by the pinning of the contact line (an intersecting line for liquid, solid and gas phases) due to defects existing on the surface[20]. The two characteristic angles (advanced and receding ones) are often measured as the limits between which an externally driven droplet remains pinned on the surface[16]. When the contact line starts moving, the dynamics of the Moving Contact Line (MCL) dictate the behavior of the interface and an apparent contact angle, θ_{app}, can be identified at macroscopic scales. The latter angle can exceed the values of θ_{adv} and θ_{rec}. Understood from the physical phenomena at microscopic scales, but with a hydrodynamic description still valid, a dynamic contact-angle model is often formulated[21,22]. A notable characteristics of hysteresis is the pinning force which is defined as the additional force required to remove a droplet from the surface, before the contact area starts retracting. The force is computed as $F_{pinning} = 2\sigma R(\cos\theta_{adv} - \cos\theta_{rec})$, where σ is the surface tension of the liquid–gas interface and $2R$ is the droplet diameter given as a reference length.[20]

Self-removing droplets from superhydrophobic surfaces have recently gained attention, since the driving physics of the process is capillarity, a free-energy source. More specifically, when two or more droplets coalesce, they tend to minimize their surface energy, which connects to the minimization of the interface area. The existence of a superhydrophobic surface and its forced interaction with the merged droplet result in redirecting upwards the kinetic energy generated during coalescence and cause the eventual jumping of the droplet[23]. This phenomenon has been used for improving performances of various technological applications, such as those involving condensation and self-cleaning of surfaces[9,24]. Numerous experimental and numerical studies have focused on understanding the fundamental mechanisms behind the droplet jumping process. The existence of low adhesion and high contact angles, together with the negligible gravity force for scales smaller than the capillary length, promote a swift detachment from the surface, reducing the contact area during the jumping process.[25,26] In addition, studies identify distinguished stages of the process, which are the liquid bridge creation and expansion, its interaction with the superhydrophobic surface, the oscillating shapes of the merged droplet resulting

from coalescence, and the eventual jumping[27,28]. Boreyko and Chen[23] were the first to observe that condensing droplets can be removed from a surface after coalescing and argued that this phenomenon could significantly improve condensation. The same study provided information on the jumping velocities following a capillary-inertial scaling for droplets of different sizes and presented a cut-off radius for which the droplets in the lower radius region deviate from it. Liu et al.[27,29] compared experimental findings of droplets jumping from Leidenfrost surfaces with numerical simulations of droplets jumping on superhydrophobic surfaces. The authors portrayed with this comparison the existence of the already mentioned distinguished stages of the jumping process. Studies on dropwise condensation showed the effect of microstructures on the early release of droplets, which improved the heat transfer[24,30–32].

A previous study pointed out that the jumping velocity was reaching up to 0.21 v_{CI}, where v_{CI} is the characteristic velocity associated with the capillary-inertial regime[24]. At this velocity, energy efficiency in converting the available surface energy to an upwards motion would correspond to 6%, but there are published works that suggest improvements in the efficiency of up to 8 times in the case of structures located between the coalescing point and the surface[33–36]. However, most studies suggest a certain range of jumping velocities ($v^*_{jump} = 0.2 - 0.25\ v_{\mathrm{CI}}$)[24,26,37,38] and energy conversion rates (from 3% up to 6%). Yan et al.[39] performed a systematic study of the differences in jumping resulting from different surface structures, wettabilities and relative sizes of droplets. Their findings suggested a maximum jumping velocity of 0.26 v_{CI} for two droplets coalescing on a superhydrophobic surface with nanoblade structures. For surfaces with microscale textures or wettability changes, the same authors identified variations in the jumping direction, and the jumping velocity reported was generally scattered from the capillary-inertial scaling and reduced for the biphilic surface.

Jumping of droplets on superhydrophobic surfaces has also been investigated numerically. From the realm of continuum-based techniques that focus on capturing or tracking the interface, volume-of-fluid (VOF) was mostly selected[34,43,44,46,48–52] even though several other methods were also used[45,53–55]. In addition, there are studies using either a lattice Boltzmann framework[40,41,56–58] or Molecular Dynamics[59–61] with results that in principle showed the same trends and observations as did the experiments and continuum-based simulations. This matching of findings is related to the overall characteristics of the jumping process, but also to the relevance of the proposed capillary-inertial scaling law[23]. A comparative list for the jumping velocities , that are obtained upon detachment and range in the main body of the capillary-inertial region, given by both numerical and experimental studies, is presented in Table I. The given values are normalized by $v_{\mathrm{CI}} = \sqrt{\sigma/(R_i\rho)}$.

There has been a relatively limited number of numerical works that varied the value of the contact angle (often referred to as the static or the equilibrium contact angle) and consequently displayed a different velocity behavior for the droplets during jumping[44]. This variation in the results demonstrates the sensitivity of the problem and stresses the importance of accurately modeling the dynamics of the Moving Contact Line (MCL). The fact that the eventual jumping velocity is sensitive to the value of the contact angle, suggests that the presence of hysteresis will indeed influence the entire droplet jumping process and therefore necessitates that a trustworthy contact–angle representation is considered during implementation of boundaries. Cheng et al.[54] looked at this phenomenon and noted that, by varying the contact angle and assuming constant values for θ_{adv} and θ_{rec}, the process of jumping was mostly influenced by the value of the receding contact angle. We also note that the velocity results of a no-hysteresis configuration reported in that study show differences as compared with the majority of the published numerical results related to the evolution of the jumping velocity. More specifically, the expected stages of the jumping process were not clearly observed in the results. Another work by Chen et al.[45] used the generalized slip boundary condition to connect the contact line velocity with a dynamic contact angle, but the effect of hysteresis was investigated by varying a slip parameter while not showing how the model compared to a no hysteresis case. Nam et al.[62] compared the jumping behavior of a hydrophobic and a superhydrophobic surface with dynamic contact angles in order to identify dissipation of the MCL due to hysteresis-induced pinning and viscosity. In an experimental study, Cha et al.[63] performed experiments with superhydrophobic surfaces of different textures and with variable contact angles and degrees of hysteresis. The authors identified different minimum droplet sizes for the jumping to take place and pointed to pinning and no-jumping observations as the outcomes of an increased droplet–surface adhesion in the cases with a more pronounced hysteresis. A noble guess for the adhesion effect, which has also been mentioned previously[62], would be that a higher degree of hysteresis permits lower receding angles to occur when the droplet retracts from the surface. The adhesion force to the surface should also reduce the efficiency of the jumping process[63]. Experiments have not yet reported the actual values that the apparent contact angle obtains during the stages of droplet coalescence and jumping on superhydrophobic surfaces. This statement represents a limitation when promoting the use of a certain tested dynamic contact angle model. Instead, those values are often provided from experimental studies as the θ_{adv} and θ_{rec} from initial arrangements of droplets before initiation of the contact line movement. Finally, another study by Attarzadeh and Dolatabadi[43], which investigated numerically the effect of microstuctures on superhydrophobic surfaces, mentions the use of θ_{adv} and θ_{rec} as upper and lower limits of their contact-angle implementation. For a flat surface without such structures, the $\Delta\theta$ was selected to be around 3°. For the heterogeneous surface with rectangular pillars, the same authors used the Kistler dynamic contact-angle model with a static contact angle as input. However, there were no investigations for scenarios with higher degrees of hysteresis.

Our interest in this work is mainly inspired by the possibilities of tuning and improving superhydrophobic surfaces through simulations that are capable of predicting the effective (i.e.truly acting) values of contact angles. We note that such an analysis is possible even when surfaces are modeled

TABLE I: List of the reported numerical and experimental jumping velocities of merged droplets on superhydrophobic surfaces.

Numerical										
Authors	Liu et al.[27]	Farokhirad et al.[40]	Liu et al.[41]	Khatir et al.[38]	Wang et al.[42]	Attarzadeh and Dolatabadi[43]	Wasserfall et al.[44]	Vahabi et al.[34]	Chen et al.[45]	Li et al.[46]
Normalized jumping vel.[-]	0.20	0.20	0.18	0.18 – 0.20	0.18 – 0.23	0.20	∼ 0.25	0.20	0.22	0.22

Experimental								
Authors	Boreyko and Chen[23]	Liu et al.[28]	Enright et al.[24]	Kim et al.[37]	Khatir et al.[38]	Mouterde et al.[47]	Wang et al.[26]	Yan et al.[39]
Normalized jumping vel.[-]	0.19	0.21	∼ 0.21	0.23	0.16 – 0.19	0.17 – 0.25	∼ 0.20 – 0.24	0.26

as flat surfaces, i.e. when heterogeneities are not explicitly a part of the computational domain. For that purpose, it is only important that the simulations are able to correctly model the physics of a droplet–surface interaction and predict scenarios when dynamic contact angles are affecting the jumping process. The acquired knowledge can be used to tailor superhydrophobic surfaces to, for example, facilitate and promote jumping for specific droplet sizes that are considered advantageous for certain applications and that would not jump on every superhydrophobic surface[32,63,64]. Additionally, we can use the suggested numerical framework to identify the exact tuning characteristics that would help to minimize the adhesion force. This would increase the energy conversion rate of the merged droplet's upwards motion. Numerous applications will also benefit from monitoring and controlling the effect of hysteresis since the observed contact angles on newly designed superhydrophobic surfaces are related to the potential overall efficiency of the jumping process with a framework that handles the contact-angle hysteresis by paying special attention to fine details of the Moving Contact Line (MCL) dynamics. However, we point out the absence of credible proof that a certain dynamic contact-angle model would in general behave more accurately than any of the ones typically presented in literature, without limiting our discussion to just the implementations relevant for our work. Additionally, we argue that the representation and implementation of the actual contact angles become more challenging but also more important, because the outcome of the whole process is highly sensitive (as we will show in what follows) to the droplets' interaction with the surface. For making possible optimization of the properties of a superhydrophobic surface through numerical simulations and in order to achieve a high degree of accuracy when predicting the dynamics of the MCL, special treatment is required in the numerical framework to deal with the existence of the stress singularity at the MCL[65–67]. For that purpose, we use in this work the frequently suggested Navier slip boundary condition[68,69] and implement it in the way as described in Section II.

Although a specific behavior of jumping droplets on surfaces with hysteresis has already been observed experimentally, there is still a lack of numerical analyses that focus on the details of the droplet–surface interaction and the contact line movement in such cases. Moreover, there is still a limited number of studies that provide detailed explanation and quantification of the changes in the jumping behavior that the presence of hysteresis may cause. The present work is an attempt to fill that gap and, for that purpose, we use the in-house multiphase flow solver IPS IBOFlow®. The solver is based on a comprehensive combined VOF–immersed boundary framework and includes several dynamic contact-angle models and a Navier slip model, as presented and validated by Göhl et al.[70]. To understand the behavior of jumping droplets on superhydrophobic surfaces with a significant hysteresis present, realistic values for θ_{adv} and θ_{rec} from selected experimental works are used and variations in the degree of hysteresis are performed to identify limitation points. For the contact-angle implementation, our idea has been to increase gradually the complexity with which hysteresis is both introduced and modeled on the studied superhydrophobic surfaces. We thus start with an implementation of fixed advancing and receding contact–angle values using the quasi-static scheme, and continue with an example of a selected dynamic contact-angle model. In summary, we aim at identifying, understanding and quantifying a range of behaviors for jumping droplets when different degrees of hysteresis are present. For that purpose, we carry out a systematic numerical investigation on how the presence of hysteresis affects the jumping process by looking at the detailed physics of the contact angles and the MCL, and the influence of the radii of the involved droplets.

II. METHODOLOGY AND CONFIGURATION

A. Methods

The numerical computations were performed with the in-house flow solver IPS IBOFlow® that is based on a combined volume-of-fluid (VOF)–immersed boundary method[71]. It solves the incompressible Navier–Stokes equations:

$$\nabla \cdot \mathbf{v} = 0\,,$$
$$\frac{\partial(\rho\mathbf{v})}{\partial t} + \mathbf{v}\cdot\nabla(\rho\mathbf{v}) = -\nabla p + \nabla\cdot(\mu\nabla\mathbf{v}) + \rho\,\mathbf{g} + \mathbf{f}_{SF}\,, \quad (1)$$

where $\mathbf{v}$ gives the velocity vector field, P the pressure, ρ and μ is the density and dynamic viscosity of the fluid, $\mathbf{g}$ is the

gravitational acceleration and $\mathbf{f}_{SF}$ is the surface tension force at the interface.

VOF is a sharp interface-capturing method and includes a transport equation for the volume fraction field to capture the interface location, which reads:

$$\frac{\partial \alpha}{\partial t} + \mathbf{v} \cdot \nabla \alpha = 0, \tag{2}$$

where α is the volume fraction. Additionally, to obtain the fluid properties for a volume cell, density and viscosity are computed by the volume average of the properties for the two fluids as following:

$$\rho = \alpha \rho_1 + (1-\alpha)\rho_2, \tag{3}$$
$$\mu = \alpha \mu_1 + (1-\alpha)\mu_2. \tag{4}$$

The coupling of pressure and velocity is performed with the help of the segregated SIMPLEC method[72] and the discretization is performed on a co-located grid. For the volume fraction equation, Equation (2), discretization of the advective part is performed according to the higher order differencing scheme CICSAM[73]. It is a fully conservative and bounded scheme that ensures sharpness of the interface during its advection.

The continuum surface force method (CSF)[74] is used for the surface tension body force $\mathbf{f}_{SF}$, where the force is given from the interface geometry and the surface tension property as

$$\mathbf{f}_{SF} = \sigma \kappa \mathbf{n}, \tag{5}$$

where σ is the surface tension between liquid and gas, κ is the interface curvature and $\mathbf{n}$ the interface normal vector.

The unit normal vector $\hat{\mathbf{n}}$ for the interface is computed from the gradient of the volume fraction, whereas the curvature is obtained from the divergence of $\hat{\mathbf{n}}$:

$$\hat{\mathbf{n}} = \frac{\mathbf{n}}{\|\mathbf{n}\|} = \frac{\nabla \alpha}{\|\nabla \alpha\|}, \tag{6}$$

and then the curvature is calculated as

$$\kappa = -\nabla \cdot \hat{\mathbf{n}}. \tag{7}$$

To capture the location of the Moving Contact Line and model the angle of the interface, the following approach is used: for numerical implementation of the contact angle we follow our previous work.[70]. For the implementation of hysteresis with different advancing and receding contact angles, the quasi-static model is used that imposes the apparent contact angle by recognizing a receding or advancing movement in accordance to the computed contact line velocity. In addition, we use the Kistler dynamic contact–angle model and the value of the imposed dynamic contact angle θ_{dyn} in the cells near the solid surface and in proximity to the location of the contact line is given as follows: it is known that the Kistler's law, as it is also known, applies the Hoffman function f_{Hoff}[75,76], which is a correlation to experimental data, when the contact line velocity is to be calculated. When using the Kistler model, the value of the contact angle for a static arrangement is required, which is the same as the quasi-static θ_{adv} and θ_{rec} values for the corresponding contact line movement. In this study, we thus adopt that the angle for a stationary contact line in the Kistler model is given by the advancing or receding contact angles, as they are available from experimental studies. Then a modification of the Hoffman function was performed following a study on both advancing and receding contact angles, which demonstrated that, for surfaces with very high contact angles[77], the Kistler model is still able to capture the behavior of the reported experimental data[76]. The equation reads

$$\theta_{dyn} = f_{Hoff}\left(Ca + f_{Hoff}^{-1}(\theta_{st})\right), \tag{8}$$

where $f_{Hoff}(x) =$

$$\cos^{-1}\left(1 - 2\tanh\left[5.16\left(\frac{x}{1+0.332x^{0.99}}\right)^{0.62}\right]\right). \tag{9}$$

As all solution variables are stored at the cell centers, a Balanced-Force method[78,79] is used to improve the accuracy of the properties calculated at the faces. This method includes the forces and a time derivative in the velocity interpolation, making the forces and the pressure gradients balanced at cell faces. The result is a more accurate and stable estimation for the face velocities, reducing the spurious currents and oscillations due to pressure instabilities.

Boundary conditions are formulated using the mirroring immersed boundary method (MIBM)[71,80] that makes it possible to describe solid surfaces with triangulated objects. MIBM is a second-order accurate method that sets the velocity field at the boundary by mirroring the velocity field. The method is used to set the local boundary condition on the structured octree-background grid. For the contact line, the method simplifies the surface force calculations when considering the local boundary normal vector needed when implementing a contact-angle model[70].

For the velocity at the three-phase boundary, a slip effect is assumed and modeled with the Navier slip boundary condition to remove the MCL stress singularity problem. Following the implementation of the immersed boundary method in our previous publications[70,81], the slip velocity is computed in the tangential direction and imposed by the immersed boundary condition in the equation of MIBM that reads

$$\frac{\vec{v}_{ext} + \vec{v}_{ghost}}{2} = \vec{v}_{IB,slip}, \tag{10}$$

where $\vec{v}_{IB,slip}$ is the computed velocity to be set at the boundary for which the tangential slip velocity v_{slip} has been added, $\vec{v}_{ext}$ is the velocity at the nodes of the fluid and $\vec{v}_{ghost}$ is the velocity at the fictitious nodes of the domain that are occupied by the body mass.

B. Configuration of the simulations

We design our simulations in three Cartesian dimensions with a flat plane representing the superhydrophobic surface

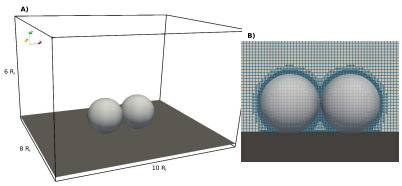

FIG. 1: Representation of A) the physical model used in our work and B) the grid set-up and refinement for a case for which the minimum cell size is 1/40 of R_i. (40 cells per R_i

for which the boundary conditions are imposed. The framework has the ability to vary the number of droplets and their sizes. In addition, it connects the grid creation and the domain dimensions to the radius of the smallest droplet. The size of the domain is $10R_i \times 8R_i \times 6R_i$, scaling to the smallest droplet initial radius R_i, as represented in Figure 1A).

The grid is automatically created with an octree grid that uses Adaptive Grid Refinement (AGR). The method is setting a selected level of refinement to the interface between the fluids, as well as to the liquid-solid boundary. The AGR method monitors the interface at every time step and, depending on movements of the interface, updates the grid if needed. It sets at least 6 cells of the highest refinement level stretching away from the interface (see also Figure 1B). These cells are selected to have a size proportional to R_i. For example, when a certain grid is said to have 20 cells per R_i (c_R), where $\Delta x = R_i/c_R$, this expression implies that the cells near the interface have a cell size corresponding to 1/20 of the droplet radius. The same principle of course holds for other grid resolutions.

The choice of a time step in a problem with a high influence of capillary and inertial forces needs to take into account the dominating time scales for the jumping droplets phenomenon. The time is given as the normalized time τ which is scaled by the capillary-inertial time scale t_{CI} and hence the time step Δt should be smaller than $t_{CI} = \sqrt{R_i^3 \rho/\sigma}$. In addition, the time step needs to respect the time-step constraint related to capillary waves:

$$\Delta t \leq \sqrt{\frac{(\rho_1+\rho_2)\Delta x^3}{4\pi\sigma}}, \tag{11}$$

as derived by Brackebill et al.[74] or the equivalent one suggested by Denner and van Wachem[82] for a static case of oppositely coming waves:

$$\Delta t \leq \sqrt{\frac{(\rho_1+\rho_2)\Delta x^3}{2\pi\sigma}}. \tag{12}$$

Additionally, the time step choice must comply with the Courant number (CFL) condition. For different droplet radii, the average normalized jumping velocity is considered constant $v^*_{jump} = U$, as has been shown by several previous

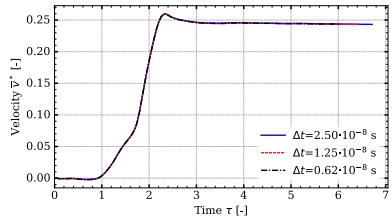

FIG. 2: Time convergence study of the average upwards velocity in time, normalized by the capillary-inertial scales. The radius of the initial droplets is 25 m.

works[27,40]. The velocity in the capillary-inertial regime scales with $v_{CI} = \sqrt{\sigma/(R_i\rho)}$. So the actual average jumping velocity should be $v_{jump} = U\, v_{CI}$. When a default case is set up for the system with Δt_{def} being the time step and $\Delta x_{def} = R_{i,def}/c_{R,def}$, we have the Courant number computed as

$$\mathrm{CFL}_{def} = \mathrm{CFL}_{const} = \frac{v_{jump}\Delta t_{def}}{\Delta x_{def}}. \tag{13}$$

To reach a constant CFL when the radii of the initial droplet or the cell size vary, the time step needs to be adjusted so as

$$\Delta t = \mathrm{CFL}_{const}\frac{\Delta x}{v_{jump}}. \tag{14}$$

By substituting in Equation (14) the definitions for v_{jump} and Δx_{def}, the time step of a simulation with different R_i or grid resolution should follow:

$$\Delta t = \Delta t_{def}\left(\frac{R_i}{R_{i,def}}\right)^{\frac{3}{2}}\frac{c_{R,def}}{c_R}. \tag{15}$$

III. VALIDATION

We demonstrate time convergence of our framework by following the jumping of two equally-sized droplets of $R_i = 25$ m and using three time steps for the simulations, $\Delta t = 2.5$E-8 s, 1.25E-8 s and 0.625E-8 s, that correspond to maximum CFL values of approximately 0.55, 0.30 and 0.15, respectively. Figure 2 shows the evolution of the velocity profile with time τ and velocity v^* normalized by the corresponding scales t_{CI} and v_{CI}, respectively. The lines show an identical velocity evolution for the different time steps, as no observable difference between them is identified. That would in theory permit us to use the largest time step of the three cases for all our simulations. However, due to an excess increase in the number of inner iterations for reaching the same solution residual, doubling the time step is not accompanied by halving the computational cost and, as a result, the medium time step of $\Delta t = 1.25$E-8 s was selected for use throughout this

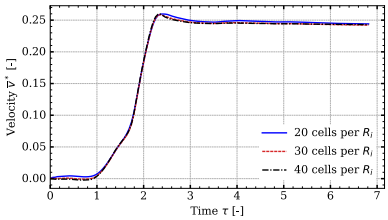

FIG. 3: Grid convergence study of the average upwards velocity in time, normalized by the capillary-inertial scales, for three different grid configurations for $R_i = 25$ m. The cases involving 30 and 40 cells per R_i demonstrate convergence of the jumping velocity behavior.

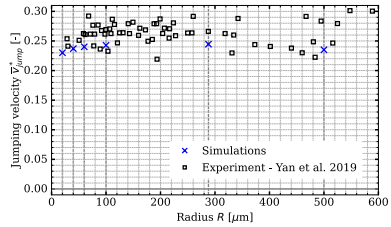

FIG. 4: Obtained jumping velocities from the simulations with different droplet radii R_i as compared to experimental data by Yan et al.[39]. Both sets of values are normalized with the corresponding velocity capillary-inertial scale v_{CI}.

work. Moreover, the selected time step case returned values for the Courant number that do not exceed 0.5 for all the simulations performed in this study. Restricting CFL preserves a sharper estimation of the interface from the CICSAM method, which will retain the same approach for computing convective coefficients in the volume fraction transport equation.

To achieve and prove grid convergence, it is needed to understand the behavior of the slip length l_{sl} that is used in the formulation of the Navier slip boundary condition. A series of tests were performed to identify the sensitivity of the simulations to the grid resolution. Studies show that in several applications the slip length is highly dependent on the cell size of the cells in the vicinity of the solid surface[83,84]. For the jumping droplets case, the slip length can be also associated with the radius or another characteristic length of the system, e.g. the height of superhydrophobic microstructures. Therefore, we tested two methodologies to identify how grid convergence and the outcome of the jumping process are affected by the choice of a slip length. By varying the cell size, we observed that in the cases when the slip length was adjusted to a half of the cell size, grid convergence was partly achieved but with a distinct separation between the jumping droplet velocities. Second, when the slip length was kept constant in relation to the droplet radius, convergence was achieved consistently in the jumping velocities with a better agreement of the final result. The general behavior of the system was similar for all the simulations, but to our understanding, the slip length is an important parameter to identify the instant when the droplet is released from the solid surface.

We present the results from the simulations with 20, 30 and 40 cells per R_i, with a slip length of $l_{sl} = 310$ nm and $R_i = 25$ m. In Figure 3 the cases of 30 and 40 cells per R_i show convergence, while the case of 20 cells per R_i does not yield the same result. For the remaining simulations in this paper, the resolution of 40 cells per R_i is selected. The proposed grid configuration is benefiting from the use of two levels of refinement close to the interface. To keep an acceptable size of the cells in the regions that exclude the interface and the Moving Contact Line (termed base cells), only a single level of refinement is suggested for use in a coarser grid. For the case of 30 cells per R_i, the base cells in the far domain are smaller than for the 40 cells per R_i case, increasing the computational cost in the less significant regions of the domain in the far-field of the interface.

We also compared the results of our simulations to experimental results of the jumping velocity. In Figure 4 data from Yan et al.[39] are presented for the jumping velocity measured upon detachment, normalized by the capillary-inertial velocity scale v_{CI} for different initial droplet radii R_i. The mentioned study provides consistent measurements of the jumping velocity that follows the capillary-inertial scaling. The simulations were performed using advancing and receding contact angles $\theta_{adv} = 170.3^\circ$ and $\theta_{rec} = 167.7^\circ$ that correspond to the measured values of the homogeneous superhydrophobic surface in the experiment. A good agreement of the jumping velocities is noticed, with the numerical results overall capturing the behavior observed in the experiment. The trend of the normalized jumping velocity to remain constant over R_i for the capillary-inertial scaling is clearly demonstrated in our simulations. The estimated jumping velocity is lower only by less than 5% compared to the experimental mean value. We seem to marginally underpredict the exact value of the experimental results, for which the reasons can be various. We argue that one of the reasons could be because we cannot be entirely certain regarding the fluid properties or the reported droplets radii in the experiments. It is to be noted here that the slip length used in the simulations was equal to the size of a wall cell, in the 40 cells per R_i grid, for the simulation case with initial droplets of size $R_i = 288$ m. This approach returns a physical value of $l_{sl} = 7.2$ m and the chosen setting gave the best agreement to the experiment for our jumping velocity, while such a high slip length is in line with the observed properties of superhydrophobic surfaces[19].

An extra emphasis is now given to demonstrate the adaptivity and high fidelity of our framework, by performing a three-droplet simulation of jumping of unequally-sized droplets. The aim here is to reproduce in detail all the stages of this

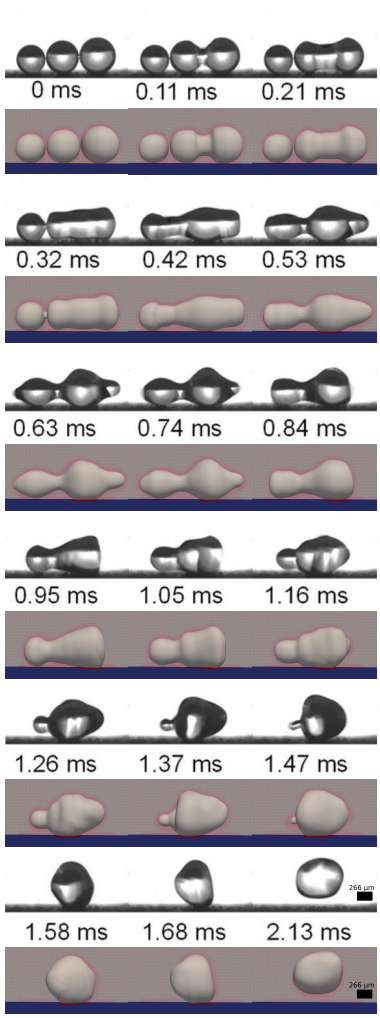

FIG. 5: Comparison of different stages of the coalescing and jumping of three unequal droplets, provided by our simulations and experiments by Yan et al (with permission).[39]. The images from experiments are always given above the corresponding simulation ones. The droplet sizes are indicated in the bottom of the figure.

process as shown in the experimentally obtained images presented by Yan et al.[39]. We have estimated the radii of the initial droplets as $R_1 = 235$ m, $R_2 = 268$ m and $R_3 = 293$ m by analyzing the published figure and the suggested scaling from the authors. Time-instants are presented with the simulation results matching the experimental images in Figure 5. An exceptionally close agreement is demonstrated between the complex droplets' oscillation features appearing in the experiment and the video produced by our simulation. In detail, the initial process of the two larger droplets coalescing and the smaller one remaining still is unambiguously recognized in both the simulation and the experiment. At the moment when the smaller droplet starts its own coalescence with the resulting droplet, the expansion of the liquid bridge seems to agree for the two cases, as does the general shape of the two pre-merged droplets. Next, the expansion in the lengthwise direction and the liquid bridge formation are captured properly. The two recognizable features(lump-shaped formations) from the pre-merged droplets and the smaller droplet exist in all the instants following up to the point when the smaller droplet merges to the already formed bigger formation. The nipple formation has been accurately modeled by the simulation and at the correct time scales. When the jumping occurred, only a single instant was provided in the experimental study, which our simulation managed to predict as well. Therefore, we argue that the overall behavior of the jumping process for the three unequal droplets has been captured with very good precision. Consequently, we recognize the ability of our framework to capture the behavior of strong inertial and capillary effects that exist in the jumping droplets phenomenon.

We finally provide a validation case that reflects the nuances that the presence of hysteresis brings to a jumping droplets process. We first note that a general lack of significant quantity of experimental data on such surfaces (and especially on the parametric details that such studies could uncover) renders comparisons between experiments and numerical simulations far from straightforward. In our work, we have chosen to rely on a qualitative comparison with an experimental video provided as Video S4 in the supplementary information of Yan et al.[85]. The reported surface had a hysteresis of $\Delta\theta = 17^\circ$, with $\theta_{adv} = 162^\circ$ and $\theta_{rec} = 145^\circ$, and the radius of droplets of $R_i = 156$ m. In Figure 6 a set of instances extracted from that video are compared to our simulation with the same contact-angle values. The contact-angle model used for the simulation in this case was the quasi-static model, which was found to have a similar pinning moment at the fifth instant (at $t = 9.9 \cdot 10^{-4}$ s) shown in the figure. We point to the nucleation of tiny droplets in the experiments, as the surface was reported to be cooled. The existence of these droplets does not affect the experimentally identified stages of the jumping droplets process. We recognized in our simulations the same patterns in the oscillations and formations of the merged droplet as those in the experiment. Hence, we consider our numerical framework validated also for dealing with superhydrophobic surfaces with various degrees of hysteresis present, in addition to being able to capture the shape oscillations caused by the dominance of capillary and inertial forces.

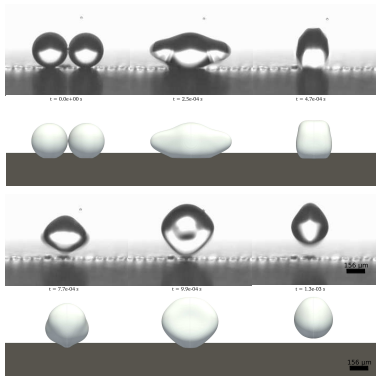

FIG. 6: Validation case of droplets jumping from a superhydrophobic surface with hysteresis present, as provided by a video recording from Yan et al. (with permission)[85]. The images from the experiments are given above the corresponding simulation ones, and instants from the simulation are provided that match the recording video timing suggested from the authors of the cited experimental study. Droplet sizes are indicated in the bottom of the figure.

IV. RESULTS AND DISCUSSION

To understand the influence of contact-angle hysteresis on the jumping process, we have carried out a series of simulations with various degrees of hysteresis and under different operating conditions. A qualitative point of comparison and a starting point in our analysis is to create numerical cases in accordance with existing experimental studies of droplets jumping from superhydrophobic surfaces with non-negligible degrees of hysteresis. Following the study of Mulroe et al.[32] that reported on the jumping ability of droplets with different radii from tuned superhydrophobic surfaces, we have selected a surface with a high degree of hysteresis as our base case. For the presented surface, designated as *S3* in Mulroe et al.[32], the values of $\theta_{adv} = 162^\circ$ and $\theta_{rec} = 147^\circ$ are provided. A minimum reported radius, termed a cut-off radius of droplets that indeed jumped on the *S3* surface, was approximately 25 m. We recreated such a case with equal droplets and first used the quasi-static contact-angle model to study the Moving Contact Line. A simulation with a static contact angle of $\theta = (\theta_{adv} + \theta_{rec})/2$ was also performed in order to understand how a simplified modeling approach for the contact angle would influence the jumping process. The two cases confirmed coalescing and jumping from the surface, but significant differences were observed. The results are presented by a plot of the normalized velocity evolution in Figure 7. Additionally, five instants of the two simulated cases are shown in the figure. We note that the stage of the liquid bridge expansion and the initial oscillations are captured similarly for the two cases. As depicted at instant *I*, the contact area with the solid surface is roughly the same, as well as the shape of the merged droplet. It can be also observed that during the liquid bridge expansion the initial contact area of the droplets reduces, causing a receding behavior at the contact line of the two initial droplets with the solid surface. While it later reaches roughly the same average upwards velocity, the simulation with hysteresis has a higher degree of initial attraction towards the surface, probably caused by the enforcement of the receding contact angle "sticking" the two initial droplets to the solid surface. This θ_{rec} is reduced by 7° compared to the value of the static contact angle imposed in the no-hysteresis case, where the contact angle is given by its equilibrium value. As expected from the literature, at instant *II* the droplet in a no-hysteresis case detaches from the surface. In contrast, the droplet with the hysteresis present retains contact with the surface due to the action of the receding contact angle (note the difference in the droplet–surface contact area at instant *II* for the two cases in Figure 7). Following a period where the velocity keeps decreasing for the hysteresis case, at instant *III* the merged droplet was also detached from the surface. It is noted that the shape of the droplet shows characteristic variations compared to the elevated no-hysteresis case. At instant *IV* the merged droplet for the simulation with hysteresis reattaches to the surface during a shape oscillation, in which the droplet elongates in the vertical direction and the interface hits the solid surface. Contact angles are re-applied and the velocity of the merged droplet decreases. The re-attachment is an important finding, contrasting the experience of jumping droplets on no-hysteresis surfaces, where the merged droplet just elevates into the air. At instant *V*, the merged droplet in the hysteresis case has a significantly different shape moments before detaching for the second time. Eventually, the droplet elevates with the reduced upwards velocity to that it possessed at the point of the final detachment. The droplet in the no-hysteresis case never experienced re-attachment and kept elevating with a constant velocity, while experiencing damping shape oscillations.

Next, we looked at the sensitivity of the simulations to slight variations of θ_{adv} and θ_{rec}. In addition to our base case, two more cases were tested with i) a halved hysteresis with $\Delta\theta = 7^\circ$ and ii) lowering θ_{adv} and θ_{rec} by 4°. In Figure 8A) the velocities of these three cases are presented. Figure 8B) shows the corresponding calculated contact angles imposed in the vicinity of the MCL, averaged for the different cells. The case i) with a reduced hysteresis showed an increased jumping velocity but the same general behavior of the coming detachment–re-attachment–detachment cycle as the base one. For case ii) with the reduced contact angles, the merged droplet was unable to jump. The experienced average velocity is below zero, as the droplet finally detaches during a retraction of the MCL caused by the shape oscillation. Since the droplet decelerated during the contact with the surface, it obtained a negative velocity, with the direction being towards the wall. The contact-angle values show that for the base case the process was initiated with the receding contact an-

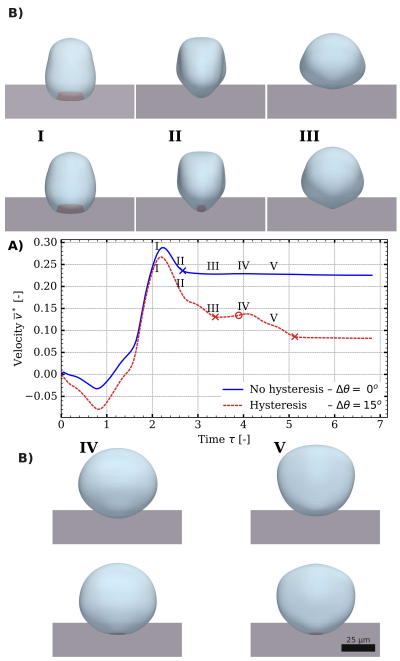

FIG. 7: The influence of hysteresis on fundamental features of droplets jumping from superhydrophobic surfaces. A) The normalized upwards velocities for the hysteresis- and no-hysteresis cases are plotted as a function of non-dimensional time, while the crosses (×) and circles (○) represent the moments where detachment and re-attachment occur correspondingly. B) Five instants from both simulations are presented. For each pair, the no-hysteresis case is depicted above the corresponding hysteresis one. A significant reduction in the jumping velocity and a temporary re-attachment for the droplets with the hysteresis present is observed. Note the difference in the droplet–surface contact area at instant *II* for the two cases. Droplet sizes are indicated in the bottom of the figure.

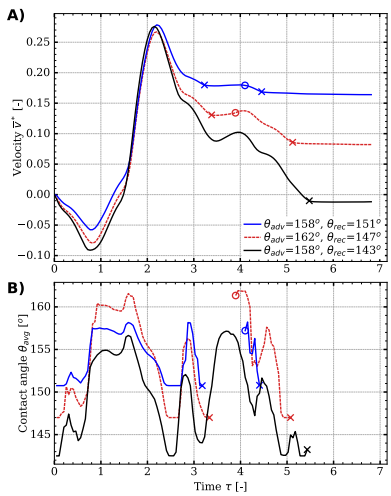

FIG. 8: A) Velocity evolution of three cases with a substantial hysteresis: the base case (the dashed red line) with $\Delta\theta = 15^\circ$, the test case i) (the blue line) with a reduced hysteresis ($\Delta\theta = 7^\circ$) and the test case ii) (the black line) with lower contact angles imposed while preserving $\Delta\theta = 15^\circ$. The initial droplet radius in all the cases is $R_i = 25$ m. The crosses (×) and circles (○) represent the moments where detachment and re-attachment occur. B) Variations of the contact angle with time for the three cases, averaged for the length of the contact line. The differences in contacts of the droplets with the superhydrophobic surface are observed, as well as the decrease in the jumping velocity as the degree of hysteresis increases and/or θ decreases.

gles in most locations of the interface. Following the moment when the liquid bridge hits the surface, the droplet expands on the solid surface and the advancing angles dominate. At that point, high acceleration is observed. Before detachment for the cases with the applied hysteresis, the imposed angles switched twice between the receding and advancing angles. The jumping occurred for the base case and the test case i). After this, the merged droplet was re-attached with a slight time difference between the two cases, at which point an advancing behavior was observed before ultimately switching to a mostly receding one and finally jumping. The test case ii) with the lower contact angles showcased similar variations for the contact angle, caused by the shape oscillations of the merged droplet, and eventually the droplet was detached at a later stage. Additional information is given in Figure 8B) on the enhanced attraction of the initial droplets mass toward the solid surface, during the liquid bridge expansion stage. The receding values are dominating the initial stage and the influence in the negative velocity is more prominent for higher hysteresis situations. Moreover, the maximum upwards velocity of the merged droplets is roughly the same, which proves that

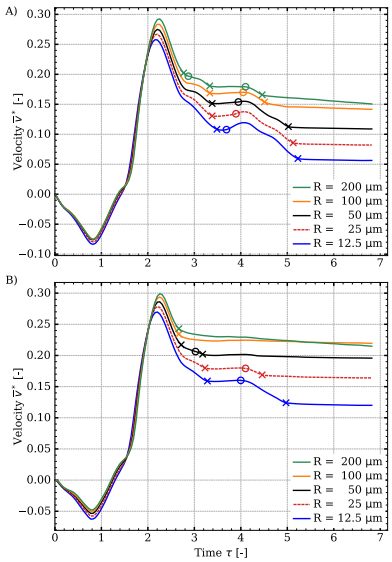

FIG. 9: Effect of radius of the initial droplets on the velocity for cases with different degrees of hysteresis (*A)* $\Delta\theta = 15^\circ$ with $\theta_{adv} = 162^\circ$ and $\theta_{rec} = 147^\circ$, and *B)* $\Delta\theta = 7.5^\circ$ with $\theta_{adv} = 158^\circ$ and $\theta_{rec} = 151^\circ$). The non-dimensional upwards velocity of the droplets is compared for five droplet radii. The moments of detachment and re-attachment are pointed with crosses (×) and circles (○) respectively for each simulation. We notify the trend for the decrease in the jumping velocity as the droplet radius reduces.

θ_{adv} is a less important factor to the eventual jumping velocity compared to the value for θ_{rec}.

We have seen so far that the presence of hysteresis significantly changes the nature of the jumping process from superhydrophobic surfaces. An interesting question is now the role of the size of initial droplets. In our previous work[81] it was shown that droplets as small as $R_i = 10$ m demonstrate the same non-dimensional velocity as do larger droplets, with only gravity becoming a factor of variation in the latter case. Therefore, we have performed a series of simulations with varying droplet radii in which contact angles were given according to the base case ($\Delta\theta = 15^\circ$). Figure 9A demonstrates the non-dimensional velocities for $R_i = 12.5 - 200$ m, which show for all the cases the previously identified re-attachment–detachment phenomenon that follows the initial detachment stage. The jumping velocity decreases for each size reduction. This finding emphasizes that, as the relevance of inertia decreases related to the viscous forces in the system, the droplet will stay attached longer to the surface. Consequently, a longer contact will result in more dissipation of energy due to interaction with the superhydrophobic surface, which in the numerical investigation is partly caused by the viscous stresses at the Moving Contact Line (MCL). To identify the sensitivity of that result to the contact-angle values, the hysteresis was reduced to a half of that of the base case ($\Delta\theta = 7^\circ$, the same as presented in Figure 8) for all the different sizes and the results are presented in Figure 9B. It is noted that for $R_i \geq 100$ m the droplet is detaching from the surface only once and retains the jumping velocity of the first detachment, in line with the known behavior of cases without hysteresis. For $R_i \leq 50$ m the double detachment is observed for both configurations, although a higher jumping velocity is noticed for the cases with a lower degree of hysteresis. The decreased velocity in the cases with higher hysteresis is explained by the greater adhesion force ($F_{pinning}$), as the merged droplet remains longer in contact with the surface.

After having observed the effects of hysteresis when $\Delta\theta$ increases, we looked at the influence of the initial radii (R_i) of the coalescing droplets on the jumping velocity. In detail, we have tested four $\Delta\theta$ (0°, 3°, 7° and 15°) with five cases of initial droplet radii ($R_i = 12.5, 25, 50, 100$ and 200 m). The jumping velocities are presented in Figure 10. We note that the jumping velocities decrease steadily for droplets smaller than $R_i \leq 50$ m. Such a trend is particularly visible for the cases with $\Delta\theta = 7$ and 15°, where the influence of a receding contact angle hinders the self-jumping of droplets of progressively smaller radii. On the other hand, the jumping velocity is much less sensitive to changes in droplet radii for no-hysteresis and small-hysteresis cases (0° and 3°). A slight drop, as observed at $R_i \leq 25$ m, follows the trends reported in the literature for numerical studies of jumping of micro-droplets on superhydrophobic surfaces[81]. There can be two additional conclusions from the same figure. The first one is that the highest degree of hysteresis showed a significant decrease in the jumping velocity for all the radii investigated. Second, there is a significant jump in the decrease of the jumping velocity of the case of $\Delta\theta = 7^\circ$ when R_i lowers from 50 to 12.5 m. Our understanding is that, considering also the results from Figure 9, the jumping droplet misses a chance of detaching while a retraction stage is recorded for $R_i \leq 25$ m, and therefore it decelerates and has a re-attachment at a later stage, which causes the significant loss of the upwards kinetic energy.

As the next step in our study, we looked at the significance of using dynamic contact angles in the simulations. We focused on being able to dynamically adjust the contact angle during its implementation in the cells near the solid surface and in proximity to the contact line location. For this study, θ_{dyn} is dependent on the computed contact line velocity and the model chosen for obtaining θ_{dyn} is the Kistler model[75], which utilizes the Hoffman correlation function for apparent contact angles in advancing liquids. The same model has also been used when a contact line is receding. A modification of the Hoffman function was implemented following a previous

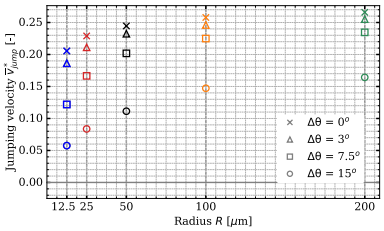

FIG. 10: Collected numerical results for v^*_{jump} over five different initial droplets radii, R_i. The increasing hysteresis leads to a significant reduction in the jumping velocity. This trend is especially pronounced for all the R_i in the highest hysteresis case and for $R_i \leq 50$ m for the medium hysteresis case (e.g. for $\Delta\theta = 7.5°$).

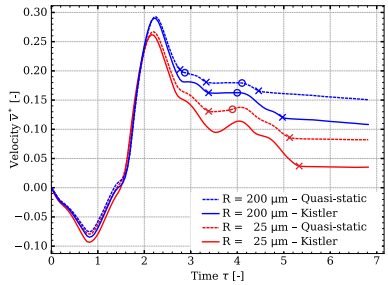

FIG. 11: The normalized velocity using two contact-angle models: the quasi-static model (the dashed lines) and the Kistler dynamic model (the solid lines) for two initial droplet radii R_i. The crosses (×) and circles (○) represent the moments where detachment and re-attachment occur. The normalized velocity plots illustrate how the use of different models affects the upwards velocity of the droplets. The use of the Kistler model results in the lower jumping velocity for both R_i.

study on both advancing and receding contact angles, which proved that for surfaces with very high contact angles[77] the Kistler model is still able to capture the behavior of the published experimental data[76]. We remind the reader that when using the Kistler model, the value of the contact angle for a static arrangement is required, which is the same as the quasi-static θ_{adv} and θ_{rec} values for the corresponding contact line movement. In our case, the values of $\theta_{adv} = 162°$ and $\theta_{rec} = 147°$ were used as input when implementing the dynamic contact-angle model. The simulations were performed for two initial droplet radii, $R_i = 25$ m and $R_i = 200$ m, and the normalized velocity profiles are shown in Figure 11. For comparison, we present the results obtained using the quasi-static contact-angle model in the same figure. The velocity decreased for both sizes when using a dynamic model, as the contact period of the merged droplet with the surface lasted longer. For the case of $R_i = 200$ m with the quasi-static contact-angle model, the merged droplet demonstrated an early detachment–re-attachment sequence, which was not seen in the dynamic contact-angle case, where the merged droplet remained in contact with the solid surface at that point. Afterwards, the larger droplet in the dynamic contact-angle model case displayed a delayed final detachment compared to the quasi-static contact-angle one, which resulted in a decrease of the jumping velocity of more than 25 %. A similar behavior of a longer contact and the later release was identified for the smaller droplet case, where the use of the dynamic contact-angle model showed a single occurrence of detachment and a highly reduced jumping velocity compared to the quasi-static contact-angle case (the difference being more than 40 %). We remind the reader here that using the quasi-static contact-angle model already represented a significant step in reducing the jumping efficiency when hysteresis was considered.

Following the results for droplets of $R_i = 25$ m, in Figure 12 the averaged contact-angle values along the MCL are given for the two different contact-angle models at each time step. We note how the dynamic contact angle decreases differently in the periods when a more pronounced receding movement of the contact line is observed. The receding contact angle of the dynamic model is lower than the one from the static θ_{rec} during the retraction stages of the merged droplet. This adjustment causes the merged droplet to avoid detachment at $\tau \sim 3.4$ in contrast to the quasi-static model case, while it also delays the final detachment of the droplet. This slight variation in the averaged receding contact angle of almost 2°, during the time where the contact line velocity is high, demonstrates variations in possible outcomes of the jumping process and its efficiency. These variations reveal the importance of applying the effective (i.e. truly acting) contact angle and deciding on the choice of parameters that affect the dynamic contact angle, which for our study was the contact line velocity. Note that, in general, there can be other possibilities for such parameters (that were not considered in this study), such as the existence of pillars or partial wetting instabilities (e.g. changes from Wenzel to Cassie–Baxter wetting types).

The choice of a dynamic contact-angle model leads to variations in the velocity evolution and the dependence on the effective receding contact angle in the system. For a more systematic study on how the mentioned phenomena vary for droplets of different sizes, the two contact-angle models were employed in the simulations involving five initial droplet radii ($R_i = 12.5, 25, 50, 100$ and 200 m). The results were compared to the equivalent simulations with the static contact angle at $\theta_{st} = 154°$, which is the mean of the θ_{adv} and θ_{rec} for the superhydrophobic surface investigated in this study. The

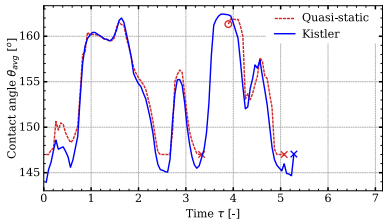

FIG. 12: Comparison of the averaged contact angle implemented along the contact line in the cases of the two contact-angle models for $R_i = 25$ m. The crosses (×) and circles (○) represent the moments where detachment and re-attachment occur. The use of the Kistler model led to a deviation of the receding contact-angle value that is imposed at the merged droplet. As a result, a longer period of contact to the solid surface was noted.

results are presented in Figure 13. The significant decrease in the jumping velocity, that was already recognized between the cases involving the static and quasi-static contact-angle representations in Figure 10, was further exaggerated by an extra negative offset, proportional to R_i, when the dynamic contact-angle model was used. More specifically, the jumping velocity obtained by the Kistler model for $R_i \leq 25$ m droplets is only $10-15$ % of the jumping velocity for an ideal superhydrophobic surface without hysteresis present. It can be concluded that the presence of a cut-off radius of around $R_i \sim 25$ m, as recorded by Mulroe et al.[32] for the actual surface, is more realistically captured by the simulations with the quasi-static and the Kistler contact-angle model, in contrast to the simulations using the static contact angle. We note here that the Kistler dynamic contact-angle model depends on a relatively limited

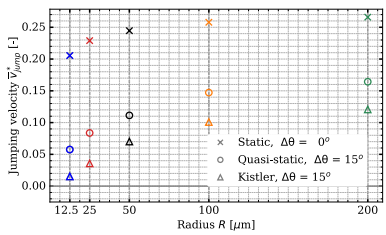

FIG. 13: The jumping velocity as a function of initial droplet radii (R_i) when three contact-angle models were tested. For a surface with a present contact-angle hysteresis, the static contact angle will overpredict the jumping velocity v^*_{jump}.

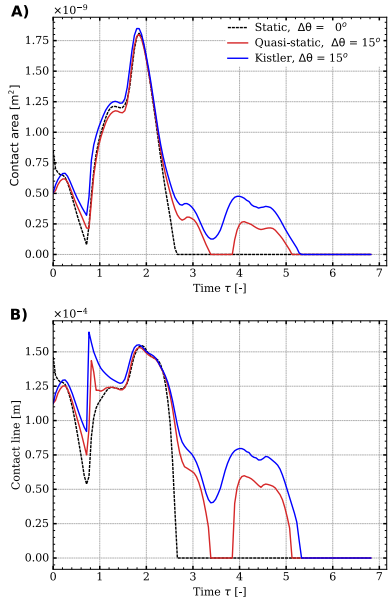

FIG. 14: A) Contact area evolution and B) the contact-line length evolution for the merged droplet on the superhydrophobic solid surface. Three different contact-angle implementations with the same equilibrium angle $\theta = 155°$ and the initial droplet radii $R_i = 25$ m. A higher value of the contact area before the late detachment can be observed when stronger hysteresis is imposed. The contact line follows the same trend, despite a "spike" when the liquid bridge hits the surface.

number of properties, such as the contact line velocity and the liquid properties. Other formulations are always possible, i.e. different models can be tested to find correlations that a certain dynamic model can have to a specific superhydrophobic surface.

We have seen that many of the fundamental attributes observed when droplets jump from superhydrophobic surfaces with hysteresis are directly linked to specific features of the interaction of the merged droplet with a solid surface in such cases. We thus present the contact area evolution A_{cont} obtained by different simulations in Figure 14A) to uncover even more subtle effects that are caused by enforcing the contact-angle hysteresis. The variations of contact areas with time are

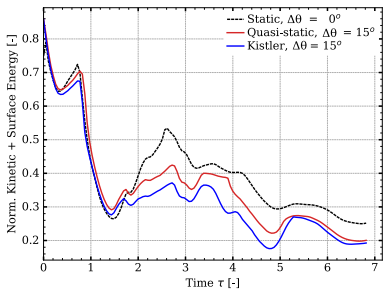

FIG. 15: The sum of the total kinetic energy and the available surface energy from the interface, normalized by the ideal available surface energy (see Results and Discussion section for more details). Three different cases of contact-angle representations are plotted vs. normalized time τ with $R_i = 25$ m. The difference in the final combined energy between the static contact-angle representation and the quasi-static and Kistler models reveals a higher dissipation for the latter cases.

presented in the figure of the cases with a static contact angle, the quasi-static and the Kistler dynamic contact-angle models. It is shown that, even though the initial evolutions of the contact areas during coalescence are not identical, the liquid bridge impingement and the maximum upwards acceleration bear qualitative similarities for the three cases. However, there are subtle differences that explain a different dynamics of the jumping process in the three cases. We see that a minimization of the contact area in the static contact-angle case occurs in a rapid manner, while for the quasi-static and Kistler models the contact area slows down in reducing and, around the normalized time of $\tau \simeq 3.5$, it starts increasing again. At that moment, the merged droplet starts expanding or re-attaches itself to the surface before a subsequent final retraction and jumping. The length of the contact line which is given in Figure 14B) follows the same trend. A rapid increase at the same instant was observed for the cases that impose hysteresis in the system, and is caused by the liquid bridge hitting the surface. The total contact line was already longer in the hysteresis cases when that event occurs, something that is attributed to the smaller receding contact angle of the initial spherical droplets when they were in contact with the solid surface.

An increase in the length of the contact line, that was previously observed for the case with the dynamic contact-angle model, can be directly connected to the presence of higher total stresses in the system. These stresses are exerted from the liquid in the vicinity of the contact line. They cause a higher dissipation of the energy in the system and are attributed to the viscous effect arising from the interaction of the moving interface with the solid surface. To observe the increase in the dissipated energy, we have decided to combine the total kinetic energy K_{tot} and the available surface energy ΔS_{avail}, which is the difference between the instant interface area A_{inter} and the final interface area of the merged droplet A_{end}, multiplied by the gas-liquid surface tension σ ($\Delta S_{avail} = (A_{inter} - A_{end}) \times \sigma$). We add the two energies and normalize them with the ideal surface energy ΔS_{ideal} of the system, which is the difference between the surface energy of the interface of two initial spherical droplets with R_i (in this case $R_i = 25$ m) and the resulted merged spherical droplet with a final radius R_{end}. From the equation for the total area of spheres, ΔS_{ideal} is given as $\Delta S_{ideal} = 4\pi(2 \times R_i^2 - R_{end}^2) \times \sigma$. The results from the combined kinetic and interface energy are given in Figure 15. We understand that the remaining component of the energy budget is completed by the unknown values of the dissipated energy due to viscosity E_{vis} and the surface energy of the contact area between the liquid droplet and the solid surface $S_{cont} = A\,\sigma_{ls}$, for which we know that it will be zero after jumping (σ_{ls} is the surface tension between liquid and the solid surface). The key point in the presented results is given in the final phase of the simulations, where the droplets belonging to all the cases have jumped from the surface. The combined kinetic and surface energy has been more reduced for the cases with hysteresis, with a more prominent reduction for the case with the Kistler model used. Moreover, when we include in the analysis the contact area of Figure 14A) for the period that the merged droplet in the hysteresis cases is in contact with the surface, between $\tau \simeq 2.7 - 3.4$ and $\tau \simeq 3.8 - 5.1$, we observe that such cases showcase reduced energy in Figure 15. A part of this energy is recovered during detachment of the merged droplet, but as the analysis of the final combined energy suggested, the energy is reduced more for the cases with hysteresis.

Finally, we demonstrate different wetting behaviors observed from the quasi-static and the dynamic contact-angle models, following the coalescence of two droplets ($R_i = 25$ m) at $\tau = 1.58$. In Figure 16 the contact line is presented in a top view and colored by the local contact angle imposed along the MCL for each model. The contact line velocity vectors are also depicted. The vector arrows are scaled and colored by their magnitude, and are tangential to the solid surface. At the investigated instant, the contact line of the two simulations shows an advancing movement in the y-direction and a receding movement in the x-direction. The contact area is significantly increased for the dynamic model (depicted right). However, only the length in the x-direction is increased in relation to the one when the quasi-static model is used (left), while the length in the y-direction of the contact area is the same. Taking into consideration that the receding angle is some 3° lower for the dynamic model, it permits us to point out the correlation of the lower receding angle to the larger wetting area. In addition, the contact-line velocity in the x-direction is higher for the simulation with the dynamic model, which is most likely caused by the higher curvature of the interface near the contact line junction. These outcomes exemplify the highlights of the current study, that the jumping process can be highly sensitive to the local contact angle on superhydrophobic surfaces with substantial hysteresis. There-

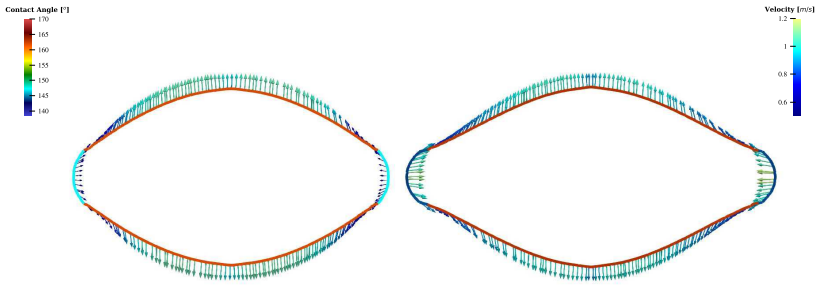

FIG. 16: Outline of the contact area of the merged droplet for the quasi-static contact-angle model (left) and the Kistler dynamic contact-angle model (right), colored by the imposed contact-angle value. We have added vector arrows of the contact line velocity scaled and colored by their magnitude. A significant increase in the contact area is observed, while correlation of the receding movement and the length in the movement's direction is acknowledged.

fore, modeling similar cases requires sufficient understanding of the contact-line interaction with the geometrical features of these surfaces.

V. CONCLUSIONS

We primarily focused in this paper on the influence of the contact-angle hysteresis on fundamental features of the jumping process of coalescing droplets on superhydrophobic surfaces, and therefore paid special attention to both representing and numerically implementing effective values of the contact angles acting on such surfaces. A combined VOF–immersed boundary method was used, with an emphasis on the accurate prediction of the Moving Contact Line (MCL) and on the formulation of the corresponding boundary conditions for the contact angles. A series of simulations were performed with static contact angles and dynamic contact-angle models for two equally-sized droplets and with several different initial droplet radii. The first outcome of this investigation is that hysteresis causes a delayed merged-droplet release and that it reduces the jumping velocity. Even more importantly, we have identified and explained in detail various forms of events involving droplet detachment and re-attachment to the surface. We have shown that such events depend on the degree of hysteresis for the modeled superhydrophobic surface, with the pinning behavior considerably enhanced when hysteresis was present.

We first demonstrated the temporal and spatial convergence of our numerical framework. The significance was pointed out of carefully selecting an appropriate slip length, as a measure to deal with the contact-line stress singularity. Furthermore, we have tested our framework on the experimentally well-documented case of coalescing and jumping of three unequally-sized droplets[39], and provided great qualitative agreement with experimentally obtained images of all relevant stages of the jumping process. We also showed that we could very well match quantitative results of the jumping velocities over a range of droplet radii. Finally, we have validated our framework with the reported experiments carried out on a superhydrophobic surface with the hysteresis present[85].

The presence of hysteresis further highlights the differences in the jumping process when different contact-angle representations and models are used. We first compared the case involving a static contact angle and the one with a quasi-static contact-angle model, with the latter using the values of the advancing and receding contact angles. We followed an experimental study[32], with a reported superhydrophobic surface that predicted the existence of a cut-off radius for the jumping to take place and that is about the size of the simulated droplets. The use of the quasi-static contact-angle model demonstrated a longer period of contact for the merged droplet and the surface, while the jumping velocity was less than a half compared to that when using the static contact-angle. Moreover, the initial detachment of the merged droplet and its subsequent re-attachment to the surface were repeatedly observed, while, eventually, an event of self-ejection occurred.

Two additional investigations with slight variations in the values of the advancing and receding contact angles, together with using a range of different initial droplet radii, portrayed the sensitivity of the simulations to the applied contact angles. Especially after varying the size of the initial droplets, we have observed sequences of detachment and re-attachment, while

the final jump took place with a delay in the cases with a higher degree of hysteresis. Similarly, for the smaller droplets the jumping velocity was observed to decrease, with the moment of jumping being increasingly delayed.

Finally, we used the Kistler dynamic contact-angle model to establish the relevance of using the actual (i.e. effective or truly acting) values of contact angles when studying the jumping process. We compared the obtained results with those when a static contact angle and the quasi-static contact-angle model are used. An investigation of the energy conversion process and the dissipated energy caused by hysteresis was also performed. The analysis supported the conclusion that a dynamic receding contact angle impeded the jumping process, as the jumping velocity became highly reduced or even neutralized for all the tested initial droplet radii. In addition, the duration of the merged droplet–surface contact and the experienced contact area were increased when the dynamic model was used.

ACKNOWLEDGMENTS

The authors would like to thank the Swedish Research Council for the financial support of this project (Vetenskapsrådet, Dnr 2019-04969).In addition, we would like to acknowledge that the handling of data and other computations were enabled by resources provided by the Swedish National Infrastructure for Computing (SNIC), which is partially funded by the Swedish Research Council through grant agreement no. 2018-05973.

[1] D. Quéré, "Non-sticking drops," Reports Prog. Phys. **68**, 2495–2532 (2005).
[2] N. Miljkovic, R. Enright, and E. N. Wang, "Modeling and Optimization of Superhydrophobic Condensation," J. Heat Transfer **135**, 111004–1 – 111004–14 (2013).
[3] N. Miljkovic, R. Enright, Y. Nam, K. Lopez, N. Dou, J. Sack, and E. N. Wang, "Jumping-droplet-enhanced condensation on scalable superhydrophobic nanostructured surfaces," Nano Lett. **13**, 179–187 (2013).
[4] H. Wang, L. Tang, X. Wu, W. Dai, and Y. Qiu, "Fabrication and antifrosting performance of super hydrophobic coating based on modified nano-sized calcium carbonate and ordinary polyacrylate," Appl. Surf. Sci. **253**, 8818–8824 (2007).
[5] S. A. Kulinich and M. Farzaneh, "How wetting hysteresis influences ice adhesion strength on superhydrophobic surfaces," Langmuir **25**, 8854–8856 (2009).
[6] S. Farhadi, M. Farzaneh, and S. A. Kulinich, "Anti-icing performance of superhydrophobic surfaces," Appl. Surf. Sci. **257**, 6264–6269 (2011).
[7] L. B. Boinovich and A. M. Emelyanenko, "Anti-icing potential of superhydrophobic coatings," Mendeleev Commun. **23**, 3–10 (2013).
[8] C. Antonini, A. Amirfazli, and M. Marengo, "Drop impact and wettability: From hydrophilic to superhydrophobic surfaces," Phys. Fluids **24** (2012), 10.1063/1.4757122.
[9] K. M. Wisdom, J. A. Watson, X. Qu, F. Liu, G. S. Watson, and C.-H. Chen, "Self-cleaning of superhydrophobic surfaces by self-propelled jumping condensate," Proc. Natl. Acad. Sci. **110**, 7992–7997 (2013).
[10] Q. Wang, X. Yao, H. Liu, D. Quéré, and L. Jiang, "Self-removal of condensed water on the legs of water striders," Proc. Natl. Acad. Sci. U. S. A. **112**, 9247–9252 (2015).
[11] D. Maggiolo, M. Seemann, H. Thunman, O. Santos, A. Larsson, S. Sasic, and H. Ström, "Self-Cleaning Surfaces for Heat Recovery During Industrial Hydrocarbon-Rich Gas Cooling: An Experimental and Numerical Study," AIChE J. **65**, 317–325 (2019).
[12] S. P. Dalawai, M. A. Saad Aly, S. S. Latthe, R. Xing, R. S. Sutar, S. Nagappan, C. S. Ha, K. Kumar Sadasivuni, and S. Liu, "Recent Advances in durability of superhydrophobic self-cleaning technology: A critical review," Prog. Org. Coatings **138**, 105381 (2020).
[13] C. Yu, S. Sasic, K. Liu, S. Salameh, R. H. Ras, and J. R. van Ommen, "Nature–Inspired self–cleaning surfaces: Mechanisms, modelling, and manufacturing," Chem. Eng. Res. Des. **155**, 48–65 (2020).
[14] W. Chen, A. Y. Fadeev, M. C. Hsieh, D. Öner, J. Youngblood, and T. J. McCarthy, "Ultrahydrophobic and ultralyophobic surfaces: some comments and examples," Langmuir **15**, 3395–3399 (1999).
[15] B. Bhushan and Y. C. Jung, "Wetting, adhesion and friction of superhydrophobic and hydrophilic leaves and fabricated micro/nanopatterned surfaces," J. Phys. Condens. Matter **20**, 225010 (2008).
[16] D. Öner and T. J. McCarthy, "Ultrahydrophobic surfaces. Effects of topography length scales on wettability," Langmuir **16**, 7777–7782 (2000).
[17] J. Wu, J. Xia, W. Lei, and B. P. Wang, "Advanced understanding of stickiness on superhydrophobic surfaces," Sci. Rep. **3**, 2–5 (2013).
[18] Y. Liu and C. H. Choi, "Condensation-induced wetting state and contact angle hysteresis on superhydrophobic lotus leaves," Colloid Polym. Sci. **291**, 437–445 (2013).
[19] D. Quéré, "Wetting and roughness," Annu. Rev. Mater. Res. **38**, 71–99 (2008).
[20] P.-G. de Gennes, F. Brochard-Wyart, and D. Quéré, *Capillarity Wetting Phenom.* (2004).
[21] J. H. Snoeijer and B. Andreotti, "Moving Contact Lines: Scales, Regimes, and Dynamical Transitions," Annu. Rev. Fluid Mech. **45**, 269–292 (2013).
[22] R. Weiqing and E. Weinan, "Boundary conditions for the moving contact line problem," Phys. Fluids **19** (2007), 10.1063/1.2646754.
[23] J. B. Boreyko and C. H. Chen, "Self-propelled dropwise condensate on superhydrophobic surfaces," Phys. Rev. Lett. **103**, 2–5 (2009).
[24] R. Enright, N. Miljkovic, J. L. Alvarado, K. Kim, and J. W. Rose, "Dropwise condensation on micro-and nanostructured surfaces," Nanoscale Microscale Thermophys. Eng. **18**, 223–250 (2014).
[25] N. Miljkovic, R. Enright, and E. N. Wang, "Effect of droplet morphology on growth dynamics and heat transfer during condensation on superhydrophobic nanostructured surfaces," ACS Nano **6**, 1776–1785 (2012).
[26] K. Wang, Q. Liang, R. Jiang, Y. Zheng, Z. Lan, and X. Ma, "Morphology evolution and dynamics of droplet coalescence on superhydrophobic surfaces," AIChE J. **64**, 2913–2921 (2018).
[27] F. Liu, G. Ghigliotti, J. J. Feng, and C.-H. Chen, "Numerical simulations of self-propelled jumping upon drop coalescence on non-wetting surfaces," J. Fluid Mech. **752**, 39–65 (2014).
[28] F. Liu, G. Ghigliotti, J. J. Feng, and C. H. Chen, "Self-propelled jumping upon drop coalescence on leidenfrost surfaces," J. Fluid Mech. **752**, 22–38 (2014).
[29] F. Liu, G. Ghigliotti, J. J. Feng, and C. H. Chen, "Numerical simulations of self-propelled jumping upon drop coalescence on non-wetting surfaces," J. Fluid Mech. **752**, 39–65 (2014).
[30] K. Yanagisawa, M. Sakai, T. Isobe, S. Matsushita, and A. Nakajima, "Investigation of droplet jumping on superhydrophobic coatings during dew condensation by the observation from two directions," Appl. Surf. Sci. **315**, 212–221 (2014).
[31] C. Lv, P. Hao, X. Zhang, and F. He, "Dewetting Transitions of Dropwise Condensation on Nanotexture-Enhanced Superhydrophobic Surfaces," ACS Nano **9**, 12311–12319 (2015).
[32] M. D. Mulroe, B. R. Srijanto, S. F. Ahmadi, C. P. Collier, and J. B. Boreyko, "Tuning Superhydrophobic Nanostructures To Enhance Jumping-Droplet Condensation," ACS Nano **11**, 8499–8510 (2017).
[33] K. Wang, Q. Liang, R. Jiang, Y. Zheng, Z. Lan, and X. Ma, "Self-enhancement of droplet jumping velocity: The interaction of liquid bridge and surface texture," RSC Adv. **6**, 99314–99321 (2016).
[34] H. Vahabi, W. Wang, J. M. Mabry, and A. K. Kota, "Coalescence-induced jumping of droplets on superomniphobic surfaces with macrotexture," Sci. Adv. **4**, eaau3488 (2018).
[35] D. Lu, M. Zhao, H. Zhang, Y. Yang, and Y. Zheng, "Self-Enhancement of Coalescence-Induced Droplet Jumping on Superhydrophobic Surfaces with an Asymmetric V-Groove," Langmuir **36**, 5444–5453 (2020).
[36] Q. Peng, X. Yan, J. Li, L. Li, H. Cha, Y. Ding, C. Dang, L. Jia, and N. Miljkovic, "Breaking Droplet Jumping Energy Conversion Limits with Superhydrophobic Microgrooves," Langmuir **36**, 9510–9522 (2020).

[37]M. K. Kim, H. Cha, P. Birbarah, S. Chavan, C. Zhong, Y. Xu, and N. Miljkovic, "Enhanced Jumping-Droplet Departure," Langmuir **31**, 13452–13466 (2015).
[38]Z. Khatir, K. J. Kubiak, P. K. Jimack, and T. G. Mathia, "Dropwise condensation heat transfer process optimisation on superhydrophobic surfaces using a multi-disciplinary approach," Appl. Therm. Eng. **106**, 1337–1344 (2016).
[39]X. Yan, L. Zhang, S. Sett, L. Feng, C. Zhao, Z. Huang, H. Vahabi, A. K. Kota, F. Chen, and N. Miljkovic, "Droplet Jumping: Effects of Droplet Size, Surface Structure, Pinning, and Liquid Properties," ACS Nano **13**, 1309–1323 (2019).
[40]S. Farokhirad, J. F. Morris, and T. Lee, "Coalescence-induced jumping of droplet: Inertia and viscosity effects," Phys. Fluids **27**, 102102 (2015).
[41]X. Liu and P. Cheng, "3D multiphase lattice Boltzmann simulations for morphological effects on self-propelled jumping of droplets on textured superhydrophobic surfaces," Int. Commun. Heat Mass Transf. **64**, 7–13 (2015).
[42]K. Wang, Q. Liang, R. Jiang, Y. Zheng, Z. Lan, and X. Ma, "Numerical Simulation of Coalescence-Induced Jumping of Multidroplets on Superhydrophobic Surfaces: Initial Droplet Arrangement Effect," Langmuir **33**, 6258–6268 (2017).
[43]R. Attarzadeh and A. Dolatabadi, "Coalescence-induced jumping of microdroplets on heterogeneous superhydrophobic surfaces," Phys. Fluids **29**, 012104 (2017).
[44]J. Wasserfall, P. Figueiredo, R. Kneer, W. Rohlfs, and P. Pischke, "Coalescence-induced droplet jumping on superhydrophobic surfaces: Effects of droplet mismatch," Phys. Rev. Fluids **2**, 1–17 (2017).
[45]G. Tryggvason, "Numerical simulation of self-propelled non-equal sized droplets," Phys. Fluids **31**, 052107 (2019).
[46]S. Li, F. Chu, J. Zhang, D. Brutin, and D. Wen, "Droplet jumping induced by coalescence of a moving droplet and a static one: Effect of initial velocity," Chem. Eng. Sci. **211**, 115252 (2020).
[47]T. Mouterde, T.-V. Nguyen, H. Takahashi, C. Clanet, I. Shimoyama, and D. Quéré, "How merging droplets jump off a superhydrophobic surface: Measurements and model," Phys. Rev. Fluids **2**, 112001 (2017).
[48]F. Chu, Z. Yuan, X. Zhang, and X. Wu, "Energy analysis of droplet jumping induced by multi-droplet coalescence: The influences of droplet number and droplet location," Int. J. Heat Mass Transf. **121**, 315–320 (2018).
[49]Z. Yuan, R. Wu, and X. Wu, "Numerical simulations of multi-hop jumping on superhydrophobic surfaces," Int. J. Heat Mass Transf. **135**, 345–353 (2019).
[50]Y. Wang and P. Ming, "Dynamic and energy analysis of coalescence-induced self-propelled jumping of binary unequal-sized droplets," Phys. Fluids **31**, 122108 (2019).
[51]S. Moghtadernejad, M. Tembely, M. Jadidi, N. Esmail, and A. Dolatabadi, "Shear driven droplet shedding and coalescence on a superhydrophobic surface," Phys. Fluids **27** (2015), 10.1063/1.4914168.
[52]H. Hou, Z. Yuan, Z. Hu, S. Gao, and X. Wu, "Effects of the surface tension gradient and viscosity on coalescence-induced droplet jumping on superamphiphobic surfaces," Phys. Fluids **33**, 112101 (2021).
[53]Y. Nam, H. Kim, and S. Shin, "Energy and hydrodynamic analyses of coalescence-induced jumping droplets," Appl. Phys. Lett. **103**, 161601 (2013).
[54]Y. Cheng, J. Xu, and Y. Sui, "Numerical investigation of coalescence-induced droplet jumping on superhydrophobic surfaces for efficient dropwise condensation heat transfer," Int. J. Heat Mass Transf. **95**, 506–516 (2016).
[55]Y. Chen and Y. Lian, "Numerical investigation of coalescence-induced self-propelled behavior of droplets on non-wetting surfaces," Phys. Fluids **30**, 112102 (2018).
[56]Y. Shi, G. H. Tang, and H. H. Xia, "Investigation of coalescence-induced droplet jumping on superhydrophobic surfaces and liquid condensate adhesion on slit and plain fins," Int. J. Heat Mass Transf. **88**, 445–455 (2015).
[57]H. Li, W. Yang, A. Aili, and T. Zhang, "Insights into the Impact of Surface Hydrophobicity on Droplet Coalescence and Jumping Dynamics," Langmuir **33**, 8574–8581 (2017).
[58]K. Wang, Q. Liang, R. Jiang, Y. Zheng, Z. Lan, and X. Ma, "Numerical Simulation of Coalescence-Induced Jumping of Multidroplets on Superhydrophobic Surfaces: Initial Droplet Arrangement Effect," Langmuir **33**, 6258–6268 (2017).
[59]Z. Liang and P. Keblinski, "Coalescence-induced jumping of nanoscale droplets on super-hydrophobic surfaces," Appl. Phys. Lett. **107**, 143105 (2015).
[60]S. Gao, Q. Liao, W. Liu, and Z. Liu, "Self-Removal of Multiple and Multi-size Coalescing Nanodroplets on Nanostructured Surfaces," J. Phys. Chem. C **122**, 20521–20526 (2018).
[61]F. F. Xie, G. Lu, X. D. Wang, and D. Q. Wang, "Enhancement of Coalescence-Induced Nanodroplet Jumping on Superhydrophobic Surfaces," Langmuir **34**, 11195–11203 (2018).
[62]Y. Nam, D. Seo, C. Lee, and S. Shin, "Droplet coalescence on water repellant surfaces," Soft Matter **11**, 154–160 (2015).
[63]H. Cha, C. Xu, J. Sotelo, J. M. Chun, Y. Yokoyama, R. Enright, and N. Miljkovic, "Coalescence-induced nanodroplet jumping," Phys. Rev. Fluids **1**, 064102 (2016).
[64]T. Mouterde, G. Lehoucq, S. Xavier, A. Checco, C. T. Black, A. Rahman, T. Midavaine, C. Clanet, and D. Quéré, "Antifogging abilities of model nanotextures," Nat. Mater. **16**, 658–663 (2017).
[65]E. B. Dussan, "On the Spreading of Liquids on Solid Surfaces: Static and Dynamic Contact Lines," Annu. Rev. Fluid Mech. **11**, 371–400 (1979).
[66]P. G. De Gennes, "Wetting: statics and dynamics," Rev. Mod. Phys. **57**, 827–863 (1985).
[67]D. Legendre and M. Maglio, "Computers & Fluids Comparison between numerical models for the simulation of moving contact lines," Comput. Fluids **113**, 2–13 (2015).
[68]J. EGGERS and H. A. STONE, "Characteristic lengths at moving contact lines for a perfectly wetting fluid: the influence of speed on the dynamic contact angle," J. Fluid Mech. **505**, 309–321 (2004), arXiv:0210101 [physics].
[69]S. Afkhami, J. Buongiorno, A. Guion, S. Popinet, Y. Saade, R. Scardovelli, and S. Zaleski, "Transition in a numerical model of contact line dynamics and forced dewetting," J. Comput. Phys. **374**, 1061–1093 (2018), arXiv:1703.07038.
[70]J. Göhl, A. Mark, S. Sasic, and F. Edelvik, "An immersed boundary based dynamic contact angle framework for handling complex surfaces of mixed wettabilities," Int. J. Multiph. Flow **109**, 164–177 (2018).
[71]A. Mark, R. Rundqvist, and F. Edelvik, "Comparison between different immersed boundary conditions for simulation of complex fluid flows," Fluid Dyn. Mater. Process. **7**, 241–258 (2011).
[72]J. P. Van Doormaal and G. D. Raithby, "Enhancements of the simple method for predicting incompressible fluid flows," Numer. Heat Transf. **7**, 147–163 (1984).
[73]O. Ubbink and R. I. Issa, "A Method for Capturing Sharp Fluid Interfaces on Arbitrary Meshes," J. Comput. Phys. **153**, 26–50 (1999).
[74]J. U. Brackbill, D. B. Kothe, and C. Zemach, "A continuum method for modeling surface tension," J. Comput. Phys. **100**, 335–354 (1992).
[75]S. F. Kistler, "Hydrodynamics of wetting," Wettability **6**, 311–430 (1993).
[76]R. L. Hoffman, "A study of the advancing interface. II. Theoretical prediction of the dynamic contact angle in liquid-gas systems," J. Colloid Interface Sci. **94**, 470–486 (1983).
[77]M. Jiang and B. Zhou, "Improvement and further investigation on Hoffman-function-based dynamic contact angle model," Int. J. Hydrogen Energy **44**, 16898–16908 (2019).
[78]M. M. Francois, S. J. Cummins, E. D. Dendy, D. B. Kothe, J. M. Sicilian, and M. W. Williams, "A balanced-force algorithm for continuous and sharp interfacial surface tension models within a volume tracking framework," J. Comput. Phys. **213**, 141–173 (2006).
[79]P. Bartholomew, F. Denner, M. H. Abdol-Azis, A. Marquis, and B. G. van Wachem, "Unified formulation of the momentum-weighted interpolation for collocated variable arrangements," J. Comput. Phys. **375**, 177–208 (2018).
[80]A. Mark and B. G. van Wachem, "Derivation and validation of a novel implicit second-order accurate immersed boundary method," J. Comput. Phys. **227**, 6660–6680 (2008).
[81]K. Konstantinidis, J. Göhl, A. Mark, and S. Sasic, "Coalescence-induced jumping of microdroplets on superhydrophobic surfaces – A numerical study," Can. J. Chem. Eng. , Accepted Author Manuscript, doi: 10.1002/cjce.2459 (2022).
[82]F. Denner and B. G. van Wachem, "Numerical time-step restrictions as a result of capillary waves," J. Comput. Phys. **285**, 24–40 (2015).
[83]M. Renardy, Y. Renardy, and J. Li, "Numerical Simulation of Moving Con-

tact Line Problems Using a Volume-of-Fluid Method," J. Comput. Phys. **171**, 243–263 (2001).
[84]S. Afkhami, S. Zaleski, and M. Bussmann, "A mesh-dependent model for applying dynamic contact angles to VOF simulations," J. Comput. Phys. **228**, 5370–5389 (2009).
[85]X. Yan, Z. Huang, S. Sett, J. Oh, H. Cha, L. Li, L. Feng, Y. Wu, C. Zhao, D. Orejon, F. Chen, and N. Miljkovic, "Atmosphere-mediated superhydrophobicity of rationally designed micro/nanostructured surfaces," ACS Nano **13**, 4160–4173 (2019).